



AFRL-AFOSR-VA-TR-2021-0095

Optical Ceramics Science for High-Power Lasers

**Gaume, Romain
UNIVERSITY OF CENTRAL FLORIDA
4000 CNTRL FLORIDA BLVD
ORLANDO, FL,
US**

**08/07/2021
Final Technical Report**

DISTRIBUTION A: Distribution approved for public release.

Air Force Research Laboratory
Air Force Office of Scientific Research
Arlington, Virginia 22203
Air Force Materiel Command

REPORT DOCUMENTATION PAGE

Form Approved
OMB No. 0704-0188

The public reporting burden for this collection of information is estimated to average 1 hour per response, including the time for reviewing instructions, searching existing data sources, gathering and maintaining the data needed, and completing and reviewing the collection of information. Send comments regarding this burden estimate or any other aspect of this collection of information, including suggestions for reducing the burden, to Department of Defense, Washington Headquarters Services, Directorate for Information Operations and Reports (0704-0188), 1215 Jefferson Davis Highway, Suite 1204, Arlington, VA 22202-4302. Respondents should be aware that notwithstanding any other provision of law, no person shall be subject to any penalty for failing to comply with a collection of information if it does not display a currently valid OMB control number.
PLEASE DO NOT RETURN YOUR FORM TO THE ABOVE ADDRESS.

1. REPORT DATE (DD-MM-YYYY) 07-08-2021	2. REPORT TYPE Final	3. DATES COVERED (From - To) 22 Dec 2017 - 31 Mar 2021
--	--------------------------------	--

4. TITLE AND SUBTITLE Optical Ceramics Science for High-Power Lasers	5a. CONTRACT NUMBER
	5b. GRANT NUMBER FA9550-18-1-0103
	5c. PROGRAM ELEMENT NUMBER 61102F

6. AUTHOR(S) Romain Gaume	5d. PROJECT NUMBER
	5e. TASK NUMBER
	5f. WORK UNIT NUMBER

7. PERFORMING ORGANIZATION NAME(S) AND ADDRESS(ES) UNIVERSITY OF CENTRAL FLORIDA 4000 CNTRL FLORIDA BLVD ORLANDO, FL US	8. PERFORMING ORGANIZATION REPORT NUMBER
--	---

9. SPONSORING/MONITORING AGENCY NAME(S) AND ADDRESS(ES) AF Office of Scientific Research 875 N. Randolph St. Room 3112 Arlington, VA 22203	10. SPONSOR/MONITOR'S ACRONYM(S) AFRL/AFOSR RTB1
	11. SPONSOR/MONITOR'S REPORT NUMBER(S) AFRL-AFOSR-VA-TR-2021-0095

12. DISTRIBUTION/AVAILABILITY STATEMENT
A Distribution Unlimited: PB Public Release

13. SUPPLEMENTARY NOTES

14. ABSTRACT
This final report summarizes the findings and results of our research effort on Optical Ceramics Science for High-Power Lasers. We report on our transparent YAG ceramic fabrication protocols, the calibration of equipment and the pursuit of stoichiometry assessment and quantification of SiO2 sintering aid by laser-induced breakdown spectroscopy (LIBS). We have developed a simulation tool to help us improve the accuracy of the fabrication process of transparent optical ceramics of YAG, as well as a model for simulating LIBS experiments on YAG. These new capabilities have brought dramatic improvement to our sample quality and fabrication consistency and to our understanding of the controlling parameters behind the fabrication process. These improvements are best epitomized by our recent laser tests on Tm:YAG ceramics and the production of Yb:YAG ceramics.

15. SUBJECT TERMS

16. SECURITY CLASSIFICATION OF:			17. LIMITATION OF ABSTRACT	18. NUMBER OF PAGES	19a. NAME OF RESPONSIBLE PERSON ALI SAYIR
a. REPORT	b. ABSTRACT	c. THIS PAGE			19b. TELEPHONE NUMBER (Include area code)
U	U	U	UU	102	426-7236

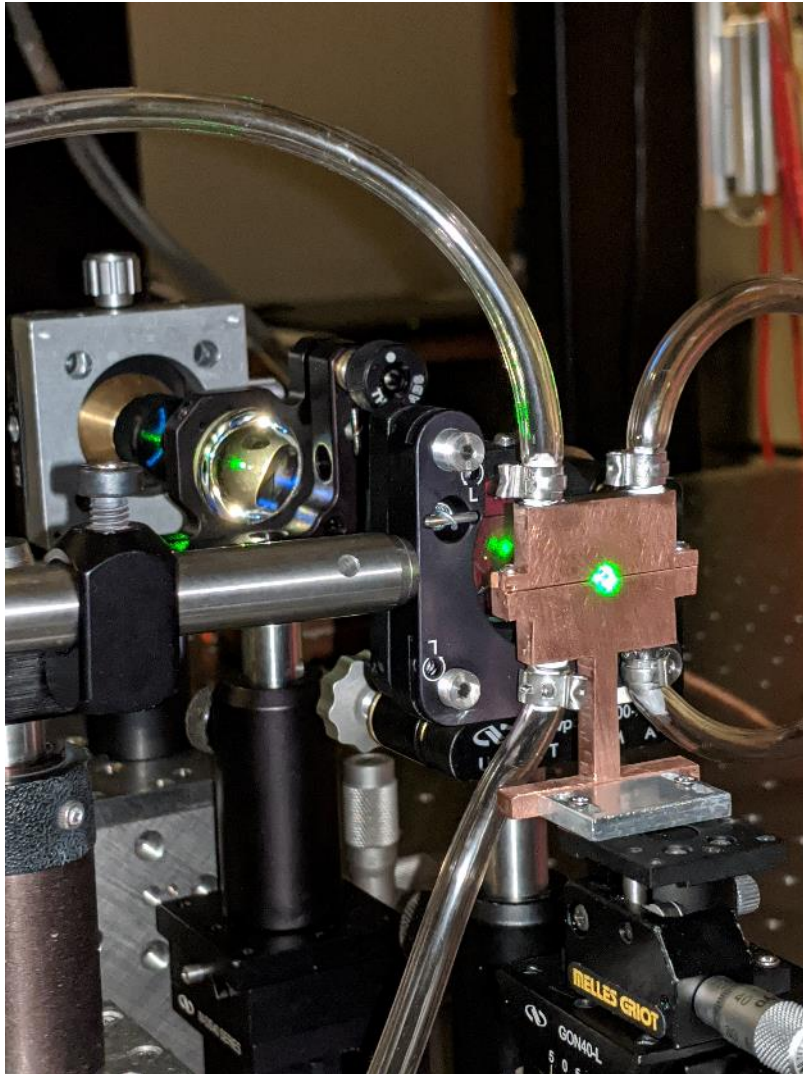
Standard Form 298 (Rev.8/98)
Prescribed by ANSI Std. Z39.18

REPORT DOCUMENTATION PAGE

1. Report Date 29 June 2021		2. Report type and Dates covered Final technical report, Dec 2017- March 2021	
3. Title Optical Ceramics Science for High- Power Lasers.		4. Funding number FA9550-18-1-0103	
5. Authors R. Gaume (PI), M. Julian, C. French, S. Stahl			
6. Performing Organization Name and Address College of Optics & Photonics, University of Central Florida (UCF) 4304 Scorpius street, Orlando, FL 32816-2700			
7. Sponsor and Program Manager AFOSR; Dr. Ali Sayir			
8. Distribution/Availability Statement Non-Restricted			
9. Abstract This final report summarizes the findings and results of our research effort on <i>Optical Ceramics Science for High-Power Lasers</i> . We report on our transparent YAG ceramic fabrication protocols, the calibration of equipment and the pursuit of stoichiometry assessment and quantification of SiO ₂ sintering aid by laser-induced breakdown spectroscopy (LIBS). We have developed a simulation tool to help us improve the accuracy of the fabrication process of transparent optical ceramics of YAG, as well as a model for simulating LIBS experiments on YAG. These new capabilities have brought dramatic improvement to our sample quality and fabrication consistency and to our understanding of the controlling parameters behind the fabrication process. These improvements are best epitomized by our recent laser tests on Tm:YAG ceramics and the production of Yb:YAG ceramics.			
10. Subject Terms Transparent ceramics; YAG; Y ₃ Al ₅ O ₁₂ ; Laser-induced breakdown spectroscopy; Non-stoichiometry; SiO ₂ sintering additive; LIBS plasma modeling;			
11. Security Classification Unclassified	12. Security Classification on this Page Unclassified	13. Security Classification of Abstract Unclassified	14. Number of Pages 103

Table of Contents

1. EXECUTIVE SUMMARY	4
2. INTRODUCTION	4
3. YAG CERAMIC FABRICATION.....	5
3.1 BACKGROUND.....	5
3.2 ACCOMPLISHMENTS	7
3.2.1 <i>Roots of non-stoichiometry in the ceramic fabrication process.....</i>	7
3.2.2 <i>Model Development: Propagation of uncertainty throughout fabrication process.....</i>	8
3.2.3 <i>Contamination free powder mixing process</i>	33
3.2.4 <i>Particle size and morphology characterization of as-received precursor and processed powders.....</i>	39
3.2.5 <i>Optical and preliminary laser characterization of sintered samples.....</i>	46
3.2.6 <i>Other accomplishments.....</i>	51
3.3 CONCLUSION	53
4. LASER-INDUCED BREAKDOWN SPECTROSCOPY (LIBS): A NOVEL METHOD FOR THE ASSESSMENT OF STOICHIOMETRY IN OPTICAL CERAMICS.	54
4.1 OBJECTIVES	54
4.2 ACCOMPLISHMENTS	58
4.2.1 <i>Simulation of YAG plasmas formed in air</i>	58
4.2.2 <i>Determination of the Al/Y molar ratio in unfired powder compacts of Al₂O₃-Y₂O₃.....</i>	67
4.2.3 <i>LIBS analysis of YAG phase powder compacts of unknown composition by aqueous solution standard addition method</i>	72
4.2.4 <i>LIBS study of sintered ceramics, powder compacts, and fused glass beads with aqueous solution based standard addition.....</i>	78
4.2.5 <i>Fabrication of sintered YAG ceramics with the composition varied by standard addition with sulfates and nitrates</i>	82
4.2.6 <i>Other accomplishments.....</i>	84
4.3 CONCLUSIONS.....	84
5. MONITORING OF SINTERING ADDITIVE CONCENTRATION AND UNINTENTIONAL IMPURITIES BY LIBS DURING THE FABRICATION OF TRANSPARENT CERAMICS OF YAG.....	85
5.1 OBJECTIVES	85
5.2 ACCOMPLISHMENTS	85
5.2.1 <i>Experimental.....</i>	86
5.2.2 <i>Results and discussion</i>	87
5.3 CONCLUSION	92
6. PROJECT CONCLUSIONS.....	93
6.1 YAG CERAMIC FABRICATION.....	93
6.2 LASER-INDUCED BREAKDOWN SPECTROSCOPY (LIBS): A NOVEL METHOD FOR THE ASSESSMENT OF STOICHIOMETRY IN OPTICAL CERAMICS	94
6.3 MONITORING OF SINTERING ADDITIVE CONCENTRATION AND UNINTENTIONAL IMPURITIES BY LIBS DURING THE FABRICATION OF TRANSPARENT CERAMICS OF YAG	95
6.4 SUMMARY	96
7. COMMUNICATIONS	97
8. REFERENCES.....	98



Tm:YAG transparent ceramic sample synthesized at UCF and under laser testing.

(see details in *Section 3.2.6*)

1. Executive Summary

This final report summarizes the findings and results of our research effort on *Optical Ceramics Science for High-Power Lasers*. We report on our transparent YAG ceramic fabrication protocols, the calibration of equipment and the pursuit of our stoichiometry assessment and quantification of SiO₂ sintering aid by laser-induced breakdown spectroscopy (LIBS). We have developed a simulation tool to help us improve the accuracy of the fabrication process of transparent optical ceramics of YAG, as well as a model for simulating LIBS experiments on YAG. These new capabilities have brought dramatic improvement to our sample quality and fabrication consistency and to our understanding of the controlling parameters behind the fabrication process. These improvements are best epitomized by our recent laser tests on Tm:YAG and the production of Yb:YAG ceramics. Our results have been published in three peer-reviewed journals and presented at three international conferences. Two patent applications are pending with the USPTO. This program has supported one Ph.D. student and has received the contribution of one Master's student and one undergraduate student.

2. Introduction

The demand for low optical-loss transparent ceramics for high-power laser components requires the ability to control the phase composition of multinary materials along with the microstructure. In this respect, the problem of stoichiometry, or more accurately the problem of deviation from stoichiometry, is one of the most critical issues pertaining to the fabrication of high-grade transparent ceramics of Y₃Al₅O₁₂ (YAG). Within the phase stability domain of a given multinary compound, departure from the nominal composition leads to the formation of point-defects until the solid-solubility limit is exceeded and secondary phases start segregating. Point-defects and precipitates not only control the sintering kinetics and final densification state of the ceramics but also affect their optical properties by introducing color centers, charge-carrier trapping sites and scattering centers. The 'inexplicable' non-reproducibility of high-quality transparent ceramic fabrication, that one comes to experience with certain materials, is closely related to investigating the nature and effect of these intrinsic defects on the sintering behavior and optical properties and measuring small excess of major elements with accuracies better than 0.1 mol%. While modern analytical techniques are commonly used to determine impurity concentrations down to ppm or ppb levels, there is, at present, no simple and direct method in scientific practice for determining deviation from stoichiometry in insulator materials except for precision measurement of crystal lattice parameters by x-ray diffraction. On top of this issue, we have published two studies in which we show that intentional impurities (such as silicon sintering additive in YAG), as well as unintentional impurities (such as iron, introduced in most ceramic processing routes) can produce broadband absorption in the NIR and visible.

Hence, our objective was to develop robust fabrication protocols as well as adequate and highly accurate analytical methods for the assessment of ceramic powder composition in order

to guarantee the consistency of the fabrication process of YAG transparent ceramics. The clear intent of this approach is to lay the fabrication of high optical quality ceramics on a firmer scientific ground than current trial-and-error practices.

The following sections summarize our findings regarding: (i) the fabrication of composition-controlled YAG ceramics, (ii) the development of a novel analytical technique that can provide sensitive and precise real-time assessment of the stoichiometry, and (iii) the use of this technique to monitor sintering additives (SiO_2) during the fabrication process.

3. YAG ceramic fabrication

3.1 Background

Despite the remarkable laser power-scaling results obtained with high-quality YAG ceramic slabs from *Konoshima Chemical Corp.*, the production of high quality (*i.e.* low-loss) laser-grade ceramics is still an art more than a science: production yields are low¹ and the process consistency is poor. The issue arises from the fact that for most multinary compounds, such as YAG or YIG, any departure from the phase stoichiometric composition strongly affects the optical properties of the material either through the formation of scattering centers (secondary phases and pores) or color centers (intrinsic point defects). In that sense, the optical quality of YAG is particularly sensitive to this effect due to the very narrow composition range that defines the garnet phase. Often described as a “line compound” in reference to the Al_2O_3 - Y_2O_3 phase diagram, recent studies have estimated the width of the phase domain to be on the order of 0.1 mol % [1]. In addition, it is interesting to realize that, contrary to the growth of single-crystals, which often involves the concomitant existence of a liquid-solid interface (at which impurities and extraneous phases can segregate out of the growing crystal), the fabrication of optical ceramics does not. This sets a more stringent requirement for composition control in transparent ceramics than for single-crystal growth. In the case of YAG ceramics, it is still common practice to use trial and error methods in order to hit the stoichiometric composition. This inevitably leads to deviation from stoichiometry from batch to batch.

The problem of non-stoichiometry in crystalline solids has a long history, dating back from the work of Berthollet in the 19th century, Kurnakow, Schottky and Wagner at the beginning of the 20th century [2]. As previously discussed, the dramatic implications of defects on the physical properties of materials is particularly well exemplified in transparent ceramics. In the case of YAG, for which Figure 1 shows a representation of a crystalline structure, three thermodynamically distinct stable phases occupy the yttria-alumina phase diagram, the other two being the yttrium aluminum monoclinic (YAM) phase and the yttrium aluminum perovskite (YAP) phase. The extent of the garnet phase is very limited in composition and appears, for that reason, as a line compound in the Al_2O_3 - Y_2O_3 diagram (see Figure 2).

¹ Konoshima Chemical Corp. reported YAG powder yields of about 20 % in 2009.

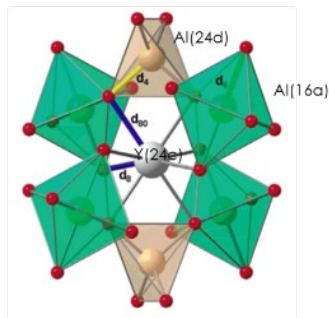
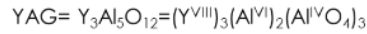


Figure 1: Crystalline structure of YAG.

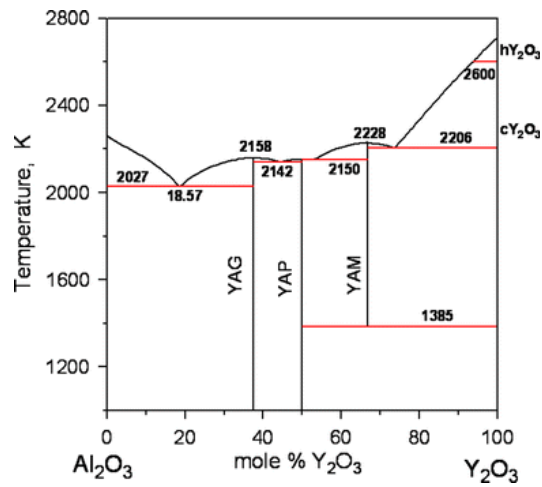
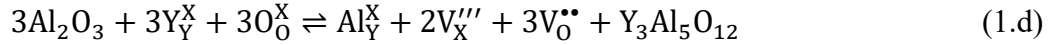


Figure 2: Alumina-yttria phase diagram. The YAG composition corresponds to 37.5 mole % of Y₂O₃.

The width of the YAG phase domain corresponds to a solid solution in which excess alumina or yttria is dissolved in the garnet lattice. The mechanisms by which this incorporation occurs have been discussed in several papers [1, 3, 4] and involve the formation of various intrinsic point-defects. The following Kröger-Vink equations are just a few examples of such mechanisms [5]:





As discussed above, these reaction equilibria have practical consequences in the fabrication of high quality YAG ceramics. The presence of these defects not only affects the sintering behavior of the ceramic by modifying the pore and grain boundary mobilities and therefore the ability to form a transparent body, but also introduces energy levels in the energy bandgap, which may result in undesired optical transitions in the absorption and emission spectra. Various factors may shift composition from stoichiometry or contribute to sample contamination:

- purity of the raw chemicals,
- precision in weighing. The balance has to have enough resolution to minimize uncertainties in mixing ratios,
- atmospheric humidity content as nanopowders have large surface areas and easily adsorb moisture,
- contamination from powder handling (ball-milling process, pressing equipment).

3.2 Accomplishments

Various improvements have been made to our YAG synthesis protocol to measure and control uncertainties leading to non-stoichiometry.

3.2.1 Roots of non-stoichiometry in the ceramic fabrication process

The aluminum to yttrium molar ratio (*i.e.* stoichiometric ratio) is defined as:

$$r = \frac{N_{Al}}{N_Y} = \frac{N_{Al_2O_3}}{N_{Y_2O_3}} \quad (2)$$

and the absolute error associated to this molar ratio is:

$$\delta r = \left[\frac{\delta N_{Al_2O_3}}{N_{Al_2O_3}} + \frac{\delta N_{Y_2O_3}}{N_{Y_2O_3}} \right] \left(\frac{N_{Al_2O_3}}{N_{Y_2O_3}} \right) \quad (3)$$

The three distinct parts of the reactive-sintering fabrication process that contribute to this error are discussed below.

Our approach was to identify and quantify each source of uncertainty and determine their contributions to a deviation from stoichiometry. Applying this insight, methods can be developed to minimize these errors sufficiently to repeatably produce laser grade YAG. We also define the limit of precision for this process.

The goal was to provide a framework for precise control of stoichiometry that can also be utilized in any material system, or application, that requires strict composition control. A simulation for the propagation of errors is presented that establishes an experimental approach to reducing these uncertainties (but does not eliminate them!). Achievement of this goal allows for better quality control and promote a more repeatable fabrication process.

3.2.2 Model Development: Propagation of uncertainty throughout fabrication process

There are three distinct parts in the reactive-sintering fabrication process that contribute to stoichiometry uncertainty.

The first is attributed to volatiles absorbed on the surface of precursor powders prior to weighing and mixing. The mass of these volatiles leaves the refractory powders upon firing and this volatile fraction is referred to as “loss-on-ignition” (LOI). Once the initial mass and final mass of the precursor oxide is measured the LOI can be determined by the equation:

$$LOI = \frac{m^f - m^i}{m^i} \quad (4)$$

Through this equation, the LOI is measured as a percentage of the initial mass that is lost during a thermal ramp. The uncertainty in the LOI measurement (δLOI) is taken as the standard deviation between consecutive LOI acquisitions of a single thermal ramp on the same lot of precursor powder.

The second contribution stems from weighting of the precursor powders on the balance to achieve the required molar ratio. Once the balance has been characterized, the uncertainty of each weighting measurement δm_{Bal} is the same. The balance has a maximum capacity not only in mass but in the area available to disperse the powder. For the batch size we work with, it is not possible to weigh all the necessary mass of each constituent in a single placement. The uncertainty will accumulate for each successive weighting on the balance (n_i).

The last contribution stems from the grinding medium (Al_2O_3 balls) used for attrition and intimate mixing of the precursor powders during the milling process. The abrasive nature of the precursor powders wears the surface of the balls. This causes some amount of excess alumina to be deposited into the powder mixture. This uncertainty is denoted $\delta N_{Al_2O_3}^{deposit}$.

Propagating all errors throughout the process gives a total uncertainty in the number of moles of each constituent as

$$\delta N_{Al_2O_3} = \left[\sqrt{n_{Al_2O_3} (\delta m_{Bal})^2} * m_{Al_2O_3}^{powder} \right] \left(\frac{1+LOI_{Al_2O_3}}{M_{Al_2O_3}} \right) + \frac{\delta (LOI_{Al_2O_3}) * m_{Al_2O_3}^{powder}}{M_{Al_2O_3}} + \delta N_{Al_2O_3}^{deposit} \quad (5)$$

and

$$\delta N_{Y_2O_3} = \left[\sqrt{n_{Y_2O_3} (\delta m_{Bal})^2} * m_{Y_2O_3}^{powder} \right] \left(\frac{1+LOI_{Y_2O_3}}{M_{Y_2O_3}} \right) + \frac{\delta (LOI_{Y_2O_3}) * m_{Y_2O_3}^{powder}}{M_{Y_2O_3}} \quad (6)$$

Upon determination of each uncertainty component, these two equations can be used to calculate the uncertainty in the molar ratio using Eqs. 5 and 6.

A polar plot representation of the phase diagram is shown below to visualize the spread of possible molar ratios obtained when considering the overall uncertainty of two constituents. The stoichiometric YAG composition is represented by a single orange line with a slope of 5/3. However, due to uncertainties, the final composition lies somewhere within the grey box. If the values of the LOI and Al_2O_3 deposit are known accurately, these considerations can be accounted for prior to batching.

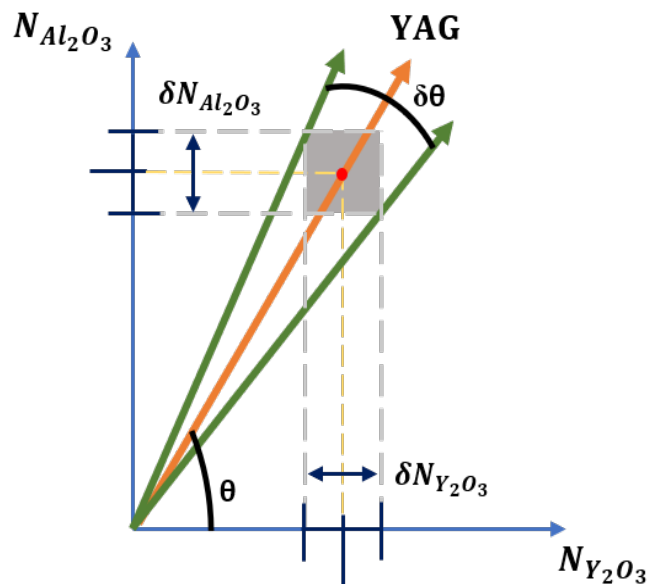


Figure 3: Polar representation of the phase diagram about the YAG composition, showing the range of possible final molar ratios that could be obtained when considering uncertainties on both the number of moles of Y_2O_3 and Al_2O_3 .

In what follows, we assume that all errors are random (*i.e.* not biased). Hence, by making multiple observations (replicates) and sampling random samples, we can build adequate statistics to help improve the repeatability of the fabrication process of TOCs. Randomness helps ensure the independence of weighing errors. This can be achieved by shaking bottles of raw powder reactants before sampling to minimize compositional non-uniformity due to moisture pickup, for example. Besides nonrandom sampling, care must be taken when compiling data over long periods of time as error independence may be compromised by the improving skills of the experimentalist at taking data (leading to decreasing errors) or the wearing down of the equipment (leading to increasing errors). It is under these conditions that all mass measurements are truly representative and share the same mean and variance, and that the errors are independent and identically distributed (IID). Below, we review some important notions of statistics which are used in our approach.

Given a sample of n observations, the sample average is calculated as:

$$\bar{x} = \frac{1}{n} \sum_{i=1}^n x_i \quad (7)$$

where x_i represents the i^{th} individual observation. The sample average is a statistic that is an estimate of μ , the mean (central tendency) of the underlying random variable, X . The sample variance is:

$$s^2 = \frac{1}{n-1} \sum_{i=1}^n (x_i - \bar{x})^2 \quad (8)$$

The sample variance is a statistic that is an estimate of the variance, σ^2 , of X . Another useful statistic is the sample standard deviation, s , which is the square root of the sample variance, σ . The quantity $n-1$ is the number of degrees of freedom associated with the sample standard deviation. In our case, we are specifically interested in the estimate of the mean and therefore the variance of the average value. This can be obtained by:

$$s_{\bar{x}} = \frac{s}{\sqrt{n}} \quad (9)$$

which also has $n-1$ degrees of freedom. Hence, when the number of observations is large, the uncertainty in the estimate of the mean is small. This relationship demonstrates that there is more uncertainty in an individual observation than in the estimated mean and that, even if the underlying phenomenon is quite variable, it is still possible to reduce uncertainty in the estimate of the mean by making many measurements.

In addition to those statistics, we want to infer the probability that a given random variable, such as a weighted mass or the Al/Y stoichiometry ratio, is within certain bounds. This requires an assumption about the shape of the probability distribution of the errors in experimental measurements. Most statistical techniques require that the errors, but not necessarily the random variable itself, have a normal probability distribution. As stated earlier, errors are both inherent variations in the random variable as well as measurement errors. The latter arises due to numerous small factors related to experimental protocols, sampling, detection, and analysis. However, since the experimental error is an aggregate of many contributing errors, then the overall error tends to have a normal distribution according to the central limit theorem, even if individual errors are not normally distributed themselves. Additionally, it is often the case that we don't have enough measurements to generate a normal probability plot and validate our assumption for the underlying probability distribution. For instance, LOI measurements are only based on a handful of replicates which makes it impossible to construct a meaningful probability plot. The amount of alumina contamination from milling is challenging to estimate and all the more is its error. In these cases, the central limit theorem provides a theoretical basis for assuming that the overall error is normally distributed.

For any estimated statistic, such as a sample average \bar{x} representing an average mass, LOI or Al₂O₃ deposit for which we have an estimated value and standard error, we can report confidence intervals. If the errors in the measurement variable, x , have a normal probability distribution and if the observations are independent, then the probability distribution for the error in the sample average, normalized by the standard error in the sample average, is a t -distribution. The t -distribution is a symmetric probability distribution centered at zero with a variance that depends on the degrees of freedom of the standard error in the statistic of interest. Since $s_{\bar{x}}$ has $n-1$ degrees of freedom, the variance of the t -distribution decreases with more measurements. The t -distribution is then used to determine a confidence interval for the true value of the mean, μ . For example, the $1-\alpha$ confidence interval for μ is obtained from the t -statistic which bounds a chosen level of probability, $1-\alpha$. For a symmetric two-sided interval with $\alpha/2$ probability level, this confidence interval is given by:

$$\bar{x} \pm t_{n-1, \alpha/2} S_{\bar{x}} \tag{10}$$

The confidence probability level can be chosen to be $1-\alpha=90\%$ (somewhat confident), 95% (fairly confident), or 99% (quite confident).

When estimating the error of a derived quantity, Z , function of n independent variables X_1, \dots, X_n , one can estimate the variance of Z from the sample variances of each of the measured variables x_i using:

$$\sigma_Z^2 = \sum_{1 \leq i \leq n} \left(\frac{\partial z}{\partial x_i} \right)^2 \sigma_{X_i}^2 \quad (11)$$

This result assumes small errors and no covariance between the random variables X_i . Hence, each independent variable X_i contributes to the variance of Z in two ways: (i) through its uncertainty σ_{x_i} , and (ii) through the sensitivity of z to x_i , $\partial z / \partial x_i$. This relation also shows that some terms (measurements) may carry more weight than others in improving the precision of the estimate of z .

For example, the variance of a weighted sum of n independent random variables:

$$Z = \sum_{1 \leq i \leq n} a_i X_i \quad (12)$$

is:

$$\sigma_Z^2 = \sum_{1 \leq i \leq n} a_i^2 \sigma_{X_i}^2 \quad (13)$$

Similarly, the relative variance of a weighted product:

$$Z = \prod_{1 \leq i \leq n} a_i X_i \quad (14)$$

is given by:

$$\frac{\sigma_Z^2}{Z^2} = \sum_{1 \leq i \leq n} a_i^2 \frac{\sigma_{X_i}^2}{x_i^2} \quad (15)$$

The ratio $\sigma_{\bar{x}} / \bar{x}$ can be estimated by $s_{\bar{x}} / \bar{x}$ if replicate measurements have been acquired.

We hypothesize that the weighing and LOI measurements are normally distributed and so is the mass of Al_2O_3 released by milling.

A Monte Carlo simulation was written to determine the probability of the final molar ratio falling at a given composition. The inputs of this model are based on mean and uncertainty values determined experimentally. This simulation can help calculate the occurrence of the many compositions (Al/Y ratios) one would get by combining these errors. The results of these simulations are shown below in Figure 4. To a good approximation, the distribution of compositions (histograms) also seem to follow a normal distribution and were fitted accordingly. As expected, larger uncertainties on the relative amount of alumina-to-yttria translate to wider composition uncertainties for the final ceramic and increase the risks of synthesizing 2-phase (*i.e.* non-transparent) ceramics when the ensemble of possible compositions exits the solid-solution domain of the garnet phase (Figure 4b).

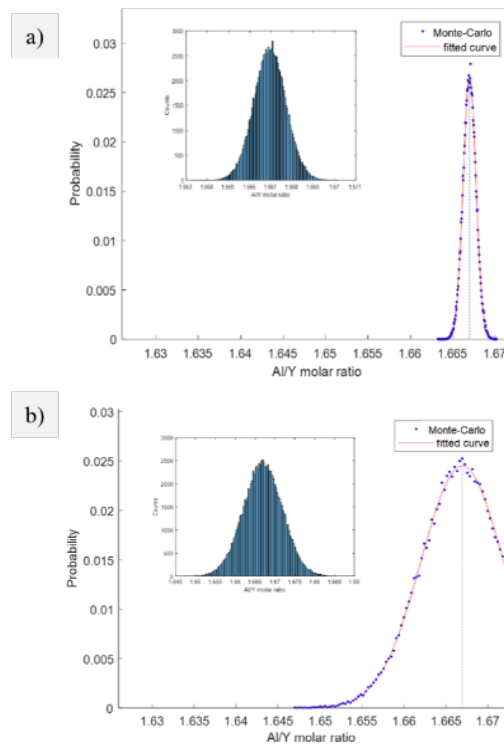


Figure 4: a) Histogram (inset) and normalized probability for obtaining varied yttrium-aluminum garnet compositions after repeating 105 Monte-Carlo “syntheses” in-silico. The following assumptions are made based on experimentally determined measurements (see sections above): weighting uncertainty 2.15×10^{-4} g, $\text{LOI}(\text{Al}_2\text{O}_3) = 0.658 \pm 0.032$ %, $\text{LOI}(\text{Y}_2\text{O}_3) = 0.690 \pm 0.014$ %, Al_2O_3 deposit is 0.439 ± 0.005 g for 40 g of $\text{Al}_2\text{O}_3 + \text{Y}_2\text{O}_3$ mixture. Powders are weighted by 5 g increments. The nominal YAG composition has an Al/Y ratio of $5/3 = 1.666$ (vertical dashed line) and the range of compositions shown corresponds to the estimated width of the solid-solution domain for the garnet phase around the sintering temperature (1750°C). Here, all compositions are within the solid-solution window and should yield single-phase garnet ceramics. b) Same simulation as in a) but with an Al_2O_3 deposit uncertainty ten times higher of 50 mg. In this case, some compositions fall outside the solid-solution window (on the Al-rich side) and are expected to yield two-phase ceramic mixtures of YAG and alumina.

The fraction of the histogram overlapping with the solid-solution window corresponds to the probability that, with these experimental uncertainties, the batch of mixed oxides yields a transparent ceramic. This probability can be used as a “metric of success” to quantify the respective roles of weighting errors, LOIs and alumina deposit errors in the process.

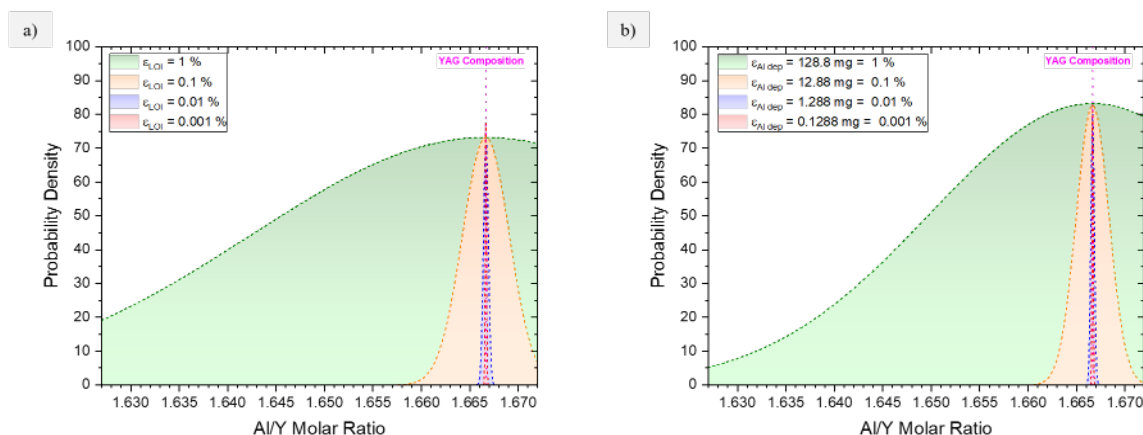


Figure 5: (a) Probability of obtaining a composition within the solid solution, the range shown, when LOI uncertainty varied between 0.001-1%, with uncertainties for both precursors taken as equal. Assumes a batch size of 30 g, the mean LOI values are both set to 2%, and the Al_2O_3 deposit error is set to zero. (b) Probability of obtaining a composition within solid solution, the range shown, when Al_2O_3 deposit error varied between 0.001-1%. Percentages are taken relative to the stoichiometric mass of Al_2O_3 for a batch size of 30 g and the LOI errors are set to zero.

The models for both plots above assume a batch size of 30 g mixed to the stoichiometric YAG composition and a mean LOI value of 2%. Model (a) shows the effect on the probability of obtaining a molar ratio inside of the solid solution when the LOI errors are varied between 0.001-1%. While model (b) shows the effect on this probability when the Al_2O_3 deposit error is varied by the same percentage, relative to the stoichiometric mass of Al_2O_3 in YAG. The red curve in both plots approaches a distribution from only the weighing of the powders. The fraction of these distributions that overlap with the solid solution window corresponds to the probability that the batch of mixed oxides yields a transparent ceramic. The LOI distribution is broader than that of the Al_2O_3 deposit distribution at 1%. Additionally, the right side of the LOI distribution still lies outside of the solid solution at 0.1%, this is not the case for the Al_2O_3 deposit. *This demonstrates that while it is important to precisely determine the uncertainties for both of these contributions, it is more important to do so for the LOI values in order to increase the probability of fabricating transparent ceramic YAG.* Maintaining this increased probability of obtaining a target ratio is necessary to ensure repeatability of the process and will allowing targeting compositions for studying the effect of non-stoichiometry on the transparency of parts and the control of the defects generated within the solid solution.

The authors recognize that this is a first order approach, with the stated assumptions, and that with more sampling the distributions can be further refined.

Identification of the sources of error, and related uncertainties, in the fabrication process is important in ensuring repeatable product quality. The development of this model allows for assessing the relevance of each source of uncertainty. Once this relevance is determined, approaches can be developed to reduce the uncertainties that bring the largest contributions, thereby increasing the repeatability of product quality.

3.2.2.1 Measurement of uncertainty from balance

The error attributed to weighing powders on a balance arises from two sources: the error inherent to the balance itself and the repeatability in depositing the powder to the same location on the balance. The error inherent to the balance is defined by both its accuracy and precision. The repeatability error, on the other hand, is user-based, and arises from our inability to control how the particles distribute themselves in space about the pan. This spatial distribution changes the location of the center-of-mass of the pile of powder relative to the center of the balance pan, generating a moment. Uneven loading of the pan results in measurement inconsistencies hereafter referred to as the ‘sand pile effect’. The unrepeatability of the sand pile effect should bring increased uncertainty, as opposed to placing a standard mass at the same spot even time.

To confirm this hypothesis, two separate yet similar experiments were conducted to quantify the uncertainty for each scenario. The benchtop balance was calibrated with calibrated masses prior to conducting any experiment. During the experiments, the atmosphere in the lab space was controlled so that no vibrations or changes in air pressure due to fume hood sash configuration affected the results.

In the first experiment, we investigated the repeatability and accuracy of the balance. To do so, a 5 g calibrated mass applied to the surface of balance while keeping its location constant from trial to trial. This was repeated for a total of 50 trials.

The sand pile effect was tested using coarse rock-salt that had been equilibrated with atmosphere to ensure the sample mass was constant throughout the test. A chosen sample mass of approximately 5 g is utilized. This is equivalent to the approximate maximum mass of powder applied to the balance, for a single weighing during the YAG fabrication process, which we are trying to calibrate. The rock-salt was placed on a piece of wax paper, the mass registered and then the mass was removed. This process was conducted for a total of 50 trials. The distribution of the mass measurements as registered by the balance for both experiments are shown in Figure 6. Both plots are presented on the same scale ranges.

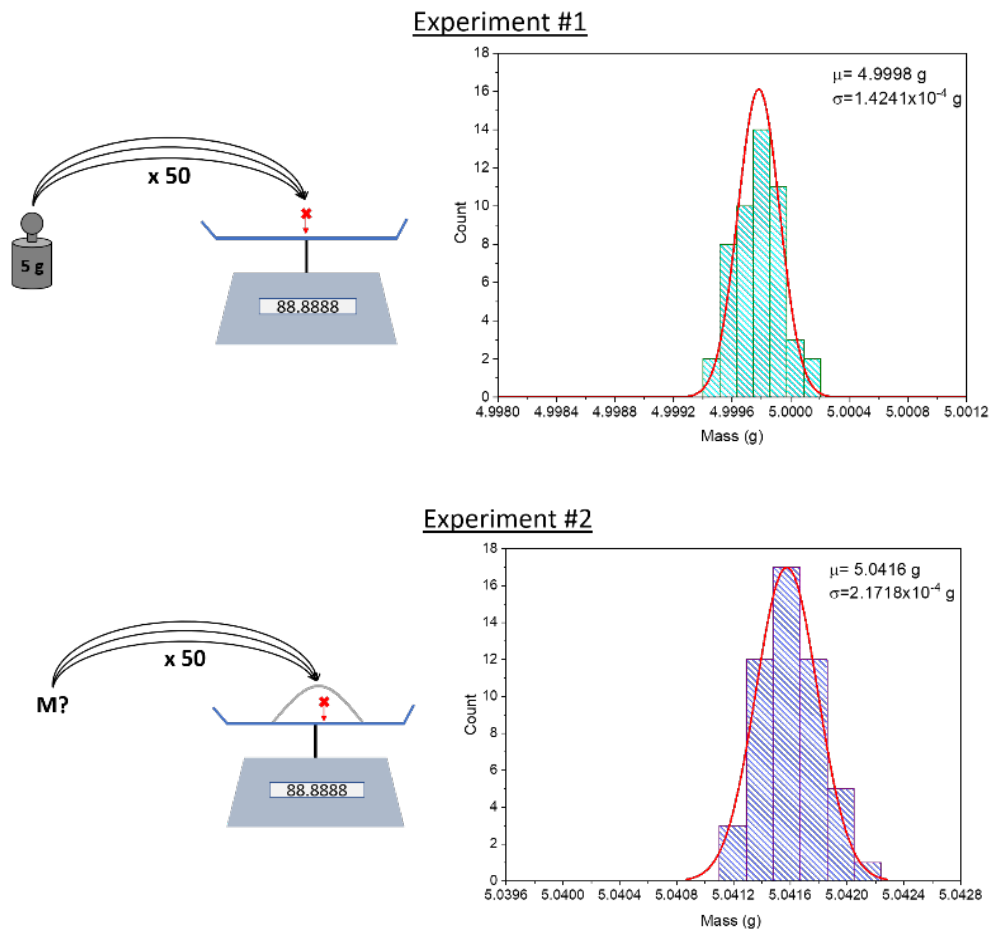


Figure 6: Distribution of mass registered during experiments to characterize the balance accuracy, precision and sand pile effect.

For the first experiment with the standard mass, there is a fair fit to a normal distribution. Based on the fit, the accuracy of the balance differs by 0.2 mg from the expected value of 5.0 g. The standard deviation at one sigma is 0.14 mg. This is just slightly larger than the resolution of the readout on the balance.

The second experiment investigated the ‘sand pile effect’ and produced a distribution with a range 33% larger than that of the distribution produced by a standard mass placed at constant location on the balance. The standard deviation at one sigma is $\sigma_{\text{SPE}}=0.22$ mg. This distribution tends to a normal distribution (central limit theorem). However, like the first experiment, increasing the sample size will produce a more robust distribution and provide a better fit.

We hypothesize that the ‘sand pile effect’ is the dominant contribution to the uncertainty on these powder weighing measurements. For this reason, the only error to be considered for propagation analysis is that of the ‘sand pile effect’.

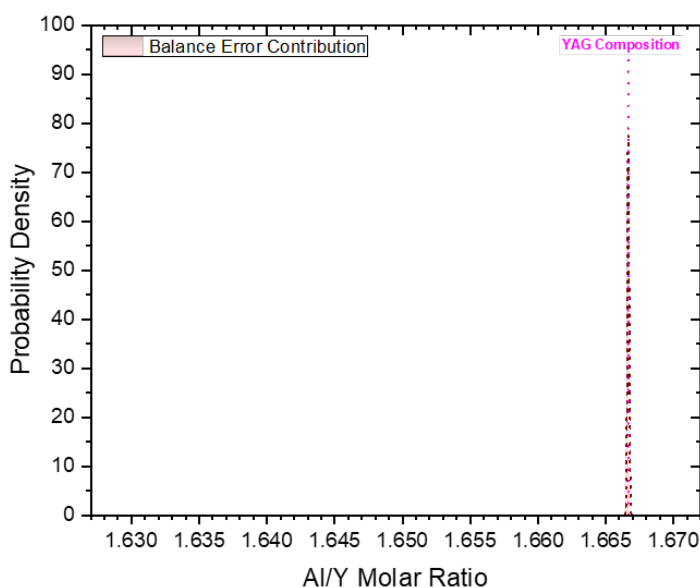


Figure 7: Contribution of the uncertainty from only the error attributed to sand pile effect the occurs during weighing powders on a balance.

The range of molar ratio when balance error becomes the limit of the uncertainty reduction is 1.66637 – 1.66696, which is a range of only $5.9 \cdot 10^{-4}$. This represents the limit to which the uncertainty can be collapsed as it will be much smaller than the other uncertainties contributions introduced in subsequent sections. A total process uncertainty of this magnitude would be adequate to always guarantee transparent parts and to precisely target distinct compositions within the solid solution.

The uncertainty attributed to a pile of particles randomly dispersed across the balance plate has a larger variance in the moment applied, compared to placing a mass repeatability in the center of the plate. Of all uncertainties identified in the process, this is the smallest contribution. If there were only this uncertainty, the probability of stoichiometry and transparent parts would be virtually 100% so long as the rest of the process is optimized.

3.2.2.2 Contamination from grinding media

The reactive sintering fabrication route of transparent YAG ceramics requires the mixing of precursor yttria and alumina powders followed by a ball milling process to ensure deagglomeration and intimate mixing. High purity aluminum balls are used as a grinding medium to prevent the addition of impurities outside of the Al_2O_3 - Y_2O_3 system during this operation. However, due to the abrasiveness of the powder, the grinding medium slowly wears

and introduces extraneous alumina to the powder mixture which results in an increase of the $\frac{N_{Al}}{N_Y}$ ratio.

Ideally, the milling process is optimized to achieve satisfactory deagglomeration and mixing while limiting the alumina deposit to a negligible amount. The optimization of this process is time consuming and requires running many experiments to determine the best of combination of the many interdependent variables involved. These variables include the mass of powders, the solid loading fraction of the slurry, the surface area of milling medium, dimensions of the jar, the duration of milling, the speed of rotation and the ball-to-powder loading fraction. Even if satisfactory attrition and mixing is achieved, the amount of alumina deposit should be quantitatively measured, or verified to be negligible, so any deposit can be considered prior to mixing of another batch to ensure stoichiometry is achieved. Additionally, it was shown in the prior section that the amount of uncertainty in the measurement has a significant effect on total uncertainty of the process, and the probability of achieving transparent YAG.

To the best of our knowledge, no studies published to date provide all the parameters used during the milling process when producing YAG. Lui *et al* [6] completed the most comprehensive study on the subject and correlated the milling time to the resulting transmission in Nd:YAG transparent ceramics. In their study, the diameter of milling media, rotation speed, mass ratio of balls to powder, and solid loading was published, but not the dimensions of the jar. In 2009, Lee *et al.* [7] completed a study on hot isostatic pressing of Nd:YAG ceramics and published the milling time, diameter of milling media, and the volume ratio of powder:media:solvent. Stevenson *et al.* [8] published the same information in a 2011 investigation on the effect of SiO₂ and densification of Nd:YAG ceramics. Yet, no rotation speed, jar dimensions, or batch size were given in these publications. Most authors having published on the fabrication of YAG transparent ceramics by reactive sintering, including Boulesteix *et al.* [9] or Bonnet *et al.* [10], give no milling information at all. Adding to this complication is different groups use different types of milling equipment (i.e. rotary or planetary ball mills.)

Additionally, to the best of our knowledge, no study has been published that has addressed quantifying the amount of contamination from grinding media during the milling process. In the past, we have attempted to quantify this deposit by qualitative visual inspection of sintered samples from past batches. A batch of varying composition is made with known mean initial molar ratios. After sintering, it is assumed that the most transparent samples are closest to stoichiometric YAG. The difference between stoichiometric YAG ($r = 5/3$) and the previously calculated ratios of these samples is then taken as a consequence of the alumina deposited during milling. The amount of deposit to cause this shift in transparency is then calculated. In actuality, this difference in transparency could also come from difference in porosity or thermal gradients between parts during sintering [11]. Not only that, but this method becomes even less reliable when considering the distribution about the mean of the final composition based on the uncertainties, as discussed previously.

Another method that has been used to determine the amount of deposit is to run the mill with only the alumina balls and a solvent present in the jar. After a set milling time the balls and jar

are rinsed into a catch and the solvent is evaporated. Weighting the remaining solid gives the mass of alumina removed from the balls during that run time. The figure below shows the results of these trials.

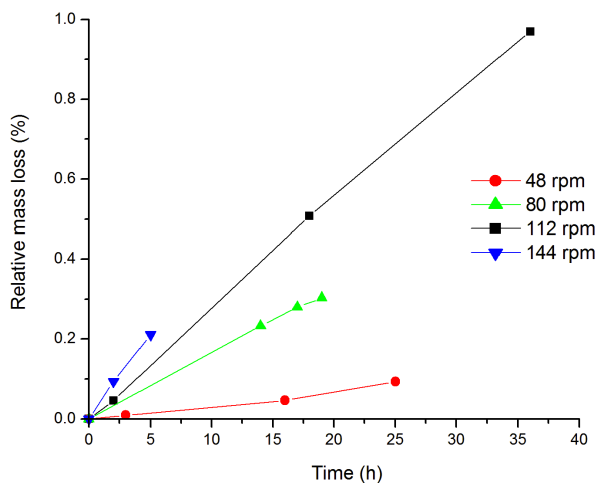


Figure 8: Mass loss of alumina balls versus time for different ball mill rotation speeds when only milling media and solvent present in jar during the run.

The problem with this method is that it does not mimic the interaction between the abrasive powder and the balls during milling, but only the interaction between the balls themselves. This fact makes the values obtained unreliable. Directly measuring the mass of a powder mixture after milling is not a solution either as this Al_2O_3 deposit represents such a small mass increment to the powder mass making it impractical to measure.

Studies have been done using tracers to measure particle motion and attrition during the milling operation, generally for industrial applications [12-15]. The utilization of radioactive tracers brings health and safety concerns that would not allow completion of this study in a typical lab space. One could imagine working with radioactive tracers for quantification, but this would bring the added difficulty of precisely monitoring decay time of the isotope, from the time the balls are doped through when any measurement is taken.

We are currently developing a simpler approach inspired by these methods and hope to get, for the first time, a unique and accurate determination of the total amount of alumina deposited during milling.

3.2.2.3 Protocol for the measurement of loss-on-ignition of starting powders

Fine starting powders enhance the kinetics of ceramic sintering, but their large surface area makes the powders susceptible to holding significant amounts of volatile species remaining from synthesis or adsorption of moisture during stocking, handling, and storage when exposed to humidity in the local atmosphere. Upon firing, the mass of the volatiles will be removed prior to phase formation and is therefore referred to as loss-on-ignition (LOI). Hence, the excess mass must be accounted for during batching to ensure the ability to repeatably fabricate parts within the solid solubility domain. The LOI should be quantified upon receipt of new powders and repeatably in time as the hydration of the powders surface can change with dynamic atmospheric conditions.

The preferred method for quantifying LOI is through thermogravimetric analysis (TGA) which monitors the mass loss of a sample during a programmed thermal ramp or cycle within a controlled atmosphere as a function of both time and temperature. It is common for the TG signal to be acquired simultaneously with differential scanning calorimetry (DSC) or differential thermal analysis signals (DTA), TGA-DSC and TGA-DTA respectively. DSC will acquire a heat flow signal during the thermal treatment while DTA records the temperature difference of the sample relative to a reference. Through these combined analyses it is possible to identify physical transitions and chemical reactions that do not necessitate a mass loss. Some of the properties or processes that can be characterized are thermal decompositions, melting points, glass transitions in amorphous materials, crystallization behavior, solid-solid transitions, among others [16, 17]. TGA can also be coupled with evolved gas analyzers (TGA-EGA) allowing for residual gas analysis through the identification and quantification of the various gaseous species that are volatilized during the thermal treatment. Fourier-transform infrared spectrometers (FTIR), mass spectrometers (MS), gas chromatographs (GC), or a combination of these can be attached to the TGA instrument to quantify decomposition by-products down to concentrations on the ppm level [18].

TGA is used in applications such as assessment of pyrolysis characteristics of fuels [19-21], mineralogical analysis of geological samples [22-24], analysis of thermal degradation in polymers [25-27], production of pharmaceuticals [28, 29], among many others. In the ceramics industry it is typically utilized for determining the decomposition temperature of organics used during wet chemical synthesis or of binders used in the forming process to optimize the burnout cycle before phase formation and sintering [30-38]. In these applications the mass loss is more dramatic, and they require much less precision than when being used for strict control of composition in reactive sintering.

Many people have made transparent YAG ceramics via reactive sintering but there are very few mentions of quantifying the LOI values of the precursors prior to mixing. We hypothesize that the reasons for not reporting this could be: (i) the LOI is not measured or considered, other processing errors are low, and transparent parts are obtained with mixed success, (ii) this value is measured but not disseminated as it is a protected part of the recipe in producing transparent ceramics, (iii) it is measured but there is little emphasis placed on it because it is thought of as a

‘common knowledge’ not worth reporting in a publication. The second or third possibilities seem to be the most reasonable. In literature there is also no mention of the repeatability in the quality of the samples produced.

The only mention of considering LOI values comes from a single group where they describe a basic technique to measure weight loss in a powder compact of the precursor on a benchtop balance. The compact is fired in a furnace, allowed to cool to 200°C, placed in a desiccator until it reaches room temperature, and then the final mass is again weighed on a benchtop balance [39-43]. While this does provide a measurement of the LOI, the accuracy and precision may be less than that which is offered by a thermogravimetric instrument. This is attributed the immediate re-adsorption of moisture when the powders are again exposed to an atmosphere with a higher moisture content. The plot below shows the mass variation as a function of time for a powder that was equilibrated in oven for two days then placed on a balance under ambient conditions. The ambient temperature was 20°C with a relative humidity of 60%.

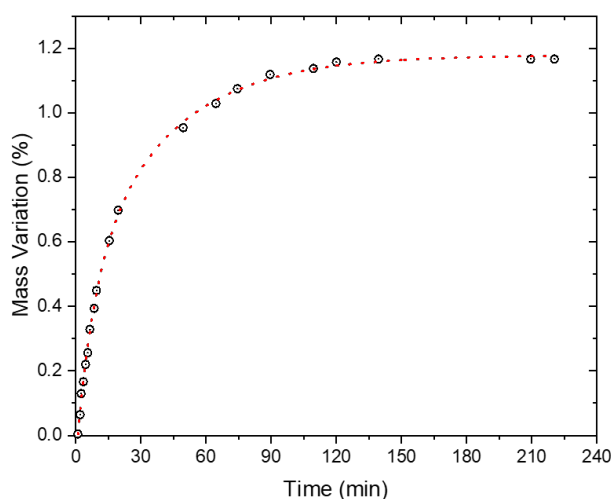


Figure 9: Mass variation of Y_2O_3 powder left on a balance for 3 hours at 20°C and in a relative humidity of 60%. The powder was dried in an oven for two days at 70°C prior weighing.

The plot shows how fast powders can re-adsorb moisture from the atmosphere in ambient conditions. Consequently, acquiring accurate or repeatable measurements via this technique would be challenging. This approach also convolutes the contributions of the balance and LOI errors.

The model introduced previously shows that obtaining accurate measure of the LOI values plays a significant role in reducing the overall uncertainty to give an increased probability of attaining stoichiometry, and the ability to target specific compositions within the solid solution. Therefore, to bring more repeatability to the process, not only is it imperative that the LOI be

considered prior to batching but the uncertainty of this measurement should also be minimized. It is worth mentioning that this is not only true for the reactive sintering route but that this would hold true for the other powder synthesis methods too.

We hypothesized that a TGA instrument, which is typically used for more coarse quantification of mass loss, can be used to reduce the statistical composition variations and accomplish the necessary precision to target compositions well within the limited solid solution domain of YAG.

The approach is to first assess the suitability of this instrumentation to achieve a magnitude of error necessary to repeatably achieve parts within the solid solution. Secondly, if the instrument is deemed suitable then develop a protocol that enables targeting of distinct compositions within the solid solution.

The instrument we have used for TGA is the SDT-Q600 (TA Instruments, USA), depicted below. This simultaneous TGA/DSC/DTA instrument houses two balanced beams, which hold a reference and a sample crucible in a furnace chamber. The temperature of the furnace is cycled up and down, and the change in mass of the sample, relative to that of the reference, is recorded as a function of the sample temperature and time.

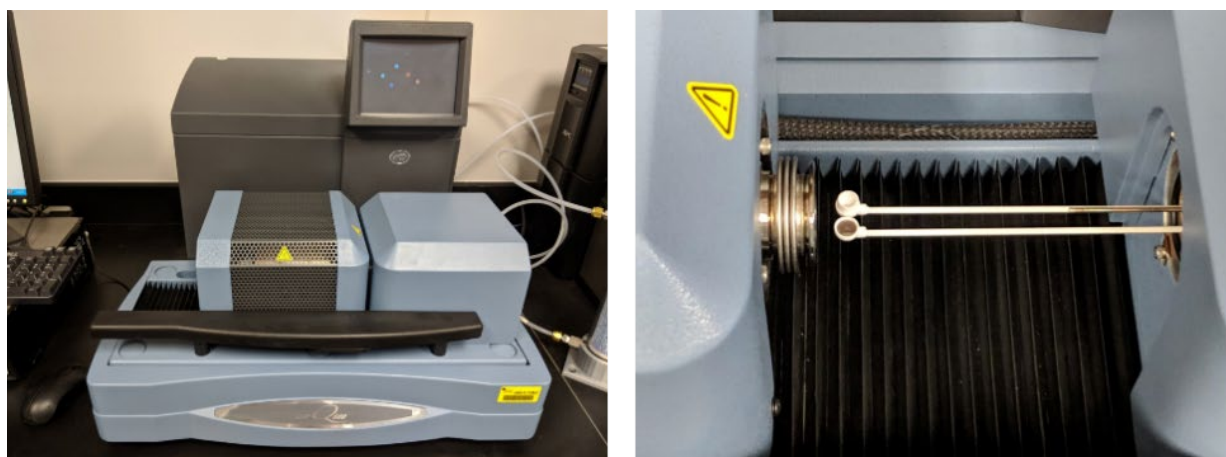


Figure 10: (left)TA Instruments SDT-Q600, (right) sample and reference beams.

Following the protocol as described in the manual, nitrogen is used as a purge gas with a flow rate of 100 mL/min and a heating ramp rate of 3°C/min is used up to 1200°C. The final mass is taken at the end of the heating ramp. This does not deviate significantly from protocols published in literature. Based on the Ellingham diagram, these refractory oxides are stable, and decomposition is not expected at these temperatures and oxygen partial pressures. Three consecutive runs from the same lot are executed for both powders, alumina and yttria. The LOI values for the Al₂O₃ powder is determined to be 0.777 ± 0.089 %, and the Y₂O₃ is 0.78910 ± 0.046 %. The Monte Carlo simulation of the LOI and balance uncertainty contributions are shown below. The balance uncertainty contribution is shown for reference.

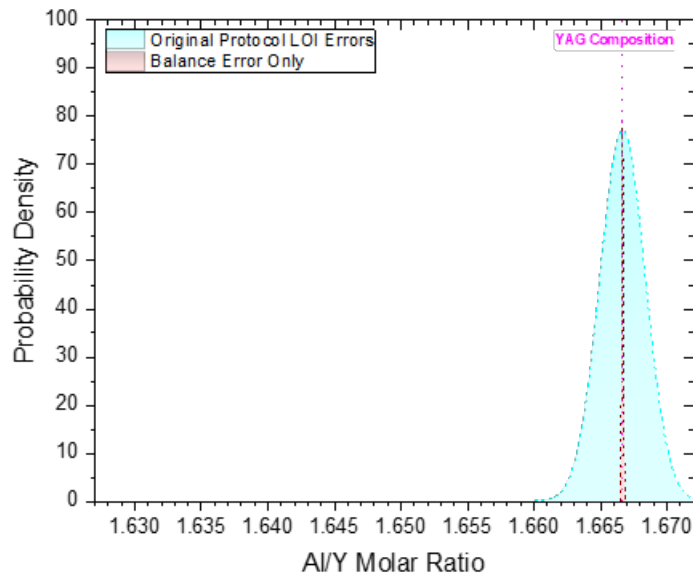


Figure 11: Probability of obtaining a composition within the solid solution, the range shown, when LOI values determined using protocol described in instrument user manual and literature.
 Al_2O_3 LOI = 0.777 ± 0.089 % and Y_2O_3 LOI = 0.789 ± 0.046 %.
 Balance contribution is shown for reference.

The plot shows that, so long as the LOI is considered, the combined uncertainty from just the LOI values yields a distribution that practically guarantees a composition within the solid solution. However, it is still a wide distribution, relative to the uncertainty of the balance contribution.

To determine if the uncertainty could be reduced further the mechanics and operating principle of the horizontal beam system is considered. The mechanics are based on the concept of a cantilever beam. Shown below, is an image of the dual horizontal beam system employed SDT-Q600.

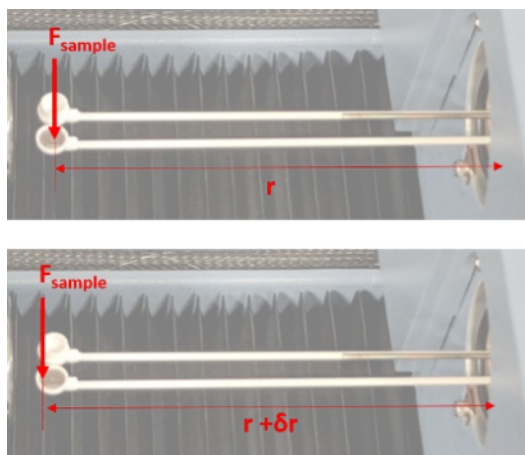


Figure 12: Image of dual horizontal beam TGA system on SDT-Q600, showing the moment arm and effect of cup moving during thermal cycling.

The beam in the back is the reference beam where an empty crucible is placed during the experiment. The mass signal produced is the difference between this reference beam and the sample beam, in the front, where a crucible loaded with the sample is placed. On the platforms there is room for the thermal expansion and contraction of the crucible during thermal cycling. However, this also allows room for the crucible to “walk”. Small displacements of the crucibles that can occur during the thermal cycle, δr , is amplified in the signal by the long moment arm. “Walking” crucibles introduces a mass gain/loss, in addition to the volatilized mass loss, that is dependent on the direction of movement. Therefore, the crucibles were “pinned” to the back of the platform with small pieces of platinum wire during the high temperature ramps, as shown in the figure below.



Figure 13: TGA crucibles pinned to back of platform with platinum wires attached to exterior wall of alumina crucible.

Acquiring a signal with powder present in the crucible presents the largest complication to reducing this error further. Some of our precursor powders sinter during the thermal ramp, Al_2O_3 in particular, which reduces the volume of the sample inside crucible at the elevated temperatures required for this analysis.

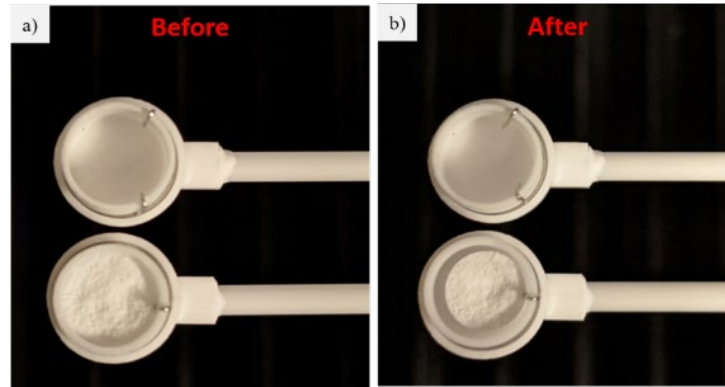


Figure 14: (a) Al_2O_3 powder in flat bottom crucible before thermal cycling, (b) Sintered Al_2O_3 powder that has walked inside crucible after thermal cycling.

As the powder sinters during the thermal ramp, the sintered body can move concomitantly within the crucible. Walking of crucibles on the platform can be minimized but controlling the movement of the sintered sample inside the standard flat-bottom crucibles is more challenging. Several experiments were run to assess the impact of sample movement during the acquisition on the LOI measurement.

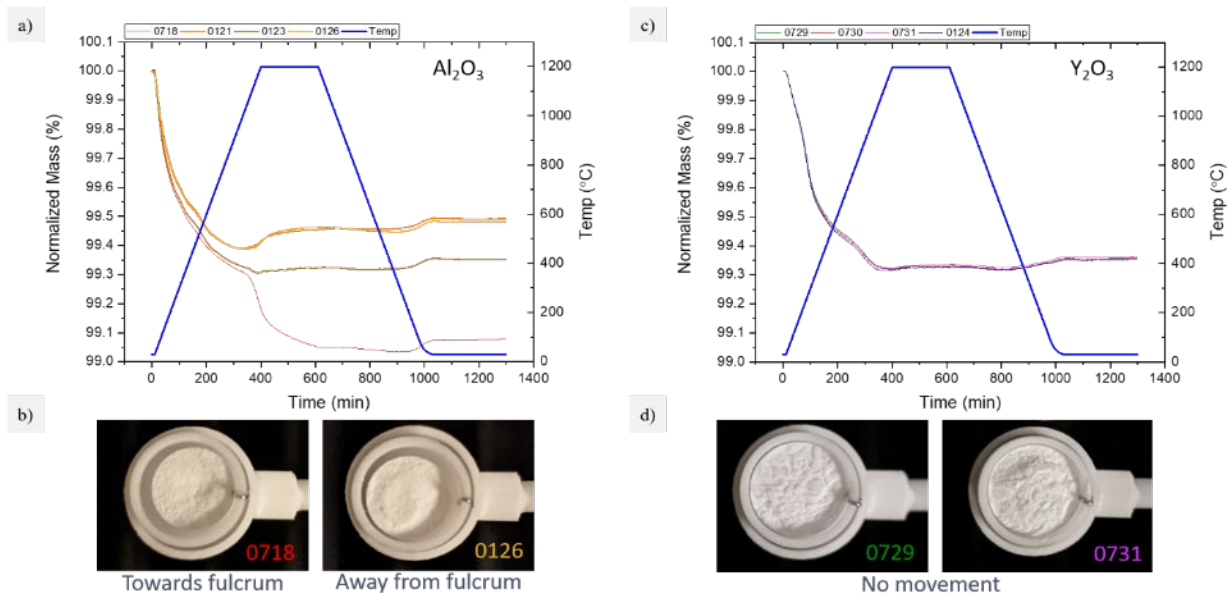


Figure 15: (a) Mass loss versus time signals for consecutive runs of Al_2O_3 powder of same lot showing significant variance in trends between each run. (b) Position of sintered bodies of Al_2O_3 after thermal cycling, colored labels correlate to experiment number on plot. Number 0718 has moved forward towards the fulcrum of the cantilever beam. Number 0126 has moved backwards away from the fulcrum of the cantilever beam. (c) Mass loss versus time curves for consecutive runs of Y_2O_3 powder of the same lot showing minimal variance in trends between each run. (d) Position of sintered bodies of Y_2O_3 after thermal cycling, colored labels correlate to experiment number on plot. All samples run in this experiment exhibit minimal sintering or movement within the crucible.

During all runs shown in the plots on in Figure 15, the cups were pinned to the back of the beam. Figure 15a shows the TG curves for aluminum oxide powder from the same lot and the magnitude of LOI variations associated with walking of a sintered sample. Uncertainty on the LOI values amount to as much as 0.27% in the worst case when the sintered body attaches to the either the front or rear wall. This variation stems from the part walking towards or away from the fulcrum of the cantilever beam during the cycle (Figure 15b) causing the center of mass to change which affects the moment. As a direct consequence it makes it seem as though, in addition to the LOI, mass is lost/gained during the run. To contrast, as shown in Figure 15c and Figure 15d for consecutive runs of Y_2O_3 powder of the same lot, the samples do not experience significant volumetric contraction and is not able to walk within the cup. The TG trends stack on top of each other producing an uncertainty of only 0.002%. Therefore, the movement of a sintered sample within the crucible produces an uncertainty that is more than an order of magnitude larger than that achieved by a sample which does not move.

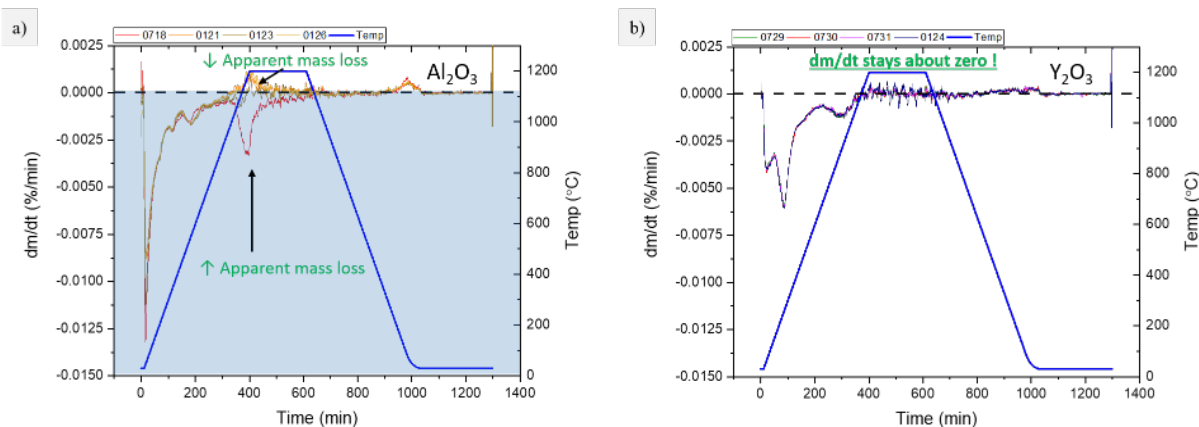


Figure 16: (a) Rate of mass change for consecutive runs of Al₂O₃ powder of same lot. Showing that for large negative peak for number 0718 which attached to the wall of the crucible closest to the fulcrum of the beam and exhibited significantly increased weight loss. Numbers 0121 and 0126 moved away from the fulcrum of the beam and then would exhibit a decrease in apparent mass loss (b) Rate of mass change for consecutive runs of Y₂O₃ powder of same lot showing that dm/dt curves stay about zero.

Figure 16a shows the mass rate of change plot for consecutive runs of Al₂O₃ powder from the same lot. Number 0718, which moved toward the fulcrum of the beam, shows a large negative peak. The sample experienced an increase in the apparent weight loss, additional to the loss due to release of volatiles on the surface of the powder. Numbers 0121 and 0126, which moved in the opposite direction, show peaks in the positive direction. These samples experienced a decrease in the apparent mass during the thermal ramp. The plots also show that movement begins well below the maximum temperature. To contrast, Figure 16b shows the same mass rate of change plot for consecutive runs of Y₂O₃ powder from the same lot, that experienced minimal volumetric contraction. These trends approach zero prior to reaching the maximum temperature and maintain this position throughout the period at high temperature. The Y₂O₃ experiments provided a much more precise measurement than those with Al₂O₃.

An experiment was devised to attempt to control the movement of the Al₂O₃ powder where a 1 mm diameter Pt-Rh pin was positioned in the bottom of the flat bottom crucible to force the powder to sinter around it and impede the movement of the sintered body.

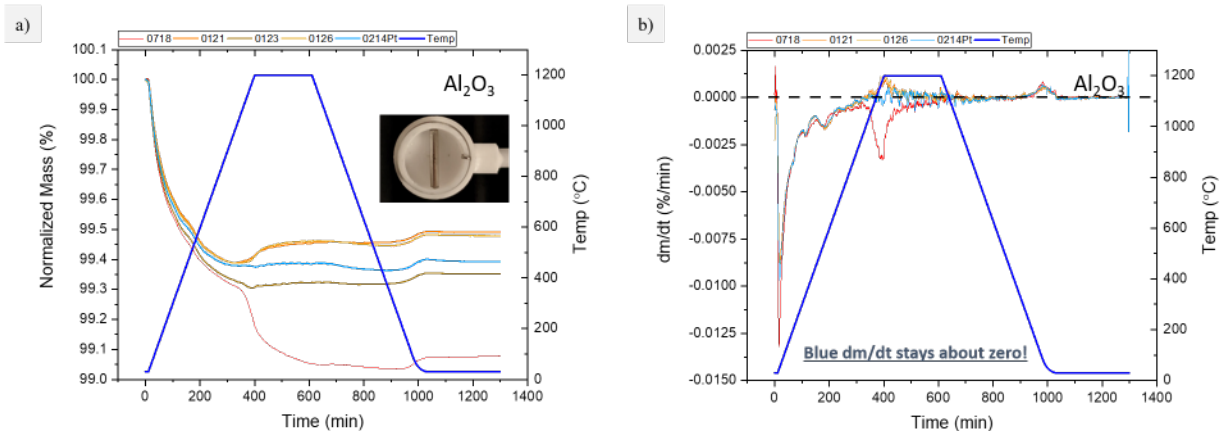


Figure 17: (a) Mass loss versus time signals using standard flat bottom refractory crucibles (same as previous figure) compared to the light blue curve which has the same thermal cycle using the anti-walk/self-centering device. Inset image is a Pt-Rh wire installed in the standard crucible oriented perpendicular to the fulcrum of the beam (b) Rate of change of mass for several signals (same as above figure) with the light blue curve added. Showing that when the anti-walk/self-centering device is employed the light blue curve stays about zero with no major peaks above or below, indicating no added/subtracted apparent mass loss due to sample moving within refractory crucible.

Figure 17b shows that when the Pt-Rh is employed (light blue curve) during the measurement the dm/dt curve approaches zero even before reaching high temperature and stays about this location throughout the time it is held at high temperature. This experiment indicates the device is successful in maintaining the location of the center of mass while the powder sinters throughout the thermal cycle. Figure 17a shows the difference between the LOI values that would be obtained when the device is employed (light blue curve) versus when there is no device to control the movement of the sample. Further experiments will be conducted to verify the repeatability of this measurement.

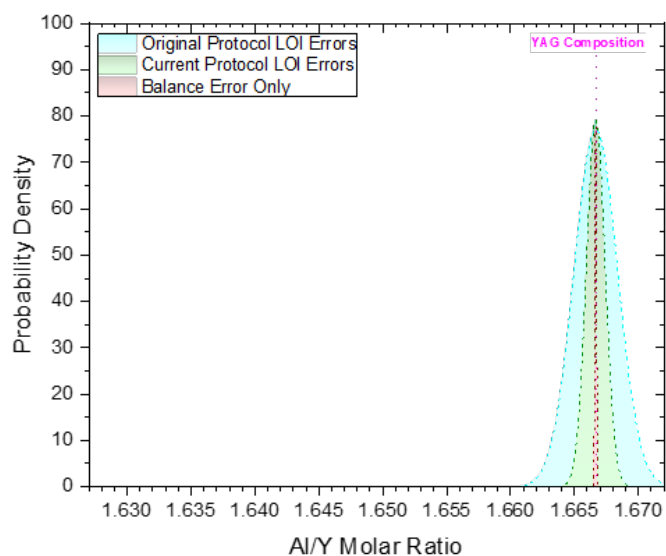


Figure 18: Probability of obtaining a composition within the solid solution, the range shown, when LOI values determined using revised protocol with pinned crucibles and a Pt-Rh pin installed to prevent walking of sintered sample. Al_2O_3 LOI = 0.681 ± 0.043 % and Y_2O_3 LOI = 0.680 ± 0.002 %. Balance contribution is shown for reference.

The uncertainties obtained with the revised protocol provides an uncertainty of 0.681 ± 0.043 % for Al_2O_3 and 0.680 ± 0.002 % for Y_2O_3 . The uncertainty on the Y_2O_3 is an order of magnitude lower compared to the initial protocol, without pinning the crucibles. The figure above shows that this has significantly reduced the combined uncertainty contribution of the LOI values.

It is promising results that the Pt-Rh wire prevents walking of the sintered body within the crucible, but it was noted that the powder did not sinter uniformly about the Pt-Rh wire which can alter the obtained final mass. There are also concerns of the difference of CTE between the Pt-Rh wire and the alumina cup stressing the crucible, and the uneven heating of the powder due to the presence of the metal wire. To address this, we have designed an anti-walk and self-centering refractory crucibles that would force the powder to sinter in the center of the cup, thereby maintaining the location of the center of mass. An invention disclosure for this device has been filed and accepted by the UCF Technology Transfer Office. Due to the ongoing legal processing of this filing, we cannot release the designs for this device.

This device will further increase the accuracy and precision on the loss-of-ignition values obtained when measurements are performed on powders that sinter nonuniformly or walk during thermal ramping in a standard flat bottom crucible. We believe that, once manufactured, this invention will provide the necessary control to reduce the Al_2O_3 LOI uncertainty to the same order of magnitude as that of Y_2O_3 . The combined LOI uncertainties from both constituents will

collapse to be just larger than the minimum uncertainty brought from weighing the powders on the balance.

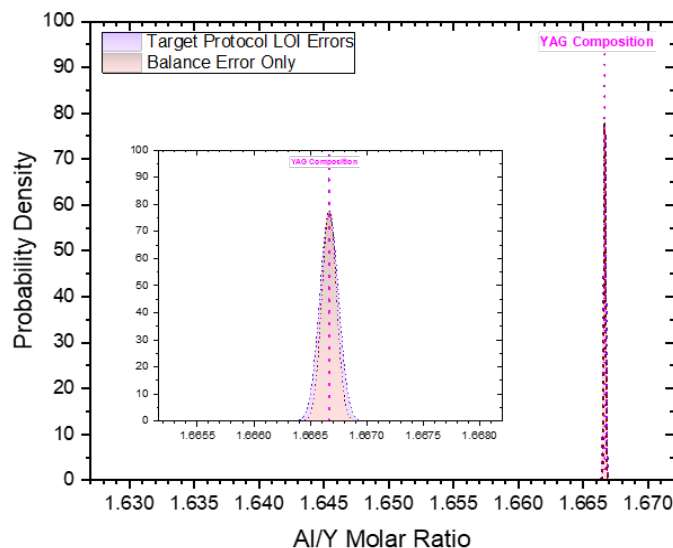


Figure 19: Probability of obtaining a composition within the solid solution, the range shown, when LOI values determined using with pinned crucibles and novel anti-walk crucibles. Assuming Al_2O_3 LOI = 0.681 ± 0.004 and Y_2O_3 LOI = 0.680 ± 0.002 . Balance contribution is shown for reference.

The accuracy and precision of this loss-of-ignition measurement is critical to increase the statistical probability of achieving stoichiometry and to repeatably obtain the desired optical properties in the product ceramic. To extend this further, there is a finite minimum uncertainty required to ensure the composition remains in the solid-solubility domain of the YAG phase but further minimization of the LOI uncertainty is required to control defects such as quenching centers that may occur within this domain.

The TGA analysis of nano-particles, on a dual beam thermal analyzer and for the purpose of quantifying LOIs is more sensitive than with coarse particles not only because (1) they have more surface area and experience more desorption, but (2) they also have a tendency to sinter and walk during the thermal cycle. While we can minimize the walk of the crucibles on the platform by pinning them, it is more difficult to control the movement of the sintered sample inside this crucible. A possible approach to limit this effect would be to utilize crucibles designed to self-center the powder during the thermal cycle.

3.2.2.4 Summary: Propagation of error throughout the fabrication process

In the preceding sections we have presented the development of a novel approach that facilitates the assessment of uncertainty propagated throughout the ceramic fabrication process and its correlation to the probability of repeatably achieving a composition within the solid solution. This approach established an experimental approach to reducing these uncertainties.

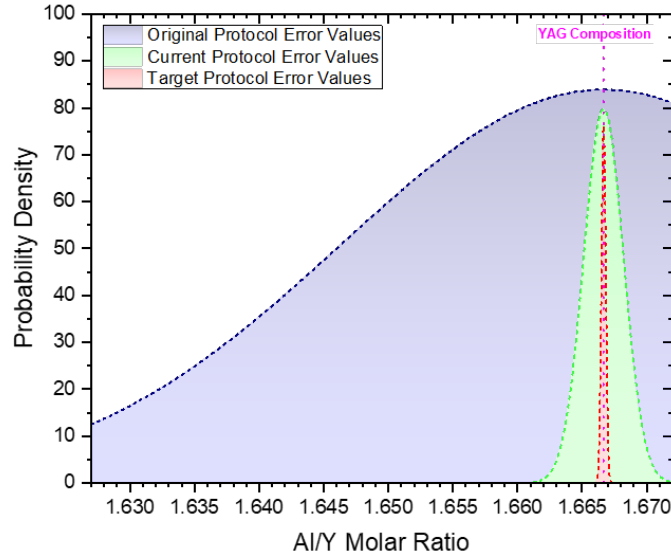


Figure 20: Probability of obtaining a composition within the solid solution, the x-axis range shown. The blue area depicts the original protocol, green area the current protocol, and the red area the target protocol for the given application of targeting distinct compositions well within the solid solution.

The figure above depicts the total process uncertainty and its effect on the probability of achieving a composition within the solid solution of YAG. The blue area is the probability distribution attained by following the original protocol. The uncertainty values are attained by following the LOI protocol given in literature and the instrument user manual. Thus, producing LOI uncertainties of $\pm 0.090\%$ for Al_2O_3 and $\pm 0.046\%$ for Y_2O_3 . With a limited sampling based on the transparency shift in a series of parts of varied composition the ball mill Al deposit was assessed with an uncertainty of 35%. This distribution is much broader than the solid solubility domain and does not guarantee a transparent part. The green area represents the probability distribution achieved with a revised protocol. The LOI values are achieved by pinning the cups and the application of the Pt-Rh pin during the Al_2O_3 acquisition. These changes produce uncertainties of $\pm 0.043\%$ for Al_2O_3 and $\pm 0.002\%$ for Y_2O_3 . The ball mill deposit is determined to be $\pm 5.34\%$ of the deposit value based on a broader sampling of parts and referencing the model. If a part is visually determined to be stoichiometric then the right wing cannot extend past the right side bound of the solid solution. Based on the total uncertainty assessed, this provides a

distribution that guarantees a composition within the solid solution, and a transparent part. The red distribution emanates from a target protocol in which the Al_2O_3 LOI uncertainty is reduced to the order of magnitude of the current Y_2O_3 using the novel anti-walk crucible and the ball mill deposit is quantified within 5% via an analytical assessment. This protocol would allow for targeting of numerous distinct compositions within the solid solution for defect engineering.

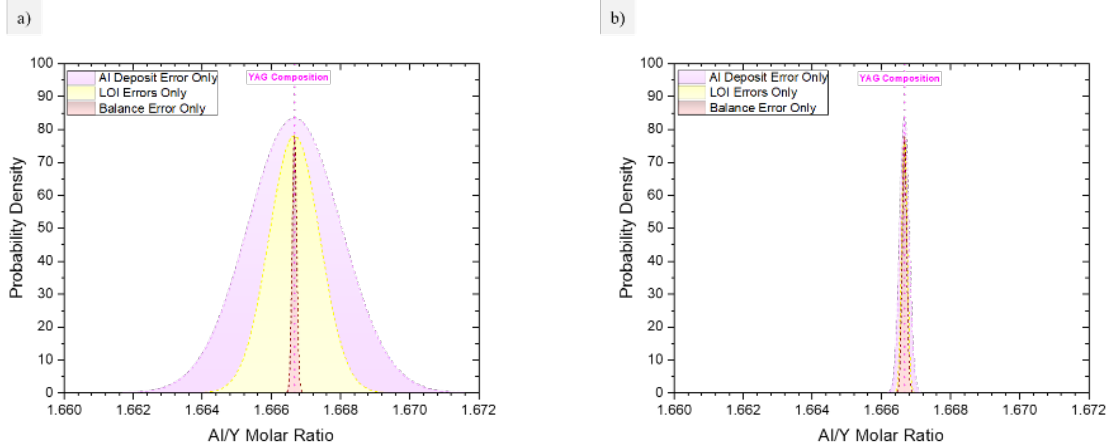


Figure 21: Contributions to the probability distribution from each of the uncertainty sources at (a) current protocol (b) target protocol. Note the right bound is the limit of the transparent regime but the total range is much smaller than the solid solubility domain.

The figure above depicts the contribution to the total uncertainty from each source and final composition probability distribution. Figure 21a shows that with the current protocol, as described above, the uncertainty related to the Al dep from the ball mill is the main contributor to the increased uncertainty. Additionally, the combined uncertainty of the LOI values is still much larger than that from weighing the powders on the balance. Figure 21b shows the contributions to the probability distribution if the target protocol is achieved. The ball mill deposit is still the main driver but is significantly reduced and the LOI contribution is virtually collapsed to the width of the balance contribution.

This novel statistical analysis approach demonstrates that if the uncertainty sources within the fabrication process are identified and quantified then parts within the limited solid solubility domain can be repeatably achieved. This achievement lays the framework to provide more repeatable quality of transparent ceramics, and other multinary compounds. Additionally, it provides a methodology to assess and further reduce uncertainty contributions. Thereby, making targeting of distinct composition within the solid solution possible. Finer scale defect engineering would be facilitated in this material system as well as other systems with limited solubility domains such as YIG, GAGG, ect. The amount of necessary precision depends on the specific application, and some may only care to guarantee to be within solid solution. However, this lays the groundwork for better quality control and promotes a more repeatable fabrication process.

3.2.3 Contamination free powder mixing process

We were given the opportunity to demo a piece of equipment (ARE-310) from *Thinky USA* that is able to mix powders without the use of grinding medium². The operating principle of this mixer relies on high rotating speeds (up to 2000 rpm) and large inertial forces to stir particles. However, because there is no grinding medium, little or no attrition is available to reduce the size of hard agglomerates (comminution). For reference, the current planetary ball mill used in our process has a maximum speed of 590 rpm. We thought of using this opportunity to test the possibility of achieving adequate **intimate** mixing of the constituent powders and possibly substituting ball-milling by this contamination-free powder mixing process.

Our time-limited experiments sought to investigate the optimal rotation speed and milling time to achieve phase pure and high-density ceramics. The solid loading fraction of the slurry was held constant and the same as our normal process. We chose to investigate the upper regime of rotation speeds (1200 – 2000 rpm) as we felt it would be necessary to have the higher energy that would be needed to break up agglomerates present in the raw powder. Fifteen separate 20 g batches were made up, with the composition set at stoichiometry ($r_{Al/Y} = 5/3$) because there would not need for any consideration of alumina deposit during milling. After milling, each batch of powder was processed through the same fabrication protocol used when we utilize the planetary ball mill. The parts were formed by cold uniaxial pressing in a 20 mm die to a thickness of approximately 3 mm, then sintered under vacuum at 1750°C for 12 hours. Table 1 identifies each sample, lists mixing parameters and the relative density after sintering as determined by Archimedes' principle. The measured density was taken relative to that of pure YAG (4.56 g/cm³.)

Table 1: Summary of milling parameters for parts mixed without grinding medium, including relative density achieved.

Part #	Mixing time (h)	Mixing speed (rpm)	Relative density after Sintering (%)	Comment
2	1	2000	93.70	
3	4	2000	97.99	
4	1	1600	93.92	
5	1	1200	93.29	
6	2	1600	92.27	
7	2	1200	93.02	
8	4	1600	94.27	

² <https://www.thinkymixer.com/en-us/product/are-310/>

9	4	1200	93.29	
10	0	0	85.16	Control – No Mixing
12	0.25	1200	91.21	
13	2	2000	93.46	
16	0.25	1600	93.21	
17	0.25	2000	94.56	

After sintering none of the samples were visually transparent, but some showed highly dense regions (Figure 22).

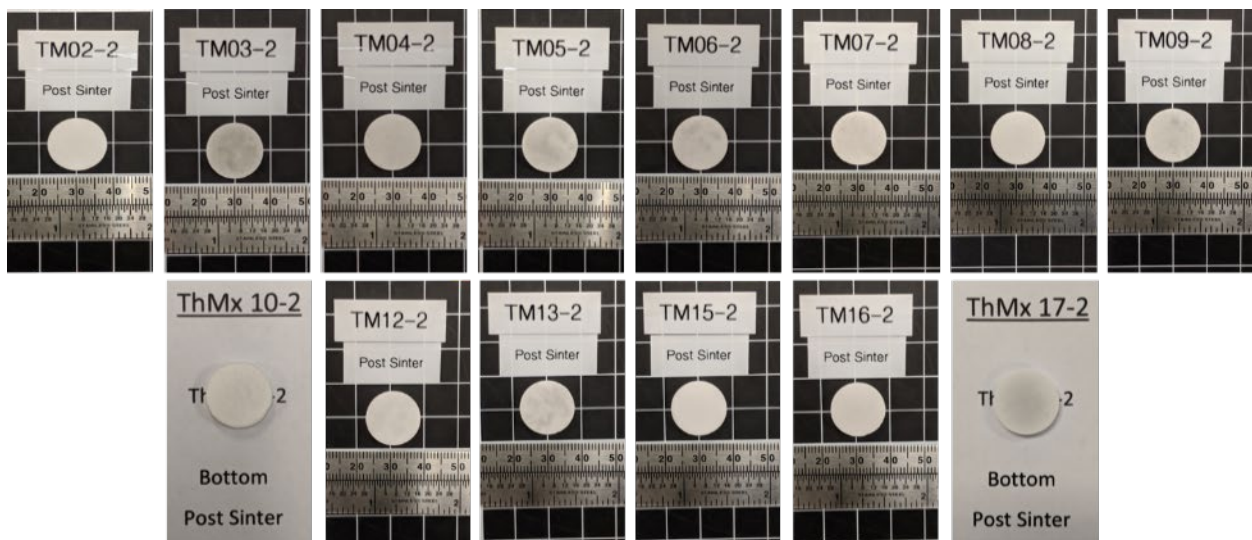


Figure 22: Sintered YAG ceramics made by powder mixing without milling medium.

The relative density of each part is plotted as a function of milling time in Figure 23. The rotation speeds are also listed to the right of each data point. This plot shows a positive correlation between the mixing time (and rotation speed) with higher ceramic densities, with 98% dense ceramics obtained at 2000 rpm after 4 hours of mixing. Unfortunately, due to the limited duration of this demo, we were not able to probe longer mixing times at high rotation speeds and have a chance to approach even higher densities.

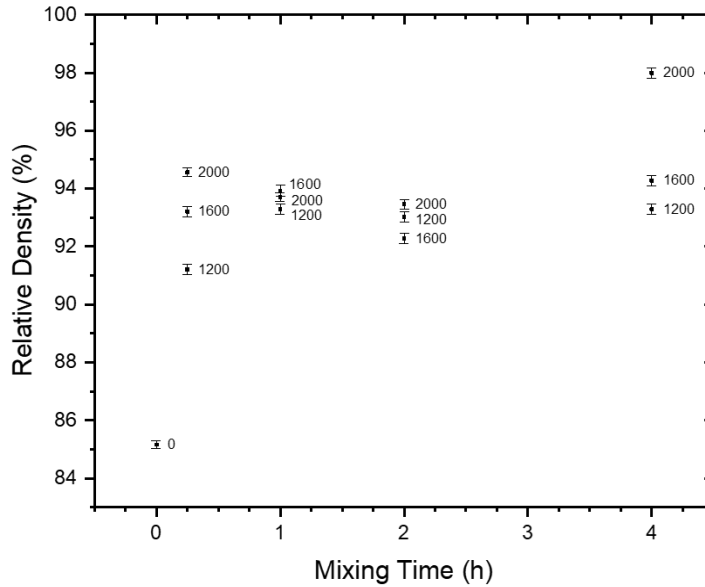


Figure 23: Relative densities of sintered YAG ceramics made by reactive sintering as a function of mixing time for powders processed without grinding medium. A control sample made by shaking powders by hand (mixing time: 0 h) achieves 85 % relative density.

X-ray diffraction (XRD) was performed on six parts with the highest densities, to check for phase purity. Examples of the diffractograms obtained are shown in Figure 24. The diffractograms all show secondary phases of $YAlO_3$ (YAP) and $Y_4Al_2O_9$ (YAM) suggesting that intimate mixing was not achieved in the conditions we have tested. Out of all samples, sample #3, which was mixed for 4 hours at 2000 rpm, has the least YAP phase.

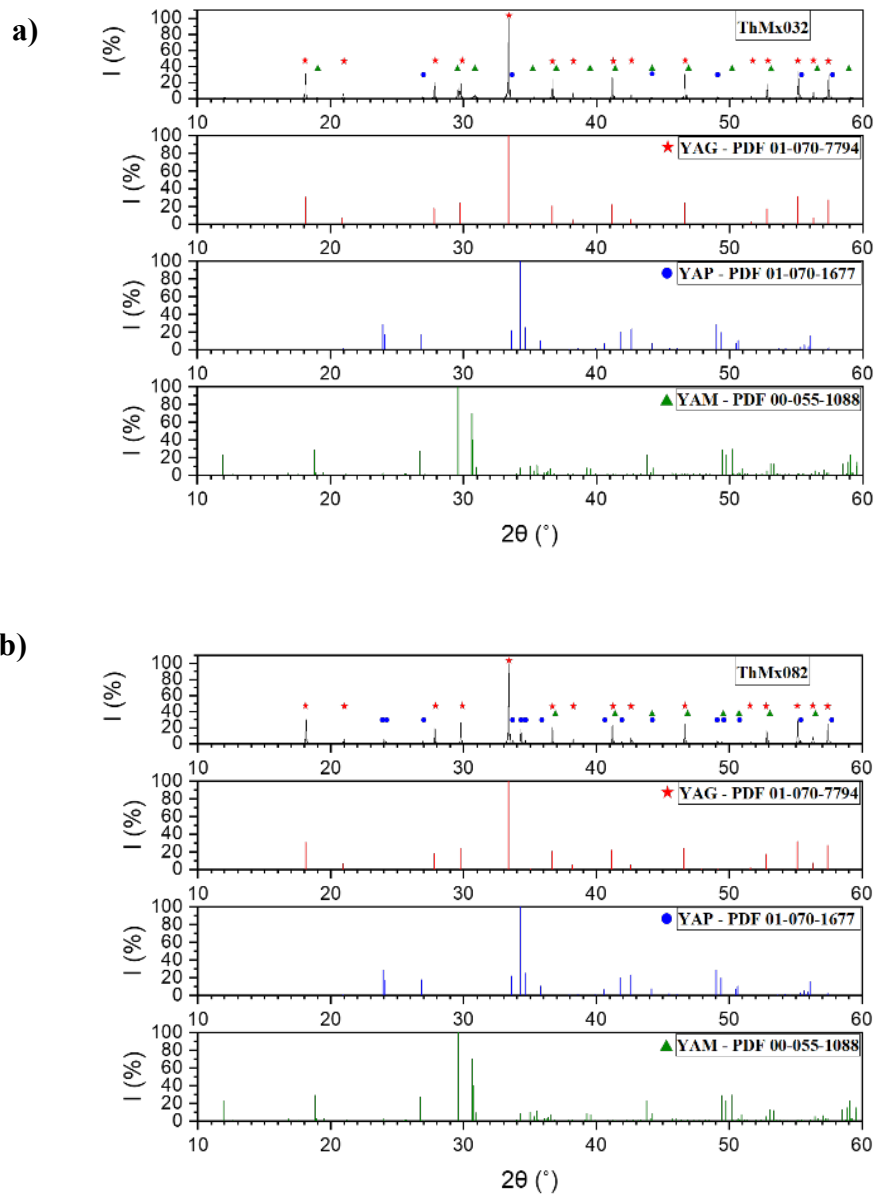


Figure 24: XRD patterns for: a) part #3, mixed for 4 h at 2000 rpm and b) part #8, mixed for 4 h at 1600 rpm. Reference patterns for YAG, YAlO_3 (YAP) and $\text{Y}_4\text{Al}_2\text{O}_9$ (YAM) are given to qualitatively assess the phase purity of these sintered parts.

The particle size is expected to be a little larger than our normal process because no milling medium was used. Therefore, we hypothesized that maybe not enough time was allowed for the YAG phase to form at the intermediate hold temperature (1450°C, 1h) before ramping to the sintering temperature of 1750°C. New samples were made from the remaining powder from batches #3 and #8, which were the samples with the highest densities. The hold time at the intermediate temperature was doubled to 2 hours. After sintering, the samples were again

analyzed by XRD for phase purity. Figure 25 shows the acquired XRD diffractograms for both parts.

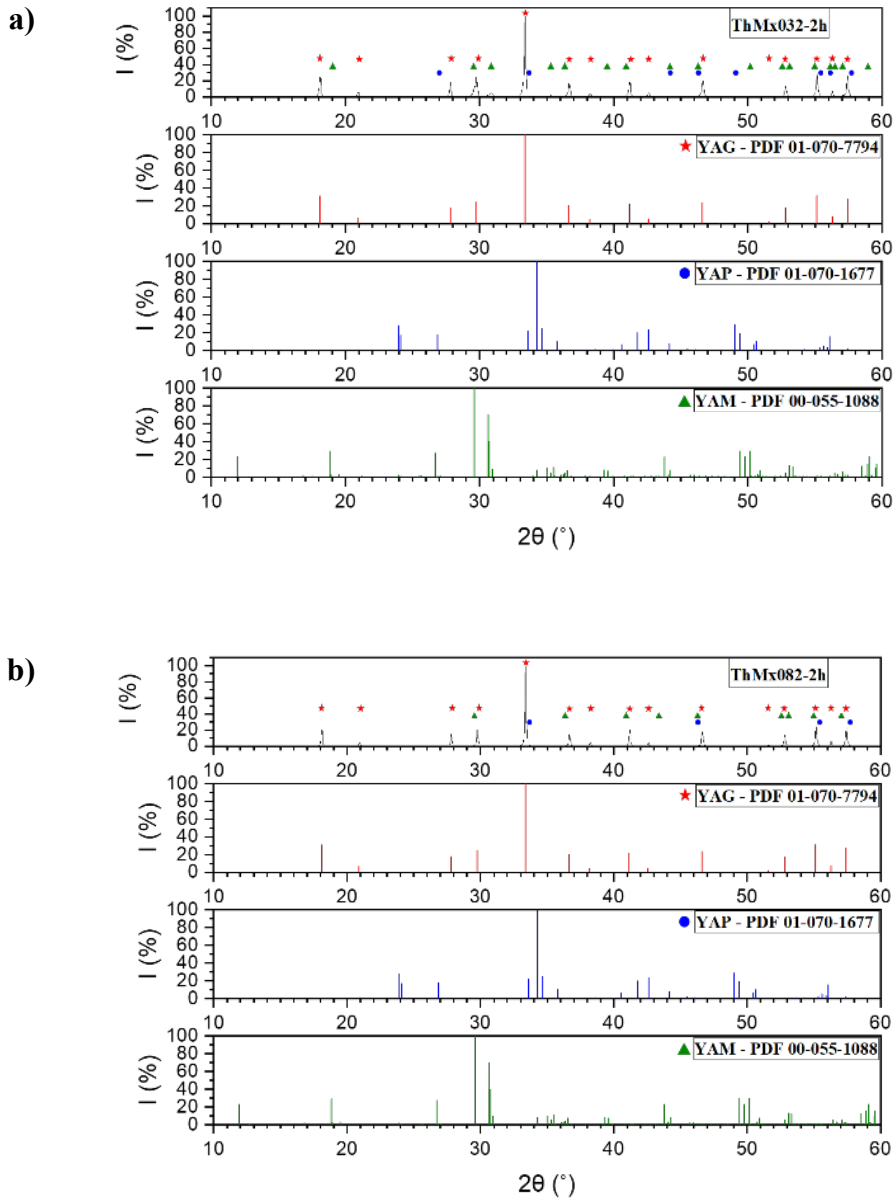


Figure 25: XRD patterns for ceramics sintered with an extended hold time at 1450°C. a) Part #3, mixed for 4 h at 2000 rpm, b) part #8, mixed for 4 h at 1600 rpm.

As seen in the above diffraction patterns, both parts still have YAP and YAM secondary phases present. Whereas the extended hold time reduced the amount of YAP present in part #8, it did not affect the phase purity of sample #3. This leads us to believe that these secondary phases

are brought about by regions of local non-homogeneities because the mixing was not intimate enough or because some agglomerates were left after milling.

Since most vacuum-sintered parts achieved closed-porosity (~92%), the samples were subsequently hot isostatically pressed at 1700°C, 200 MPa for 4 hours to see if further densification could be obtained. Images presented in Figure 26 are some of the parts after this post-processing.

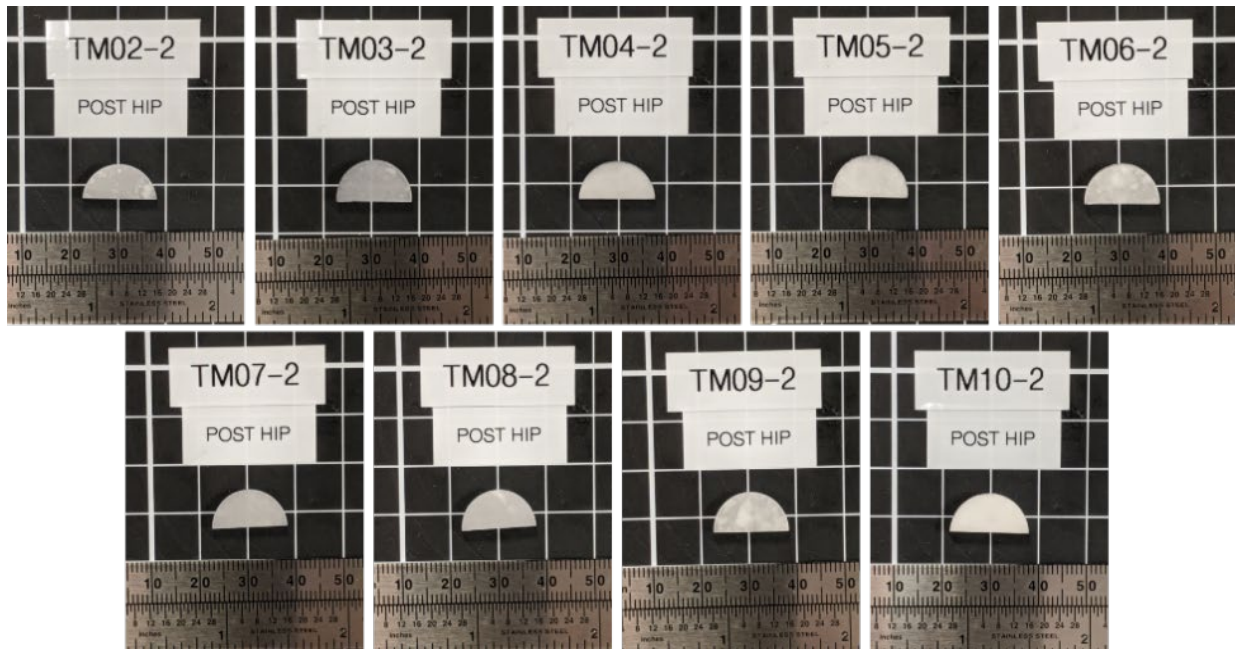


Figure 26: YAG ceramics made by contamination-free powder mixing after sintering and HIP'ing. All samples are 2 mm thick.

Part #3 had the best response after the post processing. This part is highly translucent with some haziness. Some of the other parts also showed local transparent regions but contained white “blotches” throughout. This is another indication of localized inhomogeneities and that agglomerates are likely still present after the mixing process.

Despite its potential benefits in other applications, our investigations suggest that this mixing technology, in its present development state, is not sufficient to provide both intimate mixing and de-agglomeration for the fabrication of TOCs by reactive sintering.

3.2.4 Particle size and morphology characterization of as-received precursor and processed powders

In the fabrication of transparent ceramics, the particle size and morphology of the precursor powders is very important for achieving fully dense, highly transparent parts. Powders with a narrow size distribution, small particle size ($<1\mu\text{m}$), roughly spherical shape, and soft or no agglomeration of particles are generally preferred for advanced ceramic fabrication. Small particles have a high surface area to volume ratio, which implies a high amount of surface energy per volume. The large amount of surface energy is a driving force for sintering, during which the surface energy is reduced. The use of small particles allows for high density to be achieved in a relatively short amount of time. A narrow size distribution allows for good control of the microstructure, so that coarsening, and grain growth is homogeneous throughout the ceramic. In the case of reactive sintering of YAG ceramics, alumina and yttria particles must be well mixed so that the local environment on the nano-scale fulfills the stoichiometric ratio of 5:3 for Al:Y, otherwise various Al- and Y-rich phases will form where the local environment is off stoichiometry for YAG. This is a problem that can be caused by agglomeration of alumina or yttria particles forming large agglomerates that cannot be well-mixed. This problem is mitigated in our YAG processing by ball-milling the precursor powders together, which is meant to break up agglomerates and provide intimate mixing and possibly reduce the particle size. Through electroacoustic measurements and scanning electron microscopy (SEM), our goal was to characterize our precursor powders and determine the effect of ball-milling on the particles. This could help with optimizing the ball-milling parameters and verifying the consistency in precursor powders. It is desirable to use the least aggressive ball-milling parameters possible to achieve the desired effect on the particles to minimize contamination of the powder with material from the grinding media, which can throw off the stoichiometry of the batch.

3.2.4.1 Experimental

The precursor powders Y_2O_3 (Alfa Aesar, 99.99%), Al_2O_3 (Taimei Chemicals Co., LTD., 99.99%), and Tm_2O_3 (American Elements, 99.99%) were observed with an FE-SEM (SIGMA, Zeiss, Germany). The particle sizes of the yttria and alumina powders was analyzed using electroacoustic and ultrasonic attenuation measurement equipment (AcoustoSizer II, Colloidal Dynamics, USA) and the accompanying software. The powders were measured at 2 wt% loading fraction in ethanol separately and 1 wt% loading fraction each (2 wt% loading fraction of total particles) mixed in ethanol. The powders were agitated by submersing the dispersions contained in flasks in an ultrasonic bath and sonicating them for more than 5 minutes. This was done in an attempt to break up any soft agglomerates and get more consistent particle size measurements (this method may not be aggressive enough and the use of an ultrasonic probe would be preferred, but access to such equipment is not currently available at our lab). Because the powders were dispersed in ethanol (non-protic liquid), the ultrasonic attenuation modality was the only working method to access the particles size. The BET specific surface area and porosity

of the Al_2O_3 powder was analyzed utilizing an ASAP 2020 Plus (Micromeritics, USA). Additionally, a batch of precursor powders were mixed and ball milled using our standard parameters. SEM and EDS were utilized to assess the quality of attrition and mixing achieved, as well as the degree of agglomeration after calcination.

3.2.4.2 Results

Scanning electron microscope (SEM) images of the selected precursor powders are shown in Figure 27. Figure 27(a) and (b) show the yttria powder. The particles are angular and have many cracks. The particles that appear to be one solid particle may actually be agglomerates of smaller particles. The particles/agglomerates are between 2 and 10 μm .

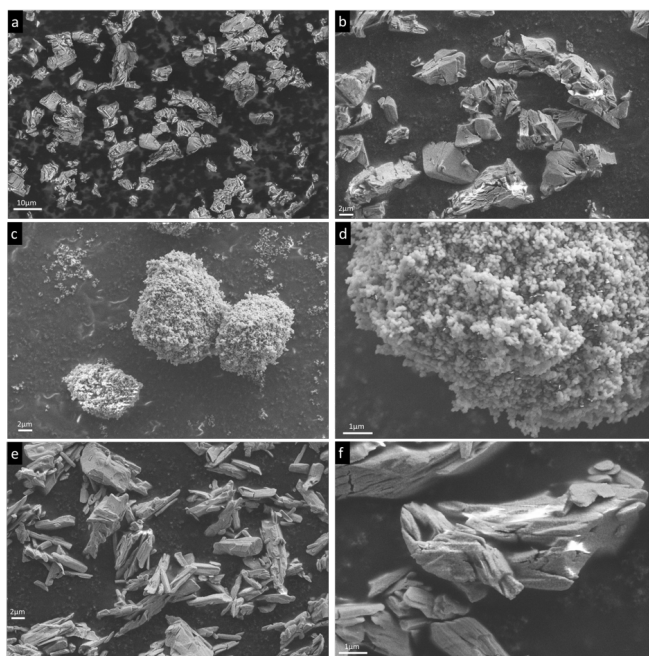


Figure 27: SEM images of precursor powders. Yttria at 1000x (a) and 2500x (b) magnifications, alumina at 2500x (c) and 10,000x (d) magnifications, and thulium oxide at 2500x (e) and 10,000x (f) magnifications, respectively.

Figure 27 (c) and (d) show the alumina powders. This powder is composed mostly of large, roughly spherical agglomerates of up to 10 μm . These agglomerates are composed of spherical nanoparticles that can clearly be seen in Figure 27 (d). The primary nanoparticles appear to be roughly 200 nm in size. This is in good agreement with the range of 100-300 nm provided by the manufacturer. There are a few unagglomerated alumina particles, which can be seen around the agglomerates in Figure 27(c). Figure 27(e) and (f) show the thulium oxide particles. These particles are rod-shaped and roughly 1 to 4 μm wide and 2 to 10 μm long. Figure 28 shows the

average particle size distribution of the yttria particles as determined using the ultrasonic attenuation method. The average particle size was calculated to be 3.72 μm , while the d_{15} (15% of particles smaller than or equal to this number) was 0.83 μm and the d_{85} (85% of particles smaller than or equal to this number) was 16.62 μm . A lognormal distribution is assumed to obtain this calculated distribution from the ultrasonic attenuation data. This distribution seems reasonable when compared with the SEM images of the yttria particles; however, the average particle size reported by the manufacturer is slightly larger at 5.47 μm . This discrepancy could be caused by various factors, particularly the degree of agglomeration of the particles, which is heavily influenced by the dispersing medium, pH, ionic strength, polarity of the solvent, and agitation to break up the particles in the solution.

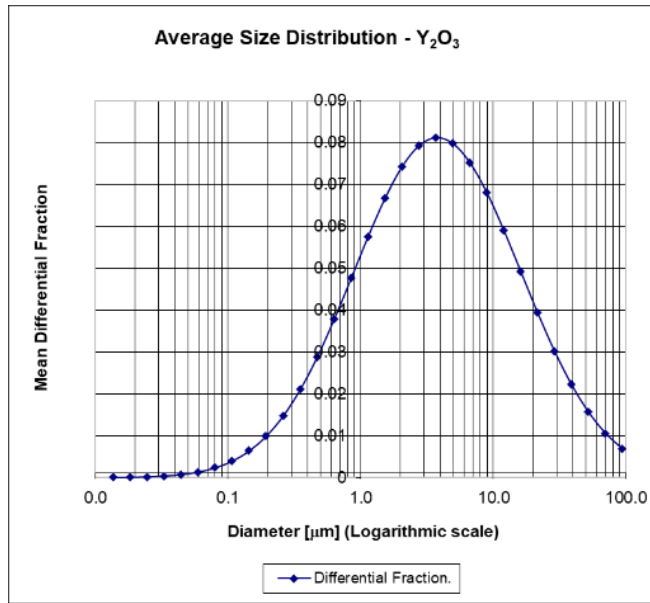
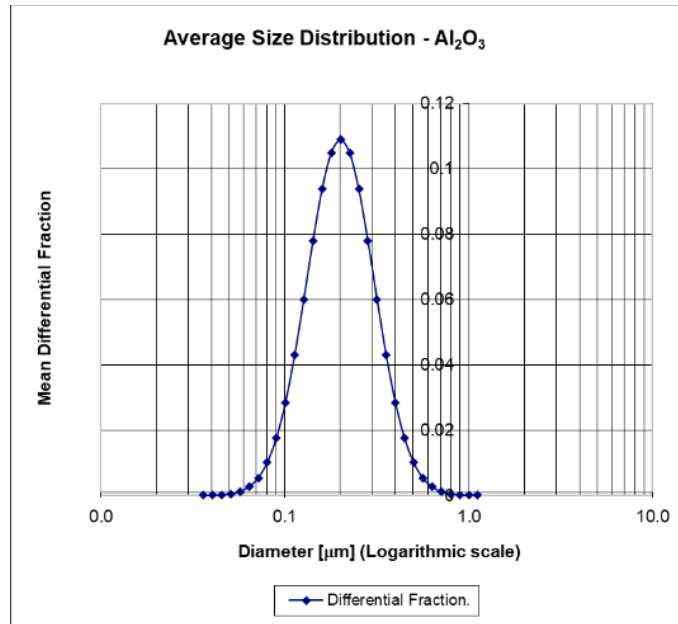


Figure 28: Average size distribution of yttria particles. Average particle size = 3.72 μm .

Figure 29 shows the average particle size distribution of the alumina particles as determined using the ultrasonic attenuation method. The average particle size was calculated to be 0.20 μm , while the d_{15} was 0.130 μm and the d_{85} was 0.310 μm . Again, a lognormal distribution is assumed.



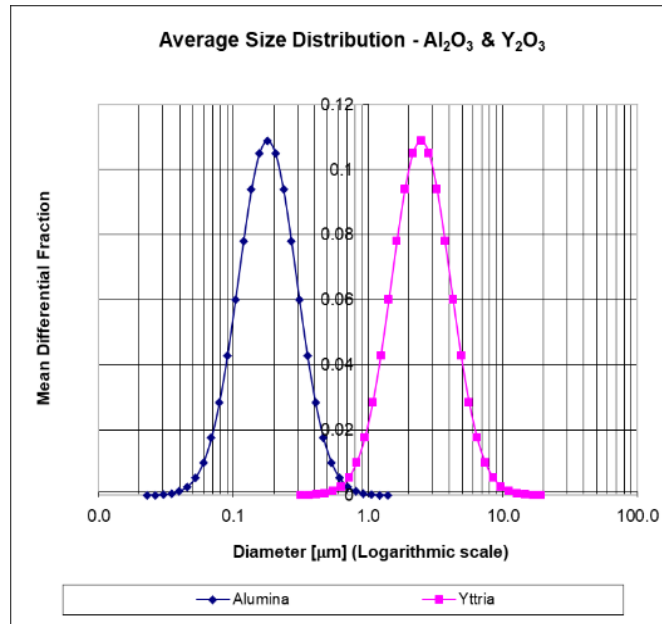


Figure 30: Average size distribution of 50-50 wt% mixture of alumina and yttria particles. Average particle size alumina = 0.180 μm . Average particle size yttria = 2.47 μm .

The precursor powders for the synthesis of YAG have been characterized by SEM and ultrasonic attenuation method for particle size analysis. The alumina, yttria, and thulium oxide powders were found to have very different morphologies and particle sizes.

Towards the end of this project, we acquired a Micromeritics ASAP 2020 Plus instrument for further characterize of our powders and powder compacts. This instrument provides the capability to quantify the BET specific surface area and porosity of precursor powders, adding to the current characterization capabilities of our ceramics processing lab. A protocol for the cleaning of glassware and prepping of samples was developed. This protocol and measurement of a sample powder was repeated multiple times to test the accuracy and repeatability of the instrument. The calibration tests were conducted on an alumina-silica calibrated standard provided by the manufacturer. All measurements conducted were within 1.5% of the mean values provided for the standard and well within the acceptable range. ***This provides confidence that the developed protocol will provide valid results.***

Below are the results from the first measurements on Al_2O_3 powders(Taimei Chemicals Co.)

Table 2: Results of BET analysis of Al₂O₃ powder on the Micromeritics ASAP 2020 Plus.

Test	Multi Point Specific Surface Area (m ² /g)	Total Pore Volume at Po 0.990 to 0.980 (cm ³ /g)	Average Pore Diameter (Å)	Single Point Specific Surface Area (m ² /g)
Measurement 1	12.3779	0.1081	341.54	12.1549
Measurement 2	12.4096	0.1193	374.48	12.1864
Measurement 3	12.3965	0.1232	386.88	12.1738
Average	12.3947	0.1169	367.63	12.1717

The average specific surface area validates the value provided by the vendor for this lot of powder providing further confidence in the developed protocol. Due to the project ending, we were unable carry out this characterization on the rest of our precursor powders.

The following section shows how effective the milling process is at attriting and mixing a mixture of Al₂O₃, Y₂O₃, and Yb₂O₃ used in the preparation of Yb-doped YAG. The aluminum and yttria powders are the same as discussed previously in this section. The ytterbium oxide particles (Figure 31: S) are angular, with a similar morphology to the yttrium, with the size ranging from 2 to 10 microns.

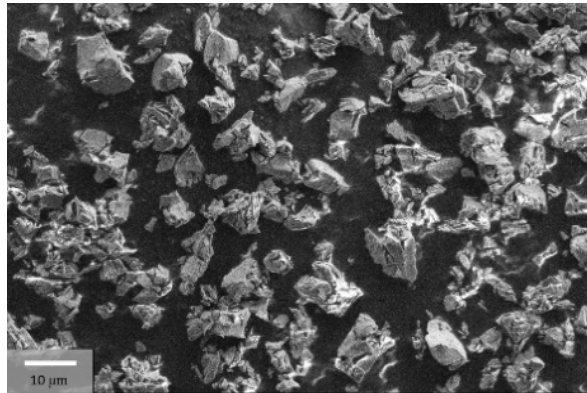


Figure 31: SEM micrographs of raw unmixed precursor powder Yb₂O₃ at 1000x.

a shows these precursor powders after balling milling in ethanol for 20 hours at 250 rpm after sieving. Followed by b and c, showing the powder mixture after further processing and calcination at 800°C for 2 hours.

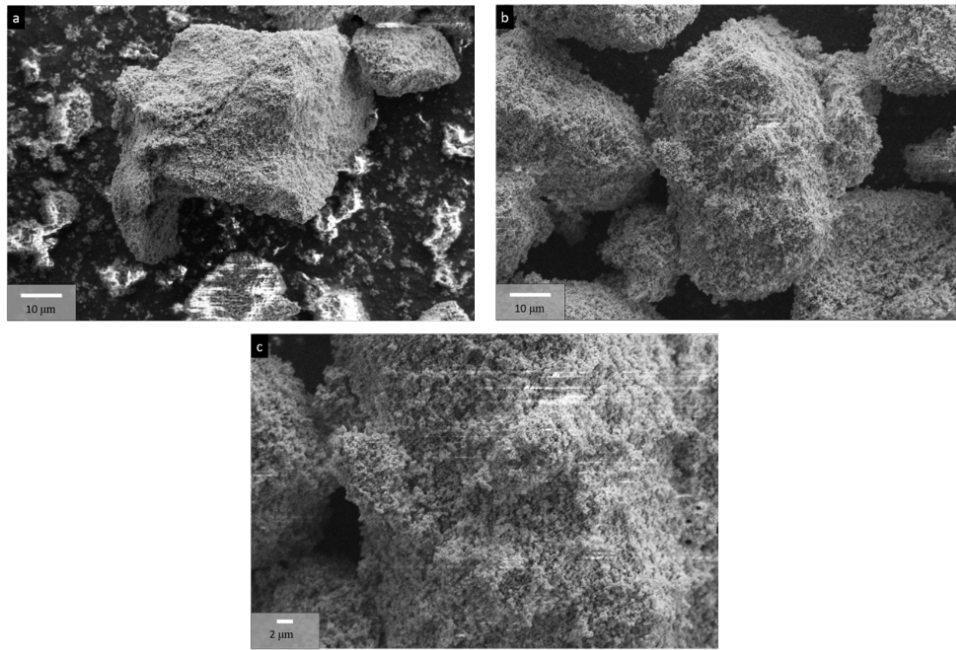


Figure 32: a) SEM micrographs of mixed Al_2O_3 , Y_2O_3 , and Yb_2O_3 precursor oxides after ball-milling and sieving at 1000x, (b) and after calcination at 800°C prior to forming at 1000x, (c) after calcination at 800°C prior to forming at 2000x.

Micrograph in Figure 32a shows that the precursor powders have been pulverized and deagglomerated, which is necessary to achieve intimate mixing. We used Energy-Dispersive X-ray Spectroscopy (EDS) at a scale commensurate with the soft agglomerates seen in the micrographs above to measure the degree of mixing of these oxides. The sampling in Figure 33 is between $150\text{-}1200\ \mu\text{m}^2$ and shows the magnitude of the alumina to rare earth peak height ratio is between 1.8-2.0 which is expected for this composition confirming that the milling process conditions are sufficient to also obtain intimate mixing.

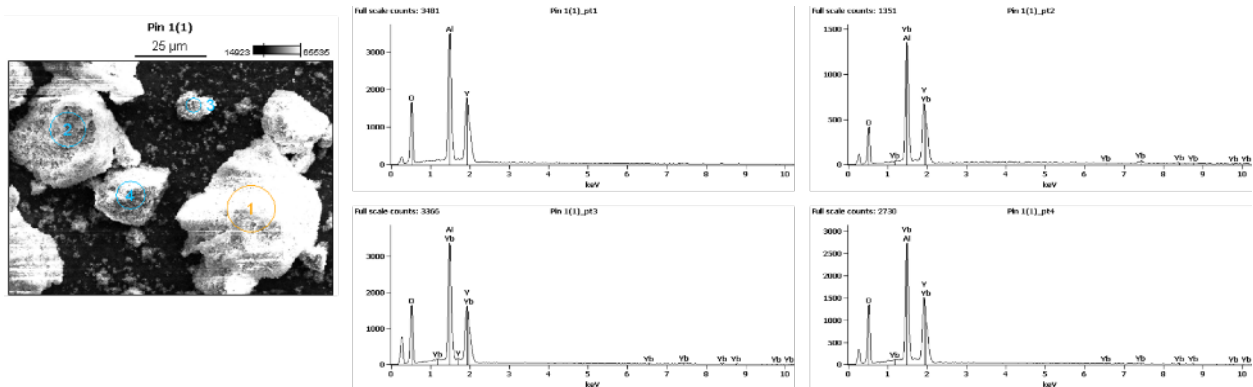


Figure 33: Energy dispersive X-ray Spectroscopy (EDX) spectra of several soft agglomerates of a mixture of precursor oxides after ball milling showing that the magnitude of the alumina to rare earth peak height ratio is 1.8-2.0, which is expected for this composition of Yb:YAG. Therefore, confirming that the precursors are intimately mixed.

Coupling this analysis with the quality of our samples, this shows the present ball milling conditions provide sufficient attrition, de-agglomeration, and mixing to produce high quality transparent ceramics via the reactive sintering route.

Further investigation could entail removing a small amount of material from the batch during ball-milling at various times to determine when sufficient mixing, de-agglomeration, and particle-size reduction has occurred. This would allow the reduction of the ball-milling time to the minimum necessary time, while reducing the potential for contamination from the grinding media. The effect of other ball-milling parameters on the particles could also be investigated to highlight possible effects that the particle size, morphology of precursors, and ball-milled powders have on the final ceramic quality. Additionally, the particle size distribution could be analyzed after ball-milling as a function of time using the ultrasonic attenuation method to help quantify the appreciable reduction in the particle size or de-agglomeration to determine the optimum ball-milling time to get sufficient mixing, de-agglomeration, and particle size reduction while minimizing the contamination from milling media.

3.2.5 *Optical and preliminary laser characterization of sintered samples*

Optical characterization, by way of an of in-line transmittance measurement, is typically conducted on sintered, polished ceramics on a UV-Vis-NIR spectrophotometer (Varian, Cary-500). Before collection of the in-line transmittance spectrum of the sample (T_{sample}), two spectra are collected for correction of the sample spectrum due to instrumental artifacts. The first correction spectrum is that of 100% transmittance (T_{100}) and is collected with a blank plate in the collection chamber. The second correction spectrum is that of zero transmission (T_0) and is acquired by blocking the pinhole of the sample holder. The equation used to make the above-mentioned correction is:

$$T_{correct} = \left(\frac{T_{sample} - T_0}{T_{100} - T_0} \right) \times 100 \quad (16)$$

As an example, Figure 34 shows the transmission spectrum of a 4.1 at% Tm³⁺:YAG transparent ceramic sample 4 mm-thick.

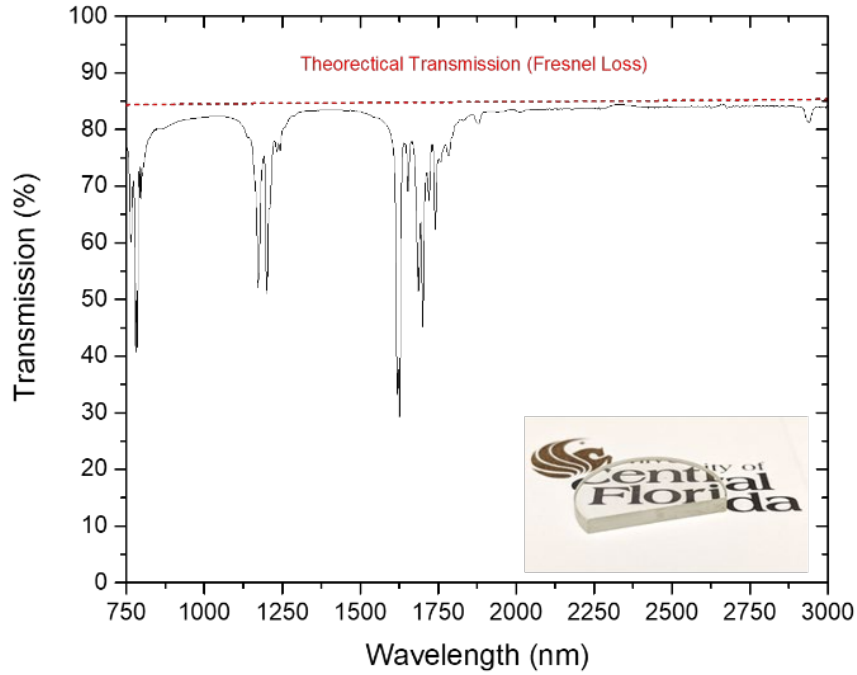


Figure 34: In-line transmittance of a 4.1 at% Tm:YAG ceramic sample.

The various insights we have gained on the control of our transparent ceramic fabrication process resulted in a drastic improvement in sample quality. This quality improvement is best judged by the ability to reach laser threshold and achieve a decent laser efficiency. Despite not being the focus of this research program, we nonetheless proceeded to evaluate the lasing performance of some of our 6 at.% Tm:YAG TOC samples (Figure 35), with the grateful help of Prof. Ivan Divlianski and Lam Mach at the *Photoinduced Processing Laboratory*, CREOL.

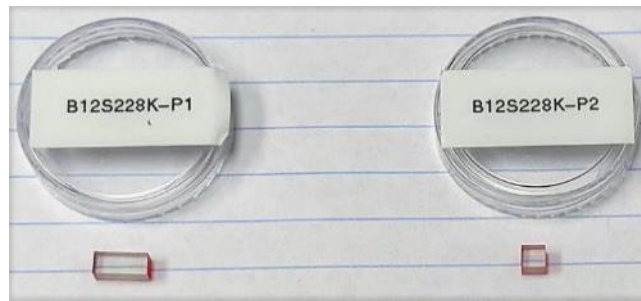


Figure 35: Polished 6 at% Tm:YAG ceramic samples extracted from a 1" TOC disc. Samples are 6x3x3 and 3x3x3 mm in size, respectively.

Due to lack of time to prepare the sample before insertion into the cavity, the 6 at.% Tm:YAG TOC sample, 3x3x3 mm in size, with two opposite faces mirror-polished was not antireflection-coated for these laser tests. The sample was end-pumped by a laser diode (LD) with an emission wavelength of 794 nm at room temperature and blue-shifted to the $^3H_6 \rightarrow ^3H_4$ absorption band of Tm:YAG at 786 nm by a thermoelectric cooling stage. The 12-cm long folded laser cavity consisted of a dichroic mirror (DM, AR-coated at 792 nm and HR-coated at 2015 nm), a fully reflective curved mirror (CM) and an output coupler (OC) with 15% transmission at 2015 nm (Figure 36). Two aspherical lenses were used to collimate the diode output and re-focus it into the crystal down to a 200 μm spot size (Figure 37). Figure 38: shows the laser performance obtained in this configuration. A maximum laser output power of 0.5 W at 2 μm was obtained for 7 W of absorbed pump power, with a laser threshold of 2.27 W and an optical-to-optical slope efficiency of 11%. The low value of the slope efficiency mostly originates from the fact that the output coupler is 85% transmissive and that the ceramic was not AR-coated, nor placed at Brewster angle in the cavity. However, these results speak to the improving quality of our transparent ceramic process.

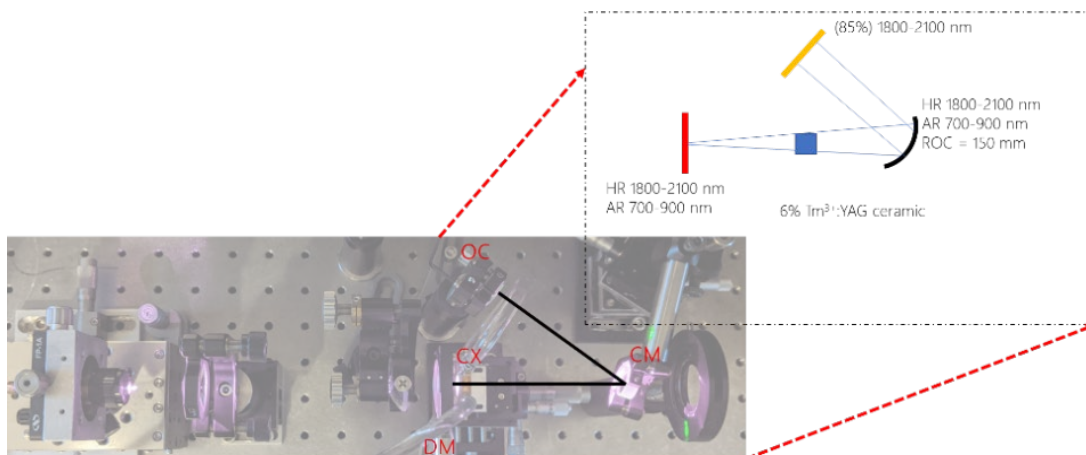


Figure 36. V-fold laser cavity used to test Tm:YAG ceramics made at UCF.

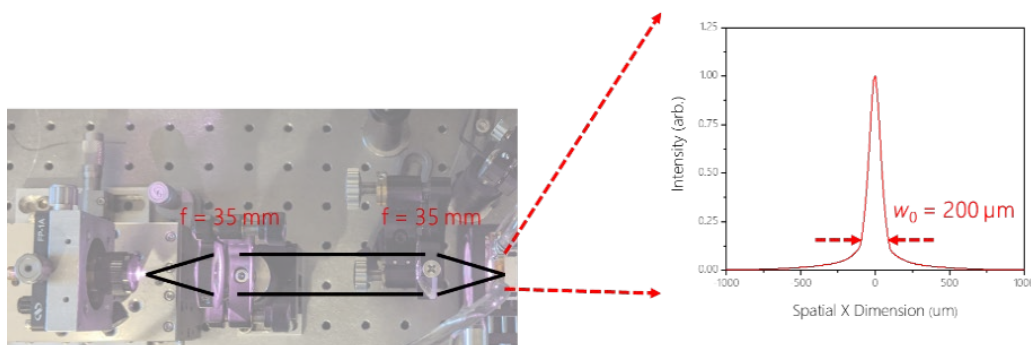


Figure 37. Collimating telescope focusing the laser diode onto the Tm:YAG sample. The Rayleigh width is 200 μm in diameter.

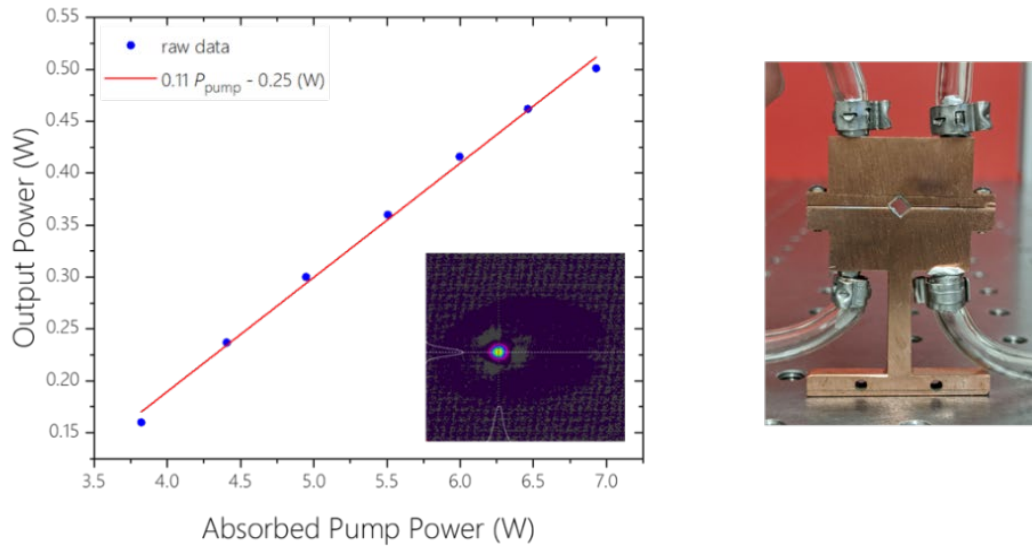


Figure 38: Laser performance test on a 6 at.% Tm:YAG transparent ceramic made at UCF (see text for details). The output is in the TEM00 mode (inset).

3.2.5.1 Fabrication of Yb:YAG for novel laser architectures

We started the fabrication of Yb:YAG ceramics for this program and to investigate novel laser architectures with the help of Prof. Divliansky at CREOL, UCF. Some of these architectures take advantage of large aperture gain media and, for this reason, require laser ceramic materials. Producing this part will allow us to prove the consistency in which we can achieve transparent laser grade ceramics, characterize the reproducibility of our process and the quality of the resulting samples. Additionally, some of these parts can be included in a set of parts used to investigate the use of LIBS on rear-earth doped YAG ceramics to determine deviation from stoichiometry.

Yb:YAG is susceptible to concentration quenching at high doping concentrations, predominately due to the other impurities that remain after purification of Yb_2O_3 (Er^{3+} , Ho^{3+}) [44, 45]. The presence of these impurities in the ceramic causes a decrease in the lasing efficiency and higher thermal loading. Dong, *et al.*, observed this effect in Yb:YAG ceramics when the Yb doping concentration is above 12% [46]. With this consideration, we chose a doping concentration of 10 at% Yb which will allow us to achieve an absorption of $\sim 96.5\%$ at 970 nm in a part with a thickness of 1.5 mm, after the double pass required by the cavity design. The thin disk, with its large surface area, in contact with the active cooling block will also work to mitigate thermal quenching and lensing effects.

To start with the highest purity RE dopant possible ytterbium oxide (4N8) was purchased from a vendor. Following the fabrication process that we have worked to optimize throughout this program, the precursor powders Y_2O_3 (Alfa Aesar, 99.99%), Al_2O_3 (Taimai Chemicals Co., LTD., 99.99%), and Yb_2O_3 (Alfa Aesar, 99.998%) were mixed, ball milled, calcined, sieved and pressed. The aim is to achieve a part where the whole diameter will be pore free and laser grade, but a 10-12.5 mm usable diameter will be sufficient for this application.

After sintering, the part was treated in the hot isostatic pressed (HIP) at 1700°C and 200 MPa for 5 hours in argon atmosphere to reduce any residual porosity.

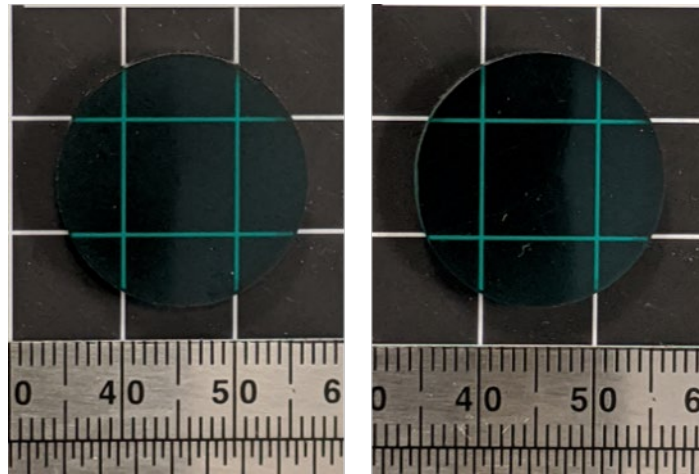


Figure 39: 10at% Yb:YAG after sintering and polishing, 25.4 mm.

The dark green color of the ceramic is indicative of the reduction of $Yb^{3+} \rightarrow Yb^{2+}$ during reactive sintering under vacuum, leaving behind Re-F color centers and oxygen vacancies [47-50]. These defects reduce the transparency of the sample by causing absorption peaks at 380 nm and 640 nm [51], while also decreasing the fluorescence intensity and lifetime [49, 52]. Annealing of the part will eliminate these defects that are deleterious to lasing performance. A literature survey was conducted in an attempt to determine the nominal annealing parameters. Discounting those references that were working with single crystals, Wu and Luo annealed in air at temperatures between 1400-1450°C for between 20 and 35 hours [51, 53]. While Tang annealed in oxygen at 1450°C for 10 hours for all experiments [49, 52, 54]. However, the thickness and geometry of the sample is important as this is a diffusion-controlled process and therefore diffusion length is important. The authors do not state what the thickness of the part is during annealing. Therefore, with a lack of concrete annealing conditions and our intent to employ a conservative annealing temperature, we chose to anneal at 1250°C but extend the soak time to 100 hours in air.

These parts are awaiting post processing, characterization and testing.

The control over our process is attested by the consistent quality of the parts produced and the ability to employ them in the intended application. We have now been approached about collaborations to make transparent ceramics for novel laser applications and intend to pursue these opportunities.

3.2.6 Other accomplishments

3.2.6.1 Cold isostatic press

In the first funding year, and as budgeted in our proposal, we ordered a custom-made hardened steel vessel from Fluitron Inc. to fix our cold-isostatic press (CIP). The new vessel is rated for 66 kpsi (455 MPa) and has a 4-inch internal diameter that will allow for the processing of larger sample sizes. We designed a support structure to fix this vessel to our current pump and control cabinet. A rendering of the CIP system and the vessel support structure, separately, are shown in Figure 40.

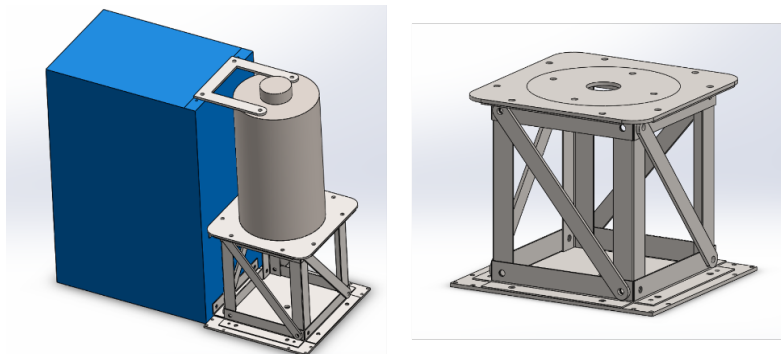


Figure 40: (left) CIP vessel with support structure attached to pump cabinet; (right) CIP vessel support structure.

The vessel will weigh approximately 800 lbs and thus requires a robust support structure. The support structure must be fixed to the cabinet as rigid high-pressure lines will connect the vessel to the pump within the cabinet. The chamber of the vessel will be sealed by a large threaded cap and a significant amount of torque will be imparted to the structure during closure. Hence, diagonal cross members were added to the structure to allow this moment to be more easily transferred to the base. Mild sheet steel was chosen for building the support structure as it allowed for cutting of the necessary geometries by waterjet. Stress simulations were run to determine the required thickness of steel needed to achieve a sufficient factor of safety. An image of the stress simulation for construction from ½” steel plate is depicted in Figure 41 (left).

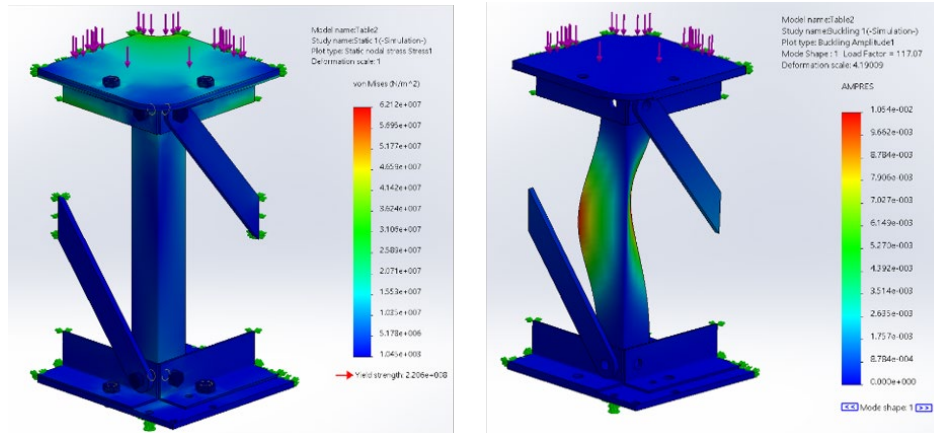


Figure 41: Stress (left) and buckling (right) simulations of CIP support structure, with ½” steel plate

The support structure has a 4-fold symmetry about the center of the top plate, where the vessel will be mounted. This allows a simplification of the simulation, where 250 lbs was applied to a single quadrant. As expected, there is a stress concentration near the sharp corners at the circular knockout in the top plate. The stress magnitude at this location is 62 MPa, which is still well below the yield strength of the material (221 MPa). The highest stress outside of this location is approximately 36 MPa. Through these simulations it was determined that using 3/8” sheet steel would only provide a factor of safety of 2, while using ½” sheet would provide a factor of safety of 7. Therefore, we felt more comfortable constructing the structure from ½” sheet. Additionally, a buckling simulation was conducted as slender L-shaped beams, with fixed end conditions, are used to transfer the load to the base. The result of this simulation is shown in Figure 41(right). Here it should be noted that the deformation scale is exaggerated as the maximum deformation is on the order of a thousandth of an inch. Additionally, with a load factor of 117, this structure will not fail in buckling unless a load of 29 kips is applied.

These simulations provide confidence in the design of the supporting structure, and it was assembled per these designs. The functionality of the current pump and high-pressure system was confirmed prior to receiving the vessel.

Upon receipt, the stainless-steel vessel was coated with a high-quality clear coat to prevent damage from oxidation. Custom bent high-pressure pipes and new valves were ordered that allowed the existing control cabinet to be retrofit to the new vessel. The support structure was fixed to the right side of the control cabinet, then the vessel was then sat down on the platform and bolted in place. The pipes and valves were installed along with a transparent “sight” that allows the user to see when all air has been vented from the vessel prior to loading with pressure. The system is rated up to 455 MPa and was tested up to 350 MPa, at which time no leaks were found, and the pump was performing well with plenty of power to increase the pressure further. Pictured below is the cold isostatic press (CIP) system under operation.



Figure 42: CIP cabinet with newly manufactured and installed vessel under operation at 200 MPa.

Through the fall of 2020, this equipment had performed well until the pump the hydraulic failed. Upon disassembly, it was discovered that one of the seals in the hydraulic cylinder had deteriorated. The pump was completely torn down, all new seals installed, rebuilt and is now in working order. An inline air lubrication system was also installed at this time.

3.3 Conclusion

The accurate and precise weighing of oxide powders is critical to ensure the proper garnet phase stoichiometry and repeatable product quality. Any deviation from this ratio impart defects to the ceramic that affect the rate of densification, the microstructure, and the optical performance.

We have developed a simulation tool to model the statistical contribution of the various experimental uncertainties on the fabrication process. This tool has helped us prioritize our efforts to reduce those uncertainties that bear the largest impact on the repeatability of the product quality.

We have developed protocols for the quantification of the loss-on-ignition of our starting powders and for the weighing errors that provides useful and quantitative results. The uncertainty attributed to the LOI of precursor powders and the alumina deposit far outweigh the contribution from weighting of precursor powders, which serves as the limit to which the uncertainty can be reduced. Regarding the issue of the alumina deposit coming from the ball-milling process, we have found that the current means to quantify this is not only complex and time consuming, but very imprecise. We have proposed an approach to a solution that would provide a quantitative assessment of this contribution. The protocol we refined for the measurement of loss-on-ignition of precursor powders has successfully reduced the uncertainty related to this measurement compared to that as stated in literature. The novel anti-walk device we have designed, and filed a patent for, will further reduce these uncertainties. Coupling these advances together will not only allow a guarantee of achieving parts within the solid solution but also the targeting of specific compositions within this regime, and a more repeatable fabrication process.

Our attempt at using a contamination-free mixing process achieved relative densities higher than 90% after sintering, with the highest being 98%. We were unable to achieve phase purity in the samples, even after an attempt to optimize the sintering schedule to account for the possibility of larger particle sizes. However, when plotting relative density vs milling time there is a positive correlation indicating that increased rotation speed and milling time induce improved densification. The part with the highest density after sintering actually became transparent after post processing. With further analysis and experimentation, it might be possible to extrapolate a milling time that would produce a high density and phase pure transparent ceramic.

Over the past three years, the various insights we have gained on the control of our transparent ceramic fabrication process have seen a drastic improvement in sample quality. The consistency of sample quality originating from different batches and the recent laser test on a 6 at.% Tm:YAG TOC sample confirm our better understanding of the synthesis of oxide garnets, and our stronger hold on their fabrication process.

4. Laser-Induced Breakdown Spectroscopy (LIBS): A novel method for the assessment of stoichiometry in optical ceramics.

4.1 Objectives

To solve the stoichiometry problem in YAG, we have proposed the use of Laser-Induced Breakdown Spectroscopy (LIBS) as an inexpensive technique capable of multi-element analysis, requiring minimal sample preparation and that could be performed on powders, green-bodies or sintered ceramics. Today, techniques for the *analysis of non-stoichiometry in insulating materials*, such as x-ray fluorescence, x-ray diffraction, ICP-AES, PIXE, are limited in their accuracy (around 2%) and can be cumbersome to use. It is worth emphasizing that, contrary to most techniques developed for the quantification of dopant or trace elements down to ppb levels, our aim is to determine the ratio of major elements, such as aluminum and yttrium, in the most accurate and sensitive manner.

The principle of the LIBS technique consists of ablating a sample with a high-energy laser pulse and deducing its chemical composition from the emission of the plasma that results from the interaction (Figure 43).³

³ The intensities of the plasma emission lines are directly related to the concentration of species according to the Saha-Eggert equation.

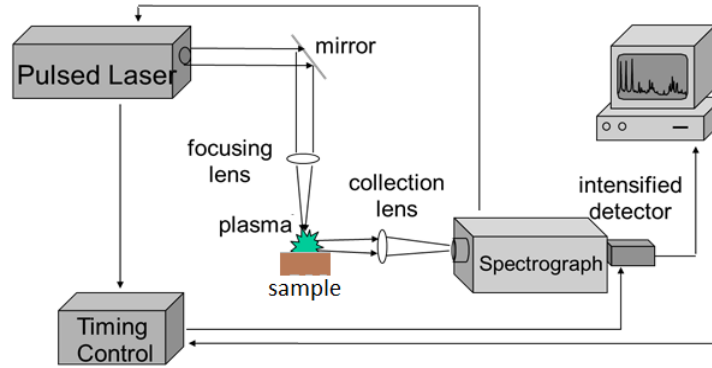


Figure 43: Schematic of a LIBS setup.

Prior to this funding, we had been able to confirm that this technique is sensitive enough to detect small departure from stoichiometry (0.1 mole% in the case of YAG) in the case of fully sintered ceramics (Figure 44). However, the current developments of LIBS present two major limitations:

- A limited precision: LIBS's precision for quantitative measurements is about a few percent typically. The technique is sensitive to fluctuations in experimental conditions (i.e. laser fluence) and therefore the repeatability of experiments cannot be achieved unless great care is put in the reduction of any parameter fluctuations.
- Matrix effects: the physical and chemical properties of the target greatly affect the characteristics of the laser ablation and, as a consequence, the plasma emission spectrum.

Our goal is to improve on the current capabilities of LIBS to enable its use at every step of a ceramic fabrication process, whether on free-flowing powders, powder compacts or sintered parts, and ultimately enable the fabrication of composition-controlled optical ceramics.

Generally, quantitative elemental analysis by LIBS is calibration-based. For measuring trace and minor amount of impurity in a sample (for instance SiO_2 in YAG, as will be discussed in Section 5 of this report), standard samples with a fixed matrix are spiked with different concentrations of the analyte. LIBS experiments are performed with the same experimental conditions on all samples and the detector response is plotted against the concentration of the analyte. However, if the composition of matrix itself needs to be determined, such as in the form of the Al/Y molar ratio in YAG ceramics, samples with slightly varying Al/Y molar ratio are prepared and the Al/Y intensity ratio is plotted against the molar ratio.

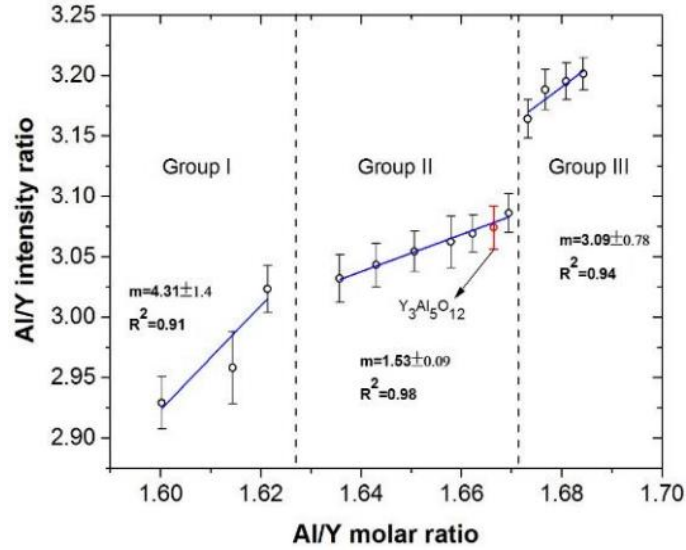


Figure 44: Variation of the aluminum to yttrium intensity ratio measured by LIBS with sample composition in fully sintered ceramics. The arrow points to the sample with the stoichiometric garnet phase composition (YAG). The three domains (labeled Group I, II and III) correspond to the visible appearance of the sintered samples: transparent for group II and translucent for groups I and III. The changes in slope seen in the calibration curves between these groups reflect differences in laser-sample interaction. After [55].

If the calibration curve is linear, the slope of the curve is called the sensitivity. However, if the curve is not linear, yet still a monotonically increasing function, the sensitivity is defined as the slope of the tangent at the middle of the working range. The unknown molar ratio or the concentration of the analyte is determined by putting the value of the detector response in the calibration curve equation. In the case of trace analysis, the detection limit of the instrument is defined as:

$$LOD = \frac{3\sigma}{m} \quad (17)$$

where σ is the standard deviation of the detector response for a blank sample, and m the sensitivity. The limit of quantification, i.e. the minimum concentration of the analyte that can be quantified, is:

$$LOQ = \frac{10\sigma}{m} \quad (18)$$

As stated above, a calibration curve is needed to find the stoichiometry shift in YAG samples. To this end, the intensity ratio of aluminum and yttrium lines are plotted against their molar ratio as shown in Figure 45.

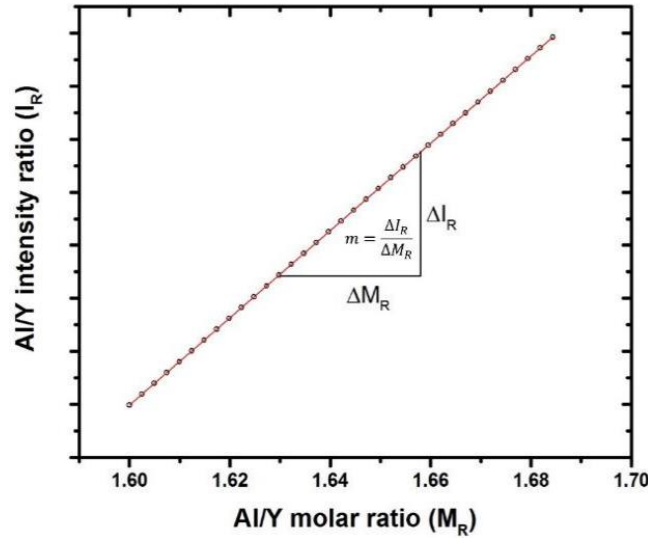


Figure 45: Hypothetical calibration curve to find the Al/Y molar ratio in YAG samples.

If the slope and intercept of the calibration curve are m and c , respectively, the molar ratio of a test sample is calculated according to:

$$M_R = \frac{I_R - c}{m} \quad (19)$$

Here M_R and I_R are the molar and intensity ratios, respectively. If the standard deviation for the intensity ratio is σ_{I_R} , the error in the corresponding molar ratio is:

$$\sigma_{M_R} = \frac{I_R - c}{m} \sqrt{\left[\frac{\sigma_{I_R - c}}{I_R - c}\right]^2 + \left[\frac{\sigma_m}{m}\right]^2} \quad (20)$$

Assuming that the relative errors in m and c are small compared to the relative error in I_R , Eq. 20 can be written as:

$$\sigma_{M_R} = \frac{\sigma_{I_R}}{m} \quad (21)$$

To differentiate the molar ratios between two adjacent compositions (x-axis of) with 99% confidence, we must have $3\sigma_{M_R} < \frac{1}{2}\Delta M_R$, where ΔM_R is the smallest difference in molar ratios between two adjacent samples. This implies that:

$$m > \frac{6\sigma_{I_R}}{\Delta M_R} \quad (22)$$

This expression shows that a large sensitivity for the calibration curve is essential to discern distinct molar ratios of non-stoichiometric YAG samples accurately. For instance, the difference in molar ratio of the samples at the extremities of the solid solubility limit is 0.03. The maximum standard deviation in intensity ratios that can be tolerated to differentiate such two samples must be:

$$\sigma_{I_R} = m \times 5 \times 10^{-3} \quad (23)$$

Since the ratio of the emission line intensities depends on the plasma temperature, it is crucial to optimize the experimental protocol to achieve the best sensitivity in the measurement.

4.2 Accomplishments

We have focused on: **(i) modeling the plasma conditions to ensure optimal sampling**, and **(ii) developing a working protocol to determine the Y/Al ratio in green-ceramics of Al_2O_3 - Y_2O_3 near the stoichiometric YAG composition**.

4.2.1 Simulation of YAG plasmas formed in air

Since the intensities of the emission lines at a given temperature depend on number densities of the emitters, the concentration of different atomic and molecular species as a function of temperature needs first to be computed. The plasma consists of ablated material vapor blended with the background gas. Let n_{vap} and n_{gas} be the atomic number densities of the ablated element (A), and the background gas (B) respectively. These elements exist as atoms and ions (A^0 , A^+ , A^{++} , A^{+++} , B^0 , B^+ , B^{++} , B^{+++}), homonuclear molecules (A_2 , B_2 , A_2^+ , B_2^+) and heteronuclear

molecules (AB, AB^+). At temperatures above 3000 K, formation of polyatomic molecules can be neglected [56, 57] so that:

$$\begin{aligned} n_{vap} &= n_A + \sum_{z=0}^1 n_{AB}^z \\ n_{gas} &= n_B + \sum_{z=0}^1 n_{AB}^z \end{aligned} \quad (24)$$

where n_A and n_B are the number densities of elements A and B (excluding molecules AB) and equal to:

$$n_X = \sum_{z=0}^3 n_X^z + \sum_{z=0}^1 n_{X_2}^z, X = A, B \quad (25)$$

Ionization states up to +3 are considered for atoms and +1 for molecules.

Assuming a plasma in local thermodynamic equilibrium (LTE), the number densities of ionic species can be obtained by Saha's equation (Eq. 27) combined with the conservation of mass. It should be noted, however, that the ionization energies are lowered in plasma due to the presence of a micro-field, which can be well approximated using Unsöld's formula [58]:

$$\Delta E_z^{ion} = 3e^2(z+1)^{3/2} \left(\frac{4\pi}{3} n_e \right)^{1/3} \quad (26)$$

The number density of neutral molecules is calculated using the law of mass action for the chemical equilibrium $A+B \rightarrow AB$ [59]:

$$\frac{n_A^0 n_B^0}{n_{AB}^0} = \left(\frac{2\pi k_B T}{h^2} \frac{m_A m_B}{m_{AB}} \right)^{3/2} \frac{U_A^0 U_B^0}{U_{AB}^0} e^{-\frac{E_D}{k_B T}} \quad (27)$$

Here, U_{AB}^0 is the partition function of a neutral molecule, E_D the molecular dissociation energy and m_A the mass of element A. The partition function of atomic species is given by:

$$U_A^z = \sum_j g_j e^{\frac{-E_j}{k_B T}} \quad (28)$$

with, g_j the degeneracy of energy level E_j . The atomic energy levels and their degeneracies can be found in the NIST atomic level database [60]. The molecular partition function is determined according to:

$$\sum_{e,\vartheta,J} (2 - \delta_\Lambda)(2S + 1)e^{-\beta E_e} \times e^{-\beta E_\vartheta^e} \times g_N e^{-\beta E_J^{e,\vartheta}} \quad (29)$$

where e , ϑ , and J are the electronic level, the vibrational and rotational quantum numbers, respectively with corresponding energies E . δ_Λ is the Λ -type doubling factor and g_N is the nuclear statistical weight. The vibrational and rotational energies are obtained by:

$$E_\vartheta^e = hcG^e(\vartheta), G^e(\vartheta) = \omega_e \left(\vartheta + \frac{1}{2}\right) - \omega_e x_e \left(\vartheta + \frac{1}{2}\right)^2 + \omega_e y_e \left(\vartheta + \frac{1}{2}\right)^3 \quad (30)$$

$$E_J^e = hcF_J^\vartheta(\vartheta), F_J^\vartheta(\vartheta) = B_\vartheta J(J + 1) - D_\vartheta J^2(J + 1)^2 \quad (31)$$

With $B_\vartheta = B_e - \alpha_e \left(\vartheta + \frac{1}{2}\right) + \gamma_e \left(\vartheta + \frac{1}{2}\right)^2$ and $D_\vartheta = D_e - \beta_e \left(\vartheta + \frac{1}{2}\right)$

The second and third order terms in (Eq. 30) and (Eq. 31) arise because of anharmonic oscillations and deformable bonds. Values of the constants $\omega_e, \omega_e x_e, \omega_e y_e, B_e, \alpha_e, \gamma_e, D_e$ and β_e can be found in NIST chemistry web book [61].

The composition of LIBS plasma at a particular temperature can then be calculated using the algorithm given in [62] and outlined in

Figure 47: V.

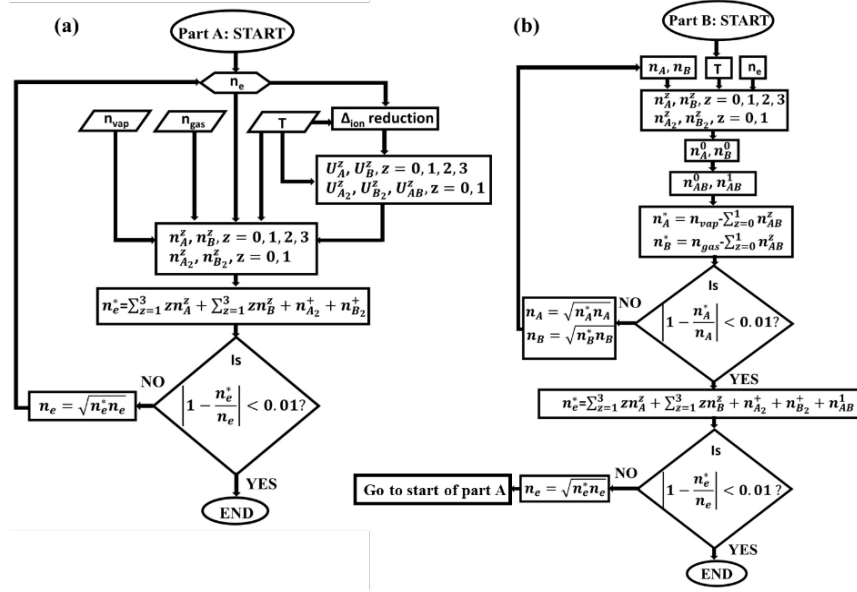


Figure 46: Algorithm flowchart for calculating number densities of different species in a plasma under local thermodynamic equilibrium. Iteration loop to calculate ionization equilibrium (a) and the chemical equilibrium (b).

The simulation is carried out using two iteration loops. The first loop is initialized with a certain electron number density n_e . Reduction in ionization potential is calculated based on Eq. 26 and then the partition functions are computed. Using these values, the number densities of neutral and charged atoms and homonuclear molecules are calculated. In the first part of the simulation, the material vapor and the background gas are not allowed to react so that $n_{vap} = n_A$ and $n_{gas} = n_B$. The electron density is given by:

$$n_e^* = \sum_{z=1}^3 z n_A^z + \sum_{z=1}^3 z n_B^z + n_{A_2}^+ + n_{B_2}^+ \quad (32)$$

If n_e^* and n_e differ by more than a percent, the value of n_e is updated as shown in

Figure 47: V(a) and the calculation is repeated. Once this loop converges, a second iteration loop is initiated in which neutral species of elements A and B are allowed to react to form neutral AB molecules. After computing the values of n_{AB}^0 and n_{AB}^+ , the total number density of unreacted A and B are updated using Eq. 33:

$$\begin{aligned} n_A^* &= n_{vap} - \sum_{z=0}^1 n_{AB}^z \\ n_B^* &= n_{gas} - \sum_{z=0}^1 n_{AB}^z \end{aligned} \quad (33)$$

Just as in the charge equilibrium loop, if n_A^* and n_A differ by more than a percent, the value of n_A is updated as shown in Figure 46(b) and the iteration is resumed. After convergence, the electron number density is recalculated with the addition of the electrons coming from AB^+ species:

$$n_e^* = \sum_{z=1}^3 zn_A^z + \sum_{z=1}^3 zn_B^z + n_{A_2}^+ + n_{B_2}^+ + n_{AB}^+ \quad (34)$$

Again, if the charge densities n_e^* and n_e differ by more than a percent, n_e is updated as before and the computation is resumed right from the beginning of the first loop, else the computation is stopped, and the number densities are returned.

The code for the simulation was written in MATLAB and tested against Hermann's results [62]. The first trial was to simulate an aluminum plasma in an oxygen background atmosphere. The starting values of n_{vap} , and n_{gas} were set just as in the reference, i.e. $1 \times 10^{22} \text{ m}^{-3}$ and $1.1 \times 10^{22} \text{ m}^{-3}$, respectively. The result in the temperature range 4000 to 12000 K is shown in Figure 47 and illustrates that our results (solid lines) are in excellent agreement with the results from the reference (circles). The results for aluminum plasma in nitrogen, also a replication of the simulation from the same reference, is shown in Figure 48, which further substantiates our procedure.

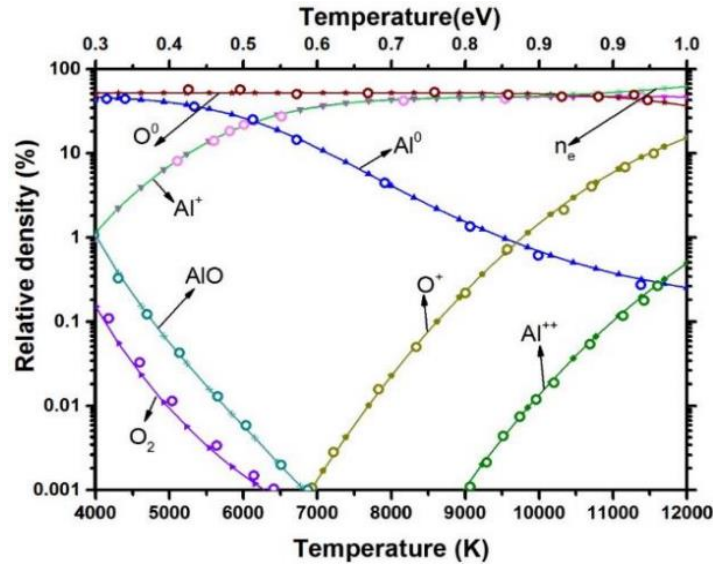


Figure 47: Validation of our plasma modeling code predicting the number densities of species for an aluminum plasma in oxygen as a function the plasma temperature. The circles are the simulation by Hermann *et al* [62] and the solid lines are our result. The number density of each species is normalized by the sum $n_{vap} + n_{gas}$.

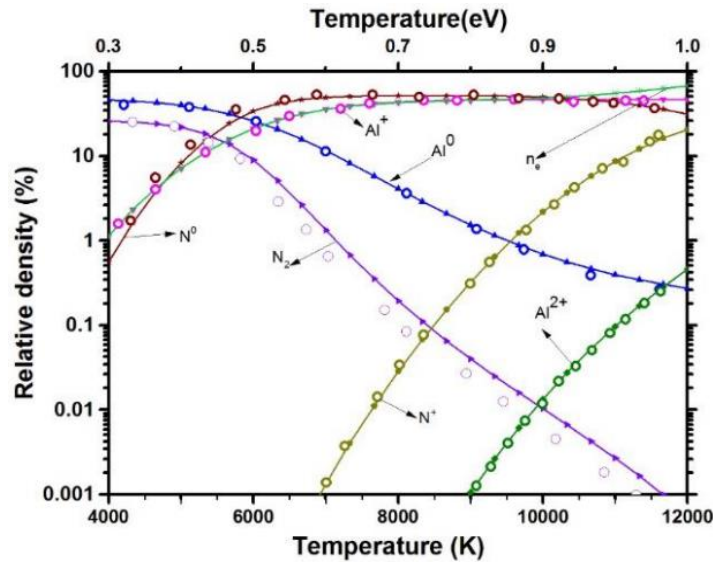


Figure 48: Validation of our plasma modeling code predicting the number densities of species for an aluminum plasma in nitrogen as a function the plasma temperature. The circles are the simulation by Hermann *et al* [62] and the solid lines are our result. The number density of each species is normalized by the sum $n_{vap} + n_{gas}$.

The slight discrepancy in the number densities of nitrogen molecules in Figure 47 and in

Figure 49: **S** may be due to the omission of Λ -type doubling factor and the nuclear statistical weight. Apart from this small difference, atomic number densities, which dictate the emission spectrum of LIBS plasma, are in very good agreement.

After the validation of the simulation code, we have used our algorithm to determine the composition of a YAG plasma in air. For this, we have used a number of ablated moles of YAG based on experimentally observed crater sizes. The diameter of the crater on the surface of YAG samples is typically 100 μm for dense samples. Assuming that all the ablated mass from the 100 μm diameter hemispheric crater goes into the plasma, a coarse assumption at the moment, the number density of YAG formula units ($\text{Y}_3\text{Al}_5\text{O}_{12}$) in the plasma should be of about $1.7 \times 10^{23} \text{ m}^{-3}$. This corresponds to $5 \times 1.7 \times 10^{23}$ aluminum atoms, $3 \times 1.7 \times 10^{23}$ yttrium atoms and $12 \times 1.7 \times 10^{23}$ oxygen atoms per cubic meter. Assuming a plasma diameter of 3 mm, the number density of oxygen and nitrogen atoms from the background atmosphere are $1.08 \times 10^{25} \text{ m}^{-3}$ and $3.8 \times 10^{25} \text{ m}^{-3}$, respectively (at 1 atm and a temperature of 300 K before the ignition of the plasma). An electron density of $1.5 \times 10^{23} \text{ m}^{-3}$ was used to initialize the simulation. The variation of number densities of the different species in the temperature range 5500 K to 18000 K is shown in Figure 49.

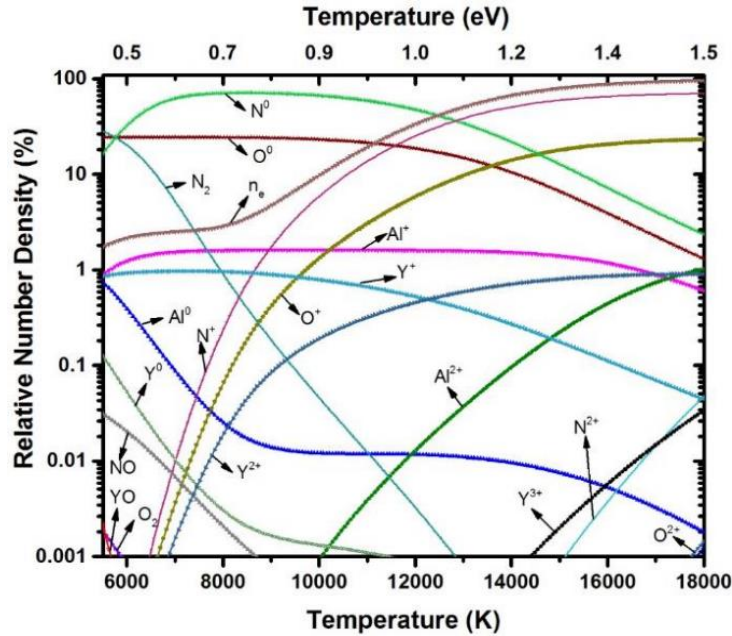


Figure 49: Simulation of a YAG plasma in air. The number density of ablated YAG molecules is estimated to be $1.71 \times 10^{23} \text{ m}^{-3}$ based on experimentally observed crater sizes. The air pressure was set to $1.01 \times 10^5 \text{ Pa}$ and the ratio of nitrogen to oxygen atoms was set to 3.7 to simulate the atmospheric conditions.

From Figure 49, it can be inferred that above 10000 K, the electron number density follows the trend of N^+ . The neutral atomic species Y^0 and Al^0 varies rapidly with temperature up to 8000 K. Al^0 levels off after this temperature while Y^0 becomes vanishingly small. On the contrary, the singly charged species Al^+ and Y^+ are relatively stable with temperature. ***This trend suggests that emission lines from Al^+ and Y^+ should be chosen for the analysis of the Al^+/Y^+ ratio in YAG ceramics, so that shot-to-shot fluctuations in plasma temperature have a minimal influence on the measured intensity ratio.*** The lines Al^+ 281.61 nm and Y^+ 278.52 nm were specifically chosen to monitor the behavior of the Al^+/Y^+ intensity ratio with plasma temperature (Figure 50), due to the close proximity of the upper energy levels.

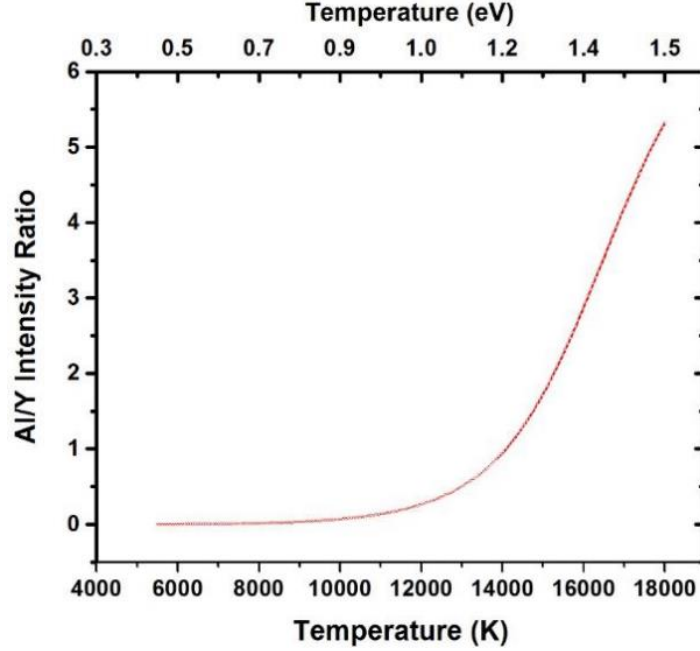


Figure 50: Simulated Al/Y intensity ratio as function of plasma temperature based on the atomic emission Al⁺ 281.61 nm and Y⁺ 278.52 nm peaks.

The intensities of the singly ionized aluminum and yttrium lines were calculated using Eq. 35:

$$I_{ji} = \frac{h}{4\pi} \nu_{ji} A_{ji} N_0^z \frac{g_j}{U^z(T)} e^{-\frac{E_j}{kT}} \quad (35)$$

where g_j is the degeneracy of the excited state j , U^z the partition function for a charge state z , N_0^z the total population of species with charge state z , T the temperature of the ensemble and k the Boltzmann constant. The constant A_{ji} is the atomic transition probability (unit s⁻¹), also known as the Einstein coefficient of spontaneous emission. The values A_{ji} , g_j and λ_{ji} were extracted from Kurucz database [63]. ***The Al⁺/Y⁺ ratio increases sharply after 12,000 K, which suggests that above that temperature, a small fluctuation in plasma temperature can produce large fluctuations in the measured intensity ratio.***

Finally, we have studied the behavior of the sensitivity of the measurement, m , with plasma temperature. To this end, simulations were performed at four different temperatures and, at each temperature, the molar ratio Al/Y of the ‘substrate’ was varied from 1.6 to 1.68 with a step size of 0.0025. These conditions are to correspond to the compositional range of ceramic we can typically produce near the nominal YAG stoichiometry. ***The results of these simulations (L) show that the sensitivity increases rapidly above 14,000 K.***

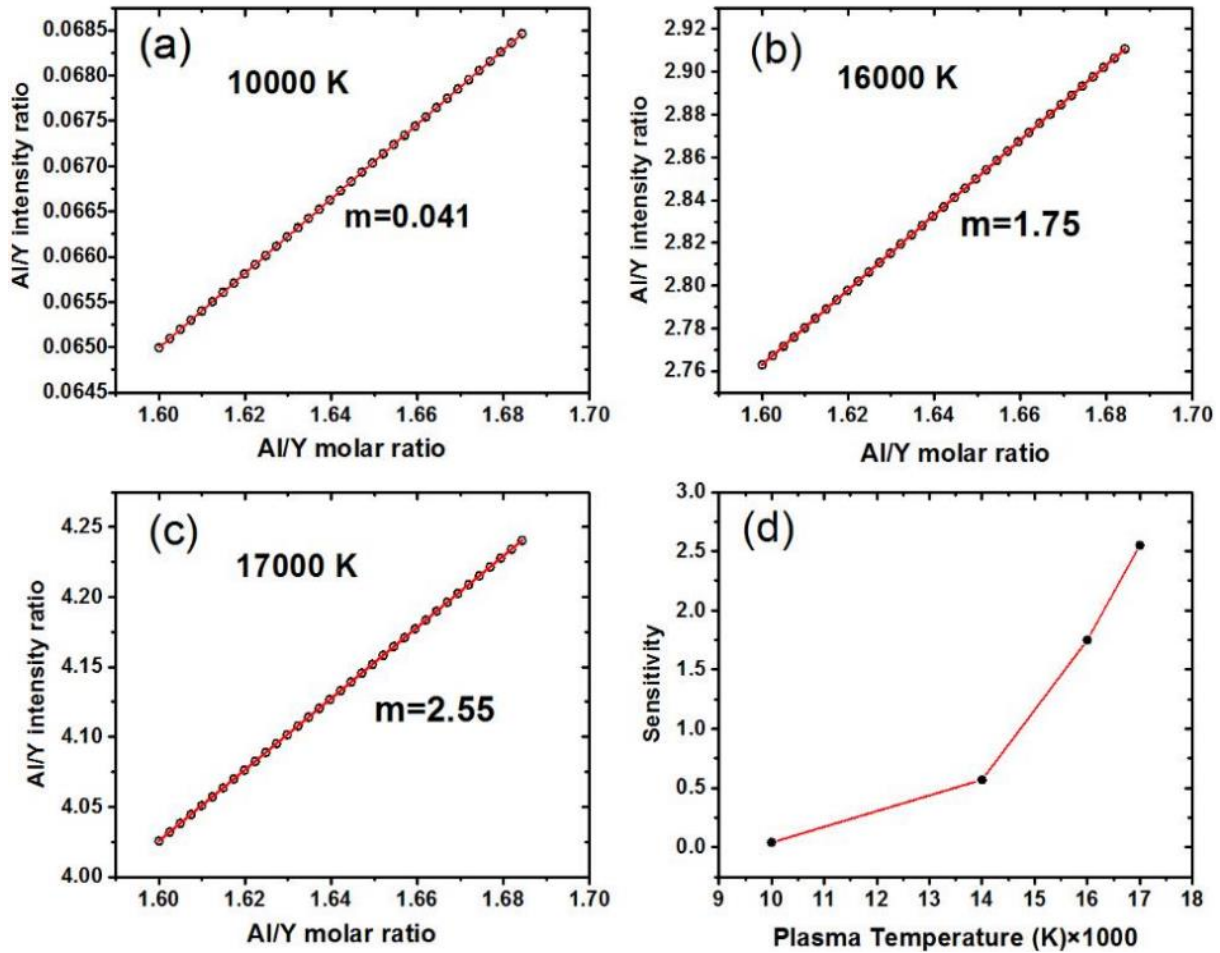


Figure 51: Simulated evolution of the sensitivity coefficient for the determination of the Al/Y ratio in YAG ceramics using the Al⁺ 281.61 nm and Y⁺ 278.52 nm atomic emission peaks.

In summary, our modeling results show that the Al⁺/Y⁺ intensity ratio, corresponding to atomic emissions at 281.61 nm for Al⁺ and 278.52 nm for Y⁺, varies sharply above 12,000 K implying that experiments should be carried out at plasma temperatures below this value to minimize shot-to-shot fluctuations on the intensity ratio. However, simulated calibration curves at different plasma temperatures show that the sensitivity increases from $m = 0.04$ to 2.6 when the temperature is increased from 10,000 K to 17,000 K. Given that the intensity ratios are too small to be experimentally resolved at lower temperatures, and that a sensitivity greater than $m = \frac{6\sigma_{IR}}{\Delta M_R}$ is required to differentiate molar ratios with 99% confidence, this modeling work suggests that plasma temperatures on the order of 14,000 K should provide sufficient sensitivity while maintaining the standard deviation of the intensity ratio smaller than $m \times \Delta M_R$.

4.2.2 Determination of the Al/Y molar ratio in unfired powder compacts of Al₂O₃-Y₂O₃

While the ability for LIBS to determine the departure from stoichiometry within 0.1 mol% in sintered YAG ceramics, this capability has not been demonstrated in unfired powder compacts. To investigate if LIBS can accomplish comparable resolution prior to full densification of the ceramics, a study was designed in which Al₂O₃ and Y₂O₃ precursor oxide powders were prepared with varying compositions about the stoichiometric ratio of the garnet phase. A 40 g mixture with an initial Al/Y molar ratio of 1.627 was ball-milled for 20 hours with ethanol and high purity corundum grinding medium. The resulting slurry was dried, sieved, and then calcined at 1000 °C for 4 hours. Aliquots of 3.35 g were separated from the larger batch and blended with controlled quantities of additional Al₂O₃ to produce eight samples of predetermined compositions. The samples prepared have Al/Y molar ratios ranging from 1.627 to 1.672. The ratio corresponding to stoichiometric YAG is 1.667, which lies within the range produced. The processed powder samples are uniaxially pressed at 10 MPa into 20 mm diameter pellets, followed by cold isostatic pressing at 200 MPa. The samples were then calcined in a furnace at 800 °C to remove the organic lubricant used during the uniaxial pressing process.

The LIBS experiments were carried out with a Q-switched Nd:YAG laser at the fourth harmonic (266 nm, 3.4 mJ, Quantel). Laser energy was optimized to produce a stable plasma and increase the signal-to noise ratio without saturating the acquired signal. The optics of this LIBS system have been outlined by Pandey *et al.* [55]. However, in this experiment the Czerny-Turner spectrometer utilized a 3600 1/mm grating and a Princeton (PMX4) intensified charge coupled device (ICCD) camera were employed to record the spectra. The laser pulse delay was set at 900 ns and the duration of acquisition by the ICCD camera was 1000 ns. For each sample, ten rastered line patterns, 1.5 mm in length, were completed in three separate locations across the surface of the sample producing 459 spectra to be averaged. This was done as a means reduce the variance of measurement by reducing the effect of any inhomogeneity in the sample. Flowing argon was used as shielding gas. The linear velocity of the raster was set to 0.1 mm/s and the separation distance between each line of the pattern was 0.25 mm.

The non-resonant lines of singly-ionized aluminum and yttrium at 281.61 nm and 278.52 nm, respectively, were utilized for this analysis as they are well isolated and not inhibited by any spectral interference [64-66]. A representative emission spectrum, in the 273 nm to 287 nm spectral window, obtained from an unfired yttrium-aluminum oxide sample is displayed in Figure 52.

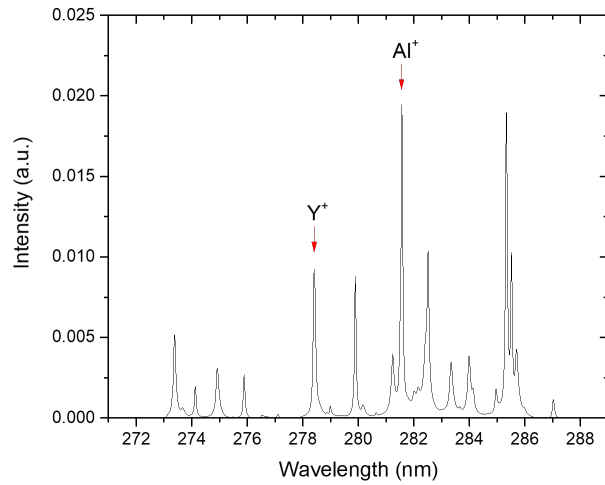


Figure 52: LIBS spectrum used for quantitative analysis, obtained from unfired yttrium-aluminum powder compact.

Figure 53 depicts the accumulated intensities of each species, across the 459 acquisitions for each sample.

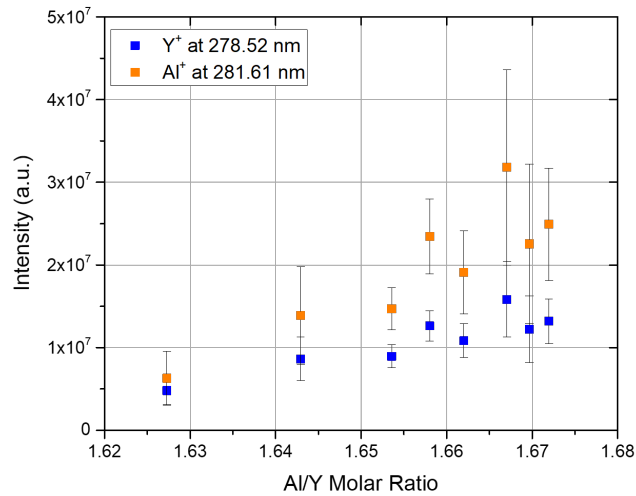


Figure 53: Intensity versus Al/Y molar ratio of prepared YAG green bodies obtained by quantitative analysis of LIBS data.

The standard deviation of the Al^+ species is much larger than that of the Y^+ species throughout all samples investigated. The increased uncertainty propagates into the standard deviation for the ratio of intensities. A plot of the ratio of the intensities of the Al^+ and Y^+ versus the molar ratio of each sample is shown below.

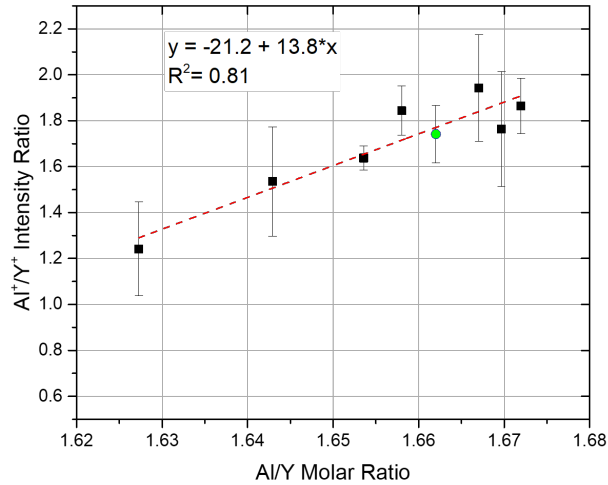


Figure 54: Al^+/Y^+ intensity ratio versus Al/Y molar ratio of prepared YAG green bodies obtained by quantitative analysis of LIBS data; the green circle represents stoichiometric YAG.

As shown in

Figure 55: , we have demonstrated, for the first time, the ability to obtain a positive monotonic correlation between the intensity ratio of Al^+ and Y^+ and their molar ratios, between the range $r = 1.627-1.672$, from unfired powder compact samples.

While this is movement in a positive direction, we acknowledge there is still more work to be done to overcome some shortcomings. The samples that were produced were not homogeneous due to inadequate blending of the additional Al_2O_3 into the starting powder mixture. This was evident in a matching set of samples that was sintered, where the number of white inclusions increased progressively with the quantity of addition. As can be seen above in Figure 54, the error of the intensity ratio is still quite large. Therefore, this data does not demonstrate the resolution necessary to reliably differentiate one sample from the next based on the obtained intensity ratio. Figure 53 shows that the error attributed to the Al^+ species is the dominant contribution to the overall uncertainty on the intensity ratio. We hypothesize that the enlarged error is related to both the inhomogeneity of the Al_2O_3 additions within the powder compacts and nonuniform density of the samples generated during cold uniaxial pressing. The effect of compaction and density has been studied previously and from these studies it can be concluded that if there is a variation of density throughout the sample due to the forming process one would see a larger shot-to-shot fluctuation of intensity [67, 68].

A positive monotonic calibration curve between the Al/Y intensity ratio and the molar ratio in non-reacted Al₂O₃-Y₂O₃ powder compacts can be obtained by LIBS about the stoichiometric YAG composition. However, due to the magnitude of error, originating mostly from Al⁺ species, this did not provide a resolution comparable to that of acquisitions from sintered ceramics. Better homogenization of the Al₂O₃ addition and a more uniform density distribution within the compacts may reduce this error, providing a higher resolution.

4.2.2.1 Ablation study on unfired YAG phase powder compacts

The ablation at the surface of soft bodies produces considerably more free particles that can negatively affect the equilibrium temperature of the plasma. Additionally, inside the powder compacts, there is a density distribution throughout the sample imparted during the cold pressing process. This density variation throughout the sample affects the ablation and temperature of the resulting plasma, which in turn increases the intensity variation from spot to spot.

To investigate if a binder could be used to reduce this effect an ablation study was performed to determine an appropriate binder that would provide a stronger surface and therefore produce less particulates during ablation. To perform this study, commercial YAG phase powder (not a mixture of Al₂O₃ and Y₂O₃ precursors) was used so the only variation in signal should emanate from only the ablation behavior of the surface. Four powder compacts of this powder were formed via cold compaction. The first with no binder, the second with a 5 wt% PMMA solution dropped directly onto the preformed pellet. For the final two parts, boric acid and KBr were dissolved into solutions with ethanol, both at a concentration of 5 wt%, then applied to loose powder prior to being formed into a pellets. During cold isostatic pressing it was expected that the applied pressure would cause these additives to flow throughout the sample, thereby binding all the particles more firmly together.

For the following acquisitions, the laser energy was set to 3.4mJ and three 5x5 grids were created. For each spot of the grid, 5 shots were accumulated. Each grid was placed approximately 120 degrees apart on the surface of the part. The variation across all acquisitions was then analyzed. To find the intensity ratio of Al/Y, the singly ionized peaks for Al⁺ (~278.5 nm) and Y⁺ (~281.5 nm) are utilized.

A microscopic evaluation of the craters created by ablation during LIBS did show a difference between the pellets with and without a binder; as well as between the different binders themselves. Shown below, in Figure 55, are images of the ablation behavior on the soft powder compacts with each binder.

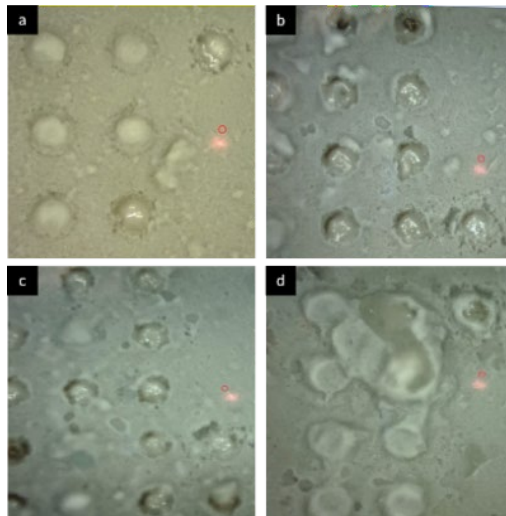


Figure 55: Ablation characteristics of soft formed bodies with different binders applied (a) No additive, (b) PMMA, (c) KBr, (d) Boric Acid.

From the above images, we see that the samples with no binder, or with KBr and PMMA additives experienced similar cratering and scattering of particles. These produced similar size craters with similar amount of particulate build up around the crater. The part with boric acid additive more brittle with larger diameter craters and flakes dislodging from the surface upon ablation.

Figure 57: is a box and whisker plot showing the variation of intensity ratio for each sample.

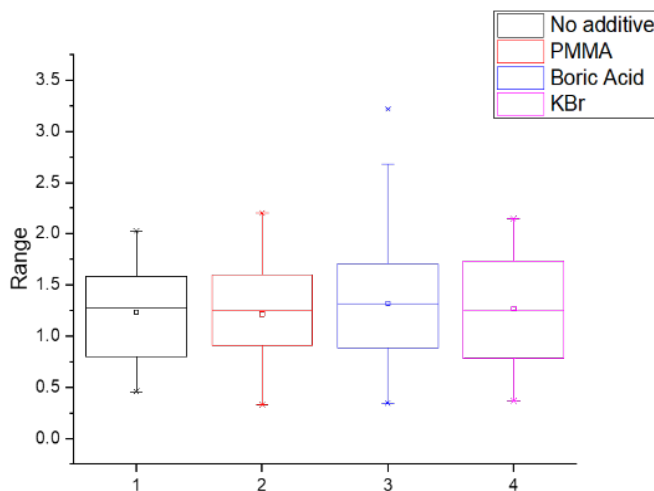


Figure 56: Al/Y intensity range for samples processed with different binders.

The samples with no additive, KBr, and PMMA have approximately the same range of variation of the intensity ratio. It can be noted that these samples also had the same cratering behavior. While the sample with boric acid has a much larger variation in the acquired signal from shot to shot. The PMMA produced the smallest interquartile range, but only slightly smaller than the sample with no additive. The sample with no additive has the smallest absolute range of variation. For this reason, it was determined that adding binder to powder compacts was not a viable way to reduce the variation of the intensity signal.

A study was performed on commercial YAG phase powders to determine if binder additives could reduce the shot-to-shot fluctuation of intensity during ablation via LIBS. While this eliminates the possibility of effects of inhomogeneity, possibly seen in the prior study, none of the binders investigated provide an appreciable reduction in intensity fluctuations.

4.2.3 LIBS analysis of YAG phase powder compacts of unknown composition by aqueous solution standard addition method

During this project, we began working with a commercial partner who produces YAG nanopowders by flame spray pyrolysis. The objective was to investigate the viability of using LIBS as an analytical technique to verify the composition of their powders and increase the consistency of their current process. The commercial partner supplied a sample of their recent product powder for this investigation.

To determine the composition of the YAG powder supplied by the commercial partner, a study was performed in which standard additions would be added to the provided “base” powder via aqueous solutions. While the definite composition of the base powder is unknown, it is assumed to be close to stoichiometry for the purpose of determining the addition step sizes, which were chosen in an attempt to stay within the linear regime of the Al/Y intensity vs Al/Y molar ratio. This region is labeled “Group 2” in the prior LIBS study of sintered ceramics in Figure 44, as was also shown to exist in the more recent study of powder compacts (Figure 54). Parts that fall outside of the continuous linear regime will not be useful to this analysis, as they will not fall onto the same linear calibration curve.

Standard addition by way of aqueous solution was chosen to provide better homogeneity than what was achieved using solid alumina in the previous investigation of powder compacts. Furthermore, no binder was used during consolidation as this was shown not to be effective in reducing shot-to-shot fluctuations.

It was determined that 500 μL of liquid was required to just wet, but not soak, the powder so as to prevent separation between the powder and liquid which would likely leave regions of higher concentration of added ions and the resulting pellet nonhomogeneous. Therefore, each solution application to the powder samples would be a volume of 500 μL .

Aqueous solutions of known Al^{3+} or Y^{3+} concentrations were created. The Al^{3+} solution was produced by dissolving aluminum ammonium sulfate in deionized (DI) water. For the Y^{3+} solution, yttrium nitrate was used and also dissolved into DI water. Four 5 mL Al^{3+} solutions of different but known concentrations were prepared, along with four 5 mL Y^{3+} solutions with the different but known concentrations. The base powder was calcined at 600°C to remove organics that were present and nine samples, each with a mass of 0.8 g, were ground using a boron nitride mortar that would limit any Al contamination. After application of the solutions to the powder samples, the step size of Al mol% would be the same in the yttrium rich direction as it was in the aluminum rich direction. The powder samples were then dried and reground in the boron nitride mortar to homogenize and limit the amount of agglomeration during the calcination process. Through the calcination the double salt introduced by the Al^{3+} solution and nitrates from the Y^{3+} solution is removed. The powders were then pressed into pellets. This created two sets of parts to be analyzed by LIBS, one with increasing Al^{3+} concentration and the other with increasing Y^{3+} concentration.

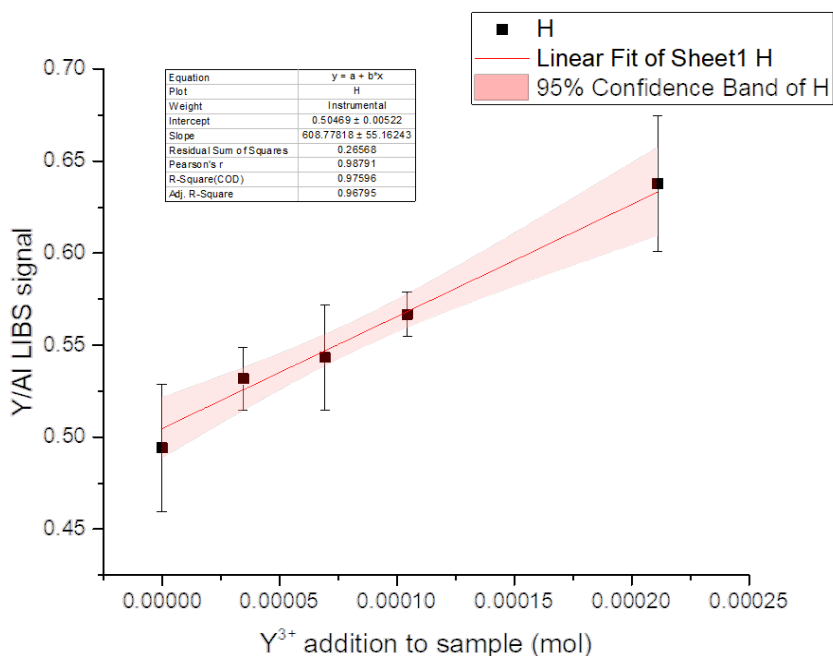


Figure 57: LIBS curve produced for parts with yttria additions.

The plot above shows the Y/Al signal intensity ratio vs the quantity of moles made on each sample during the additions. It should be noted here that we do not know the actual composition of any of these samples, but solely the number of ions added to each one. The point at the far left is the “base” powder with no addition. Taking the equation for the fitted line, we can compute the x-intercept. This point can be interpreted as the number of moles that would be needed to be removed from the base powder for the sample to have zero intensity. Therefore, this should be

the number of moles of yttrium present in the base powder. Using this technique, we find that this sample, comprised of only the “base” powder, brings an offset of $8.29\text{E-}4$ moles of Y^{3+} to the calibration curve.

Then this same technique described above can be employed for the Al^{3+} in order to find the number of moles of aluminum present in the base powder. Once these values are known, taking the Al/Y ratio should reveal the composition of the powder, which was previously unknown. Figure 58 shown below, is the calibration curve obtained by LIBS for the Al^{3+} additions.

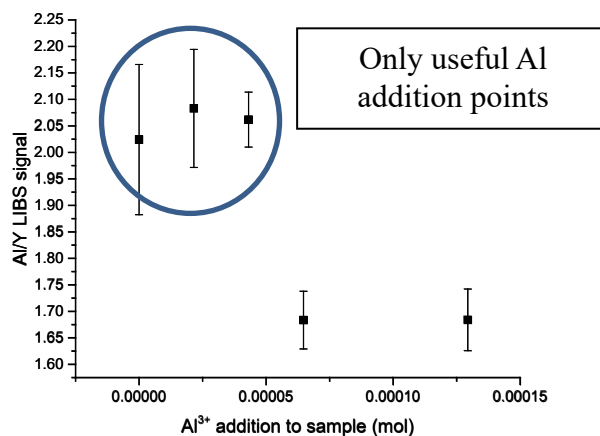


Figure 58: LIBS curve produced for parts with Alumina additions.

Here there are only three points that fall on the linear portion of the curve. These three points also have large uncertainties, which would provide a poor linear fit, and extrapolating the x-intercept to identify the number of moles of Al^{3+} would not yield a reliable result. Therefore, we were not able to implement the standard addition analysis in this case.

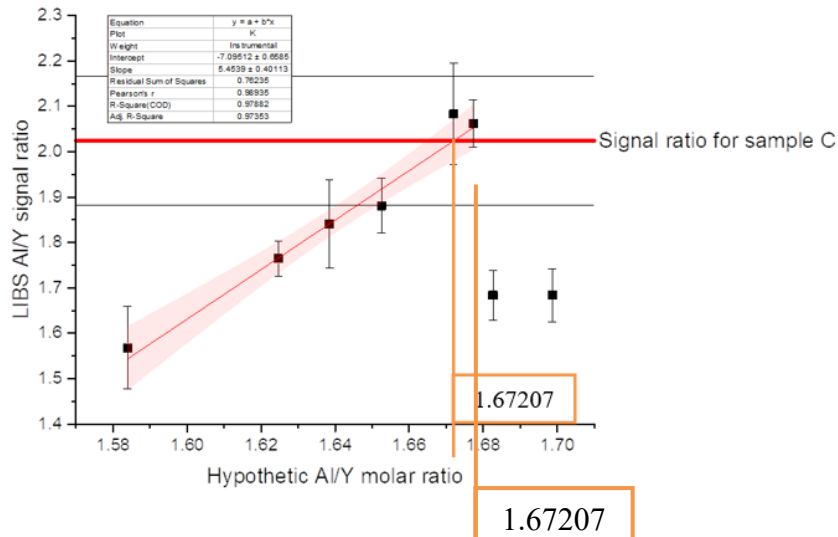


Figure 59: Plotting the Al/Y intensity ratio vs the hypothetical molar ratio with the assumption that the “base” powder had an initial ratio of 1.6667.

Unable to utilize the standard addition technique, an attempt was made to determine the composition of “base” powder through determining where the intensity ratio of this sample intersected the calibration curve found from the samples with the additions. However, the final molar ratios of these samples are hypothetical because this assumes that the base powder before spiking had a molar ratio of 5/3. The ratio of the “base” powder is then found to be 1.67207. For the above reasons, we believe this value to be invalid.

The use of aqueous solutions for the standard additions was effective in increasing the homogeneity, and reducing the error incurred during LIBS analysis. However, the composition of the sample provided by the commercial partner was not able to be determined by this method because some of the parts fell out of the continuous linear regime. This could be corrected by producing a set of Al additions with a smaller step size. Directly measuring the intensity ratio of the known against the calibration curve obtained from the full set of additions provided a value we deemed invalid.

4.2.3.1 Determination of composition YAG phase powder by ICP-MS

As a check on our LIBS analysis, we also conducted Inductive Coupled Plasma Mass Spectrometry (ICP-MS).

The glass beads used in the ICP-MS analysis composed of YAG infused into Li-Tetraborate. A mortar was used to mix 10 wt% base powder with the borate. The mixture was then be placed inside a graphite crucible and melted in a tube furnace, under an inert atmosphere, with a max

temperature just above the melting point of the Li-Tetraborate (917°C) in order to limit any volatilization of the lithium during the melting process.

To perform ICP-MS, the fused glass bead is digested completely into a 5% nitric acid solution. The resulting solution is then diluted down by a factor of 10^6 such that the concentration fits into the calibration range of the instrument. Standard additions are then performed on the diluted solution.

A summary of the standard additions is shown below in Table 3.

Table 3: Summary of concentrations used for standard additions to dissolved glass beads.

Solution	Concentration (ng/ml)	
	Al	Y
Addition 0	0	0
Addition 1	5.1716	5.2232
Addition 2	10.2701	10.3826
Addition 3	20.6506	20.9199
Addition 4	30.8347	31.299

After these additions were performed, the dilute solutions are pushed through the ICP-MS and the the concentration of Y and Al ions are subsequently measured. Standard addition calibration curves are developed from these measurements and shown below is Figure 60.

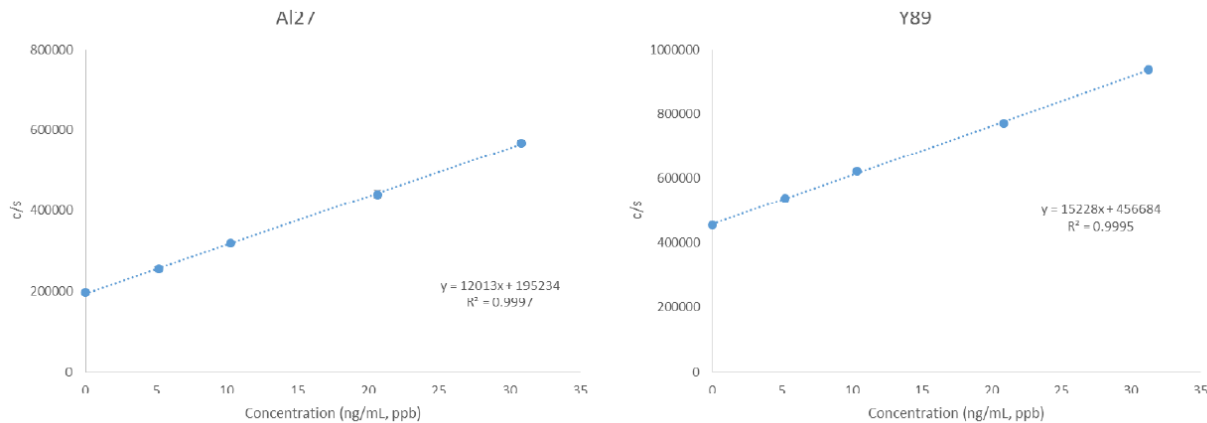


Figure 60: Standard addition curves obtained by ICP-MS (left) Aluminum (right) Yttrium.

As discussed previously, regarding the standard addition analysis, the equations for the fit of these curves will yield the concentration of each species in the sample with no addition by finding the x-intercept. When using the values found through this analysis, the Al/Y molar ratio is found to be 1.6568 +/- 0.0394. This is a much more reasonable result.

The ICP-MS analysis of the composition of the commercial powder by way of standard additions provided a more reasonable result than that of LIBS on powder compacts.

4.2.3.2 Ablation Sintering of YAG nanopowder

To confirm the validity of the values determined from the LIBS and ICP-MS results, one gram of supplied base powder was formed into a compact to be sintered. Figure 61 shows optical microscopy images of the sintered sample after polishing.

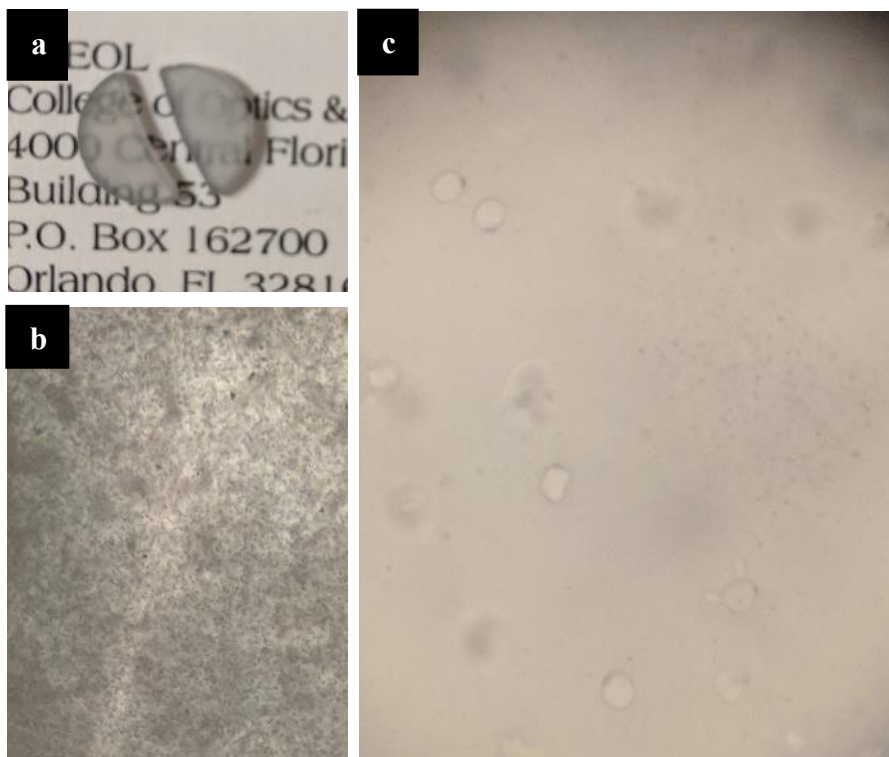


Figure 61: Images of sintered YAG FSP nanoparticles from customer. a) Polished transparent sintered ceramic b) Optical microscopy showing uniform porosity throughout sample at 5x c) Optical microscopy showing large pores at 50x.

The sample is transparent but contains a large amount of porosity. This can likely be attributed to the fact that no sintering aid was added prior to sintering. If TEOS had been added this part would likely be more transparent due to the silica helping control the grain growth rate and allowing the pores to be annihilated during densification. The molar ratio found by LIBS, 1.67207, actually lies just outside of the transparency regime so we feel this value is not realistic. We know that molar ratio 1.6568 lies within the transparency regime and therefore believe that the ICP-MS results are much more reasonable.

4.2.4 LIBS study of sintered ceramics, powder compacts, and fused glass beads with aqueous solution based standard addition

We have shown that we can obtain reliable and precise composition measurements by LIBS from fully dense sintered ceramics. However, there have been some complications obtaining this quality of results from less dense compacts. With the difficulty in obtaining reliable LIBS results from powder compacts due to the variation of density that is present, as opposed to fully sintered samples. After the experience making fused glass beads for ICP-MS analysis, we thought to use this same process but perform the analysis with LIBS. These fused beads are fully dense and will produce a much more stable plasma compared to green bodies. Additionally, when an analysis of a sample with an unknown composition needs to be conducted a new calibration curve needs to be created each time to correct for inherent fluctuations in laser power due to cooling. A set of fused glass standards lends itself to this application because there is much less surface damage upon ablation compared to that on powder compacts. After the surface of the glass standard has been ablated it can be polished down to provide a clean surface for the next analysis, where this is not possible for powder compacts. This processing route is quick and easy and could be applied to many other material systems when compositional control is critical.

Once we successfully fabricate a set of standards and obtain satisfactory results, this set can be used repeatedly to build a calibration curve each time the composition of a sample needs to be determined. This would also give us the capability to extract a small sample directly from the slurry, fuse this into a glass bead, and analyze this against the calibration curve to determine any deviation from stoichiometry at the beginning in the fabrication process. This includes any deviation brought about by contamination during ball milling.

Our goal is to apply LIBS as early in the process as possible before significant time is spent on the powder processing. It would make the most sense to do this directly after the mill process when the sources of error in the composition have already occurred. However, at this point the powder is loose and not compacted. Previous work on LIBS acquisition on loose powders has shown increased RSD in the intensity. This was found to be attributed to two factors: (i) plasma light shielding by powders that are not ablated but ejected and suspended in the air thus hindering the collection of light [69, 70] and (ii) surface roughness along the surface of the powder causing non-uniform ablation [67, 70]. These complications cause differences in the ablation from shot-to-shot, and therefore a fluctuation in the intensity. We believe that we have

identified a solution that will allow the precise determination of the composition directly after the ball milling process.

The proposed solution is to fuse the powder into a glass. A mixture of the $\text{Al}_2\text{O}_3\text{-Y}_2\text{O}_3$ powder can be mixed with a borate powder and upon melting the $\text{Al}_2\text{O}_3\text{-Y}_2\text{O}_3$ mixture will dissolve into the glass matrix. The beads can then be polished to present a fully dense and flat sample surface for ablation. This solution has been used for quantitative elemental analysis via LIBS by others in the past [71-75]. Additionally, when comparing LIBS on powder compacts versus fused glass beads it was found that the fused glass beads produce lower RSD and better fits of the calibration curve [72, 73, 75].

While LIBS on fused glass has been studied before, to our knowledge, no study has been performed on glass beads to determine the molar ratio of a powder mixture from the intensity ratio of majors or to quantify the ratio with the resolution we are seeking to achieve (0.1-0.3 mol%). Furthermore, there has not been a study to compare the analysis of sintered samples, powder compacts, and fused glass beads in the context of improving the fabrication of advanced ceramics.

Our hypothesis is that through fusion of YAG powder into glass beads we can use LIBS to establish a calibration curve that will be able to determine the deviation from stoichiometry with a resolution equal to or better than 0.3 mol%, which was previously determined to be the resolution on sintered parts by Pandey, *et al.* [55].

4.2.4.1 Experimental

Materials Preparation

The precursor powders Y_2O_3 (Alfa Aesar, 99.99%) and Al_2O_3 (Taimei Chemicals Co., LTD., 99.99%) are weighted and mixed to obtain a yttria rich composition with an Al/Y ratio of 1.6. TEOS (Sigma Aldrich, $\geq 99\%$) and ethanol were added to the powder mixture. Spherical 3 mm alumina balls (IRIE, Japan) were employed as a grinding media and the mixture was milled for 20 hours at 250 rpm. The slurry was dried to evaporate the solvent then sieved, followed by calcination at 800°C for 2 hours. The powder was subsequently divided out into 10 separate aliquots. Aluminum ammonium sulfate dodecahedral (Alfa Aesar, Reagent Grade) was mixed in deionized water to prepare a 1M solution. A predetermined volume of this solution was added to each aliquot to achieve the desired Al/Y ratio to make a series of parts with the composition varied about the stoichiometric YAG composition, where an Al/Y ratio of 1.667 corresponds to this stoichiometric compound. The powders were dried, mixed in a mortar, then calcined at 350°C to remove the crystallization water.

Table 4: Final Al/Y ratio for each aliquot of powder after addition of Aluminum Ammonium Sulfate solution.

Part Number	Final Al/Y Ratio
0	1.6000
1	1.6206
2	1.6353
3	1.6498
4	1.6570
5	1.6609
6	1.6655
7	1.6683
8	1.6727
9	1.6835

- Fused Glass Beads

To prepare the fused glass beads, 0.4 g of powder was removed from each of the aliquots and was mixed with 3.6 g of Lithium Tetraborate (Johnson Matthey) then calcined at 480°C for 4 hours. Immediately after cooling these mixtures were loaded into a cylindrical graphite die that has pockets to form 15 mm glass discs after melt. The parts were heated to 1050°C and soaked for 20 minutes then air quenched. The formed glass discs were then polished prior to analysis by LIBS.

- Powder Compacts

To prepare the powder compacts, 0.65 g of powder was removed from each of the aliquots and was uniaxially pressed at 20 MPa in a 13 mm steel die and then cold isostatically pressed at 250 MPa. The powder compacts were then calcined in air at 900°C for 1 hour then sealed under vacuum to prevent absorption of water prior to acquisition by LIBS.

- Sintered Parts

To prepare the sintered parts, 0.65 g of powder was removed from each of the aliquots and was uniaxially at 20 MPa in a 13mm steel die and cold isostatically pressed at 250 MPa. These compacts were then calcined in air at 900°C for 1 hour then subsequently sintered under vacuum at 1750°C for 16 hours. The parts were then polished prior to acquisition by LIBS.

4.2.4.2 Results

Shown below are the samples of fused glass and sintered parts with the composition varied across the set.

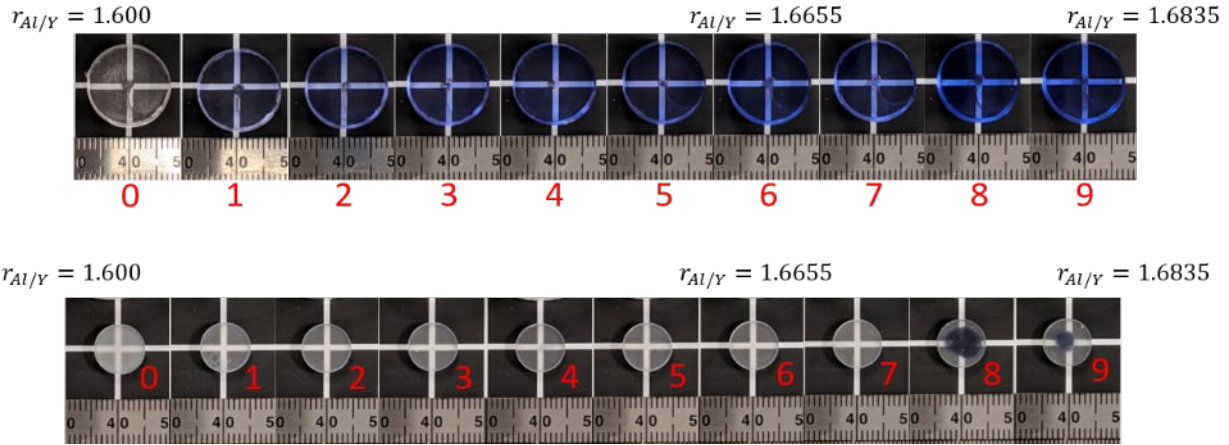


Figure 62: (top) YAG infused glass beads with the Al/Y ratio varied from 1.600 to 1.6835 across the set. (bottom) Sintered YAG ceramics with the Al/Y ratio varied from 1.600 to 1.6835 across the set.

The glass beads (top) are very transparent and homogeneous. They have taken a purple color that deepens with the increasing amount of the aluminum ammonium sulfate solution that was added. This might be attributed to organics or sulfates that may have remained on the powder during the fusing process. The sintered YAG samples (Figure 62 bottom) appear very uniform with almost no inclusions and the transparency varies across the set as was expected. However, parts 8 and 9 have black spots in the bulk which is evidence of absorption caused by the sulfate which was not able to be removed during calcination prior to sintering under vacuum. The presents of sulfur should not affect the acquisition by LIBS as it is in trace amounts. The sample set of powder compacts was produced also but is not shown above.

We are confident that these sample sets will allow for the Al/Y ratio to be determined across the different sample medias. We had begun optimization of acquisition parameters but encountered a problem with the laser during this time. Therefore, we have not been able to finish this study prior to the end of the funded project.

4.2.5 Fabrication of sintered YAG ceramics with the composition varied by standard addition with sulfates and nitrates

From this same batch of powder an additional sintered sample set was produced in hopes of sending them for PALS analysis. We were also investigating the use of an additive that could be used to adjust any deviation from stoichiometry determined by LIBS without having to scrap the current batch.

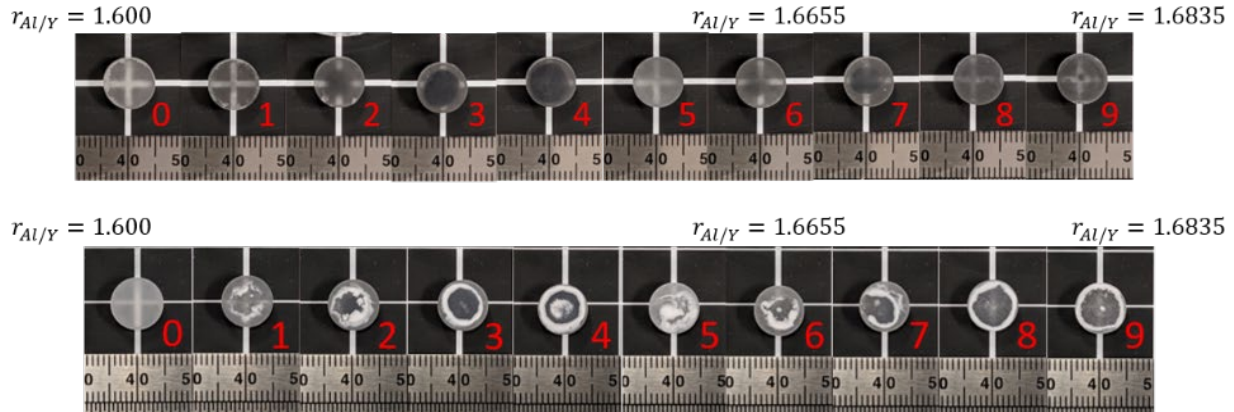


Figure 63: (top) Sintered YAG ceramics with the Al/Y ratio varied from 1.600 to 1.6835 across the set. (bottom) Sintered YAG ceramics with the Al/Y ratio varied from 1.600 to 1.6835 across the set, after annealing at 1250°C in air for 8 hours.

The parts shown above were processed the same as those discussed in the previous portion of section 4.2.4. However, the thickness of these parts was increased to a thickness of about 4 mm after cold isostatic pressing, compared to about 2.6 mm for the other sintered parts. After sintering in under vacuum the dark coloration and black spots are present in more of these parts than there was for the other set (Figure 63 top). We hypothesize this is because of the increased diffusion distance necessary to remove the sulfate during calcination prior to sintering. To see if the remnants of the sulfur could be removed by further heat treating the set was annealed at 1250°C in air for 8 hours. After treatment the coloration did not appear to decrease but there was a white residue on all of the parts that had the additive applied (Figure 63 bottom). Due to the inclusion of these black spots, we do not believe the parts are of sufficient quality for analysis by PALS.

The difficulty of removing sulfate from the surface of precursor oxide powders prior to sintering under vacuum makes the use of aluminum ammonium sulfate an unlikely candidate as an additive to correct composition of a powder mixture that is found to deviate from stoichiometry.

Following our experience with using aluminum solutions to produce sets of samples with varied composition and the difficulties with removing sulfate from the powders, we still wanted

to identify an additive that could create these samples sets while also identifying a candidate that could be used to correct the composition of a powder batch if it was found to deviate from stoichiometry after mixing. Nitrates have a significantly lower volatilization temperature as compared to sulfates, so Aluminum Nitrate was chosen as another additive candidate. Another batch of powder was prepared following the same protocol as described in section 4.2.2. The resulting part set is shown below.

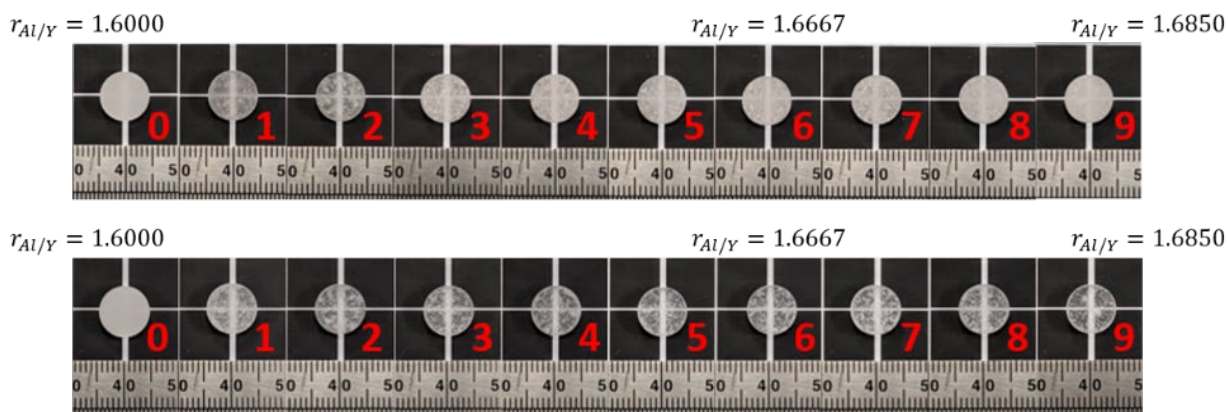


Figure 64: (top) Sintered YAG ceramics with the Al/Y ratio varied from 1.600 to 1.685 across the set. (bottom) The same set of parts after hot isostatic pressing at 1700°C and 200 MPa for 6 hours.

The sintered parts shown at the top of Figure 64 became less transparent with the increasing amount of additive that was applied. These parts contained what appears to be white spots throughout the bulk, optical microscopy showed an abundance of large pores or transparent secondary phase in these areas, but the densities were over 99% as measured by Archimedes' method. To determine if hot isostatic pressing (HIP) could eliminate this porosity the set of parts was HIP'ed at 1700°C and 200 MPa for 6 hours. The parts after this post processing are shown at the bottom of Figure 64. The parts still contain white spots due to localized high density porosity but are very transparent outside of these areas. We hypothesize that is because nitrate tends to be viscous and clump together (more so than sulfates). Upon drying the wetted powder, the nitrate re-agglomerated within leaving areas with an increased concentration of the aluminum nitrate, which after calcination leave areas of amorphous alumina, and the diffusion during sintering is not sufficient to redistribute this homogeneously the YAG lattice. Due to the occurrence of high pore content or secondary phase we do not believe that this set of parts is of sufficient quality for analysis by PALS. However, these parts could be analyzed by Cathode Luminescence (CL), Thermo-Stimulated Luminescence (TSL), and Electro-Paramagnetic Resonance (EPD) as we believe the coupling of these techniques provide the qualitative and quantitative information regarding defect content that we seek to obtain.

The increased porosity or evolution of secondary phase after vacuum sintering makes the use of aluminum nitrate an unlikely candidate as an additive to correct composition of a powder mixture that is found to deviate from stoichiometry.

4.2.6 Other accomplishments

We have filed a patent for a ‘*Method for fabricating an optical source for calibrating an optical system*’ (United States application 16/429,423, docket number 10669-283US0), which can provide spectral-calibration and spectral power density calibration of laser-induced breakdown spectroscopy (LIBS) systems. Our plug-and-play, compact, bright, and broadband (180 nm to about 2 μm) source can fit most commercial and experimental LIBS systems and advantageously replace dimmer and more bulky light sources that normally require additional components, such as integrating spheres, currently utilized in both qualitative and quantitative analyses. We have built several working prototypes and can share more specific details with AFOSR upon request.



Figure 65: Custom-build calibration unit in use in the Applied Spectra J200 LIBS system.

This equipment will allow us to monitor the temperature of plasmas precisely and enable us to confirm (or infirm!) the validity of our simulations and optimizations. This will also be crucial in reducing quantification errors in the composition analysis of ceramics.

4.3 Conclusions

Our protocols and plasma modeling are now at a point where we can begin making sufficiently accurate measurements of the Al/Y ratio in both precursors and YAG ceramic samples. However, additional work is still required to further improve the accuracy and stability of these measurements by improving plasma temperature calibration protocols.

5. Monitoring of sintering additive concentration and unintentional impurities by LIBS during the fabrication of transparent ceramics of YAG.

5.1 Objectives

Various ceramic applications require the sintering of parts to full density so as to enhance their structural, electronic or optical characteristics [76]. In many instances, this is accomplished by adding inorganic additives, at a percent level or less to ceramic powders, to help control the mobility of pores relative to the grain-boundaries during firing [77]. Monitoring the concentration of these additives throughout the ceramic fabrication process is integral to understanding their role on the evolution of the microstructure and to the optimization of the densification process. This state of affairs is well exemplified by the fabrication of pore-free, optically transparent, yttrium aluminum garnet laser ceramics [77]. In fact, it was shown that, within the solubility limit in YAG, higher concentrations of SiO₂ decrease both the sintering time and the temperature to achieve this result [78]. However, in some cases a segregation of silicon-rich phases has been observed at grain boundaries after sintering [8] and a strong linear correlation has been evidenced between the amount of silica and a broadband absorption loss in the visible and near-infrared [79]. Hence, recent fabrication efforts have aimed at reducing the amount of silica to limit the effect of such background absorption in this laser host, while allowing the fabrication of fully transparent parts.

The next sections summarize our work and findings with regard to the quantification of silica by the LIBS technique and the monitoring of the concentration of silica in YAG ceramics throughout the fabrication process. This work has been published in the *Journal of European Ceramic Society*.

5.2 Accomplishments

The use of silica as a sintering aid in the production of transparent YAG ceramics was first proposed by De With and Van Dijk [80]. While their work led to translucent parts only, their key finding was further improved using colloidal silica [81] and TEOS [82], eventually enabling the production of transparent and laser-grade ceramics. The beneficial effect of silica on the densification and microstructure evolution of YAG ceramics has since been studied and discussed in numerous publications [8, 42, 83-86]. However, despite its advantage, the presence of silica doping in the sintered body may not always be desired as it either leads to the formation of color centers [87] or secondary phases [79, 86, 88, 89], thereby degrading the material's laser efficiency. So far, only a small amount of research has been dedicated to the solubility of Si in YAG, in particular in relation to the production process of transparent YAG ceramics. Sun et al. analyzed YAG with very high Si content treated in air at 1550 °C [90], and Kuru *et al.*,

determined the solubility of Si and Ca in precipitated YAG powder heat-treated at 900°C [91]. The high temperature solubility limit of Si in 1 at.% Nd:YAG has recently been studied by Zamir *et al.* [92]. Ceramics sintered in a vacuum at 1700°C for 6 hours exhibit solubility values of 980±60 ppm when fast-cooled (200°C/s), and 650±60 ppm when slow-cooled (100°C/h). Similar values were reported by Ikesue *et al.* in 7.2 at.% Nd:YAG ceramics reactively-sintered in a vacuum at 1750°C for 10 hours, however the cooling rate was not specified [93]. With the initial amount of Si reaching values of about 2000 ppm [93] or even 3700 ppm [92], the results of these two studies also reveal the significant loss of silicon occurring during the fabrication process. It should be noted that despite the absence of secondary phases or compositional inhomogeneity in the samples made by Ikesue *et al.*, the large amount of Nd³⁺ causes distortions in the crystalline structure - a change in lattice constant was observed with increasing Si content- and affects the dissolution behavior of silica.

In an attempt to better understand the origin and the mechanism of this silica loss, we have quantified the amount of Si in YAG at different steps of the fabrication process on a series of samples with different sintering aid concentrations, introduced either in the form of TEOS or SiO₂. This quantification was carried out using Laser-Induced Breakdown Spectroscopy (LIBS), a powerful and sensitive technique, well-suited for the study of ceramics and the monitoring of Si content in YAG transparent ceramics as demonstrated in prior publications [55, 94].

5.2.1 *Experimental*

5.2.1.1 *Materials preparation*

A set of YAG mixtures with different Si contents was prepared from oxide powders (Y₂O₃, nanocerox; Al₂O₃, TM-DAR, Taimei) and TEOS (Sigma Aldrich) or SiO₂ soot (Sigma Aldrich) as a sintering additive. From the analysis of impurities in the oxide powders results an introduction of about 35 ppm of Si in the YAG, equivalent to 0.008 wt% of SiO₂. The compositions are listed in Table 5. The preparation process, described in [95], includes ball-milling of powders in ethanol slurries in polyethylene jars with alumina milling medium, followed by spray-drying and uniaxial pressing of the granulated powder, cold-isostatic pressing, calcination in air at 600°C and sintering in a vacuum (10⁻⁴ Pa) at 1735°C for 16 hours. The sintering was followed by an annealing step in air and, for the purpose of this study, two different treatments were evaluated: a lower temperature with a long holding time, 1100°C for 100 hours; and a higher temperature with a short holding time, 1300°C for 1 hour. The size of the sintered pellets was 12 mm in diameter and 2 to 3 mm in thickness.

Table 5: Compositions of YAG ceramic pellets evaluated in this study.

Sintering additive	None	TEOS (0.25 wt.%)	TEOS (0.5 wt%)	TEOS (1 wt.%)	SiO ₂ (0.144 wt.%)
Initial SiO ₂ content [wt.%]	0	0.068	0.141	0.275	0.144

5.2.1.2 Characterization

The microstructure of the ceramics was analyzed on a FE-SEM (SIGMA, Zeiss, Germany). The silicon content was measured using a LA-LIBS system (J200 Tandem, Applied Spectra, Inc.). Ten spectra were accumulated on a single location to improve the signal-to-noise ratio, and this acquisition was repeated, for each sample, over a grid of 100 different locations on a 10×10 spot grid over a 6.25 mm² area. The calibration was described in [94] a five-point calibration curve was obtained using a set of samples prepared from a stoichiometric mixture of aluminum and yttrium oxides with different additions of SiO₂ powder ranging from 0 to 1.08 wt.% of SiO₂. The amount of silica in the YAG samples was then measured using the integrated intensity ratio of neutral silicon (288.158 nm) and neutral yttrium (288.654 nm) lines. Spectral emission lines were identified using the National Institute of Standard and Technology (NIST) database [60]. The detection limit was 0.0017 wt.% of SiO₂ (8 ppm of Si) and the quantification limit was 0.0463 wt.% of SiO₂ (216 ppm of Si). The analyses were performed at every step of the preparation process, as illustrated below in the further sections.

5.2.2 Results and discussion

5.2.2.1 Microstructure

Figure 66 shows, on a same scale, the fracture surface of reactively-sintered YAG ceramic samples with 0, 0.25, 0.5 and 1 wt.% TEOS additions, respectively. As already shown in prior publications [7, 88, 96], this addition has a dramatic effect on the ceramic microstructure both in term of grain size (the grains grow larger with increasing TEOS content) and porosity (the density and size of the pores reach a minimum for an initial addition of 0.5 wt.% TEOS). The sample without TEOS (Figure 66a) contains a significant amount of porosity which contributes to its opacity (Figure 67a), and fracture is mostly extragranular. For an initial addition of 0.25 wt.% TEOS (Figure 66b), the pores remain at the triple junctions, and at a level of 0.5 wt.% (Figure 66c), the ceramic is devoid of pores and is transparent (Figure 67c). At 1 wt.% TEOS (Figure 66d), the grains grow much too fast and the pores detach from the grain-boundaries, yielding closed residual porosity entrapped within the grains. Fracture is essentially intragranular in this case.

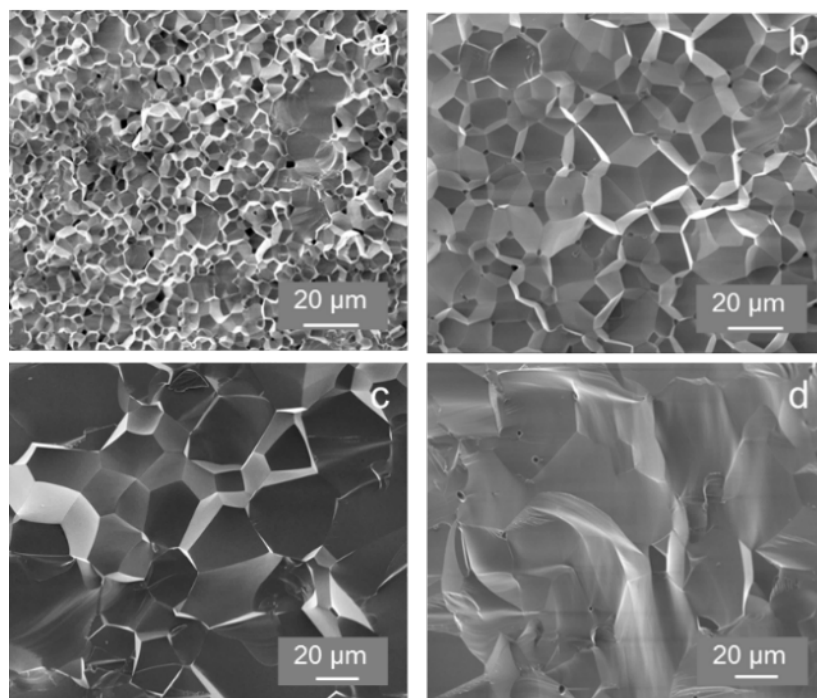


Figure 66: Fracture surface seen by SEM of YAG ceramic samples obtained with an initial addition of 0 (a), 0.25 (b), 0.5 (c) and 1 wt.% (d) of TEOS.

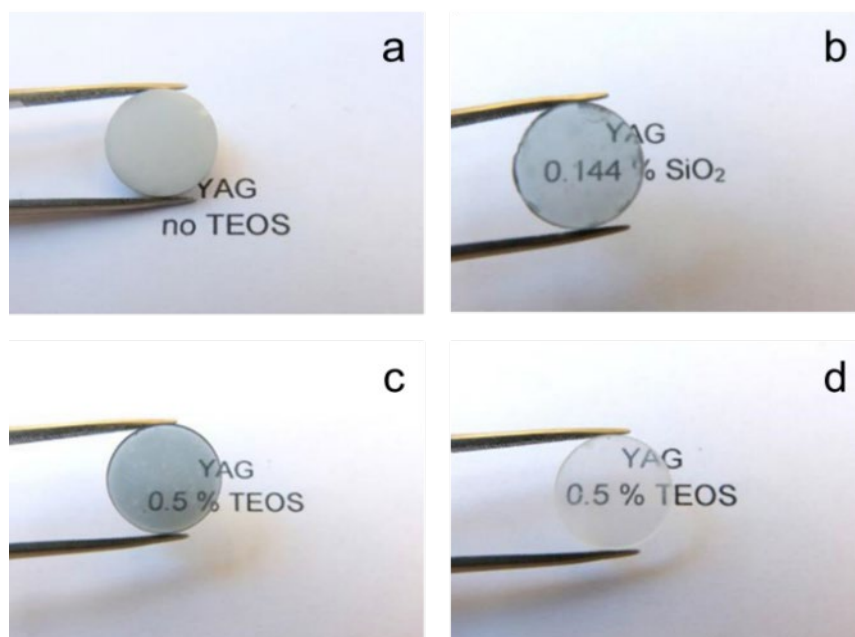


Figure 67: Photographs of reactively-sintered YAG ceramics without sintering additive (a), with 0.144 wt.% SiO₂ (b), with 0.5 wt.% TEOS (c) and with 0.5 wt.% TEOS after annealing (d).

5.2.2.2 LIBS characterization

The LIBS spectra, obtained at the different steps of the preparation process, are shown in Figure 68 for samples containing 0, 0.25, 0.5 and 1 wt.% of TEOS.

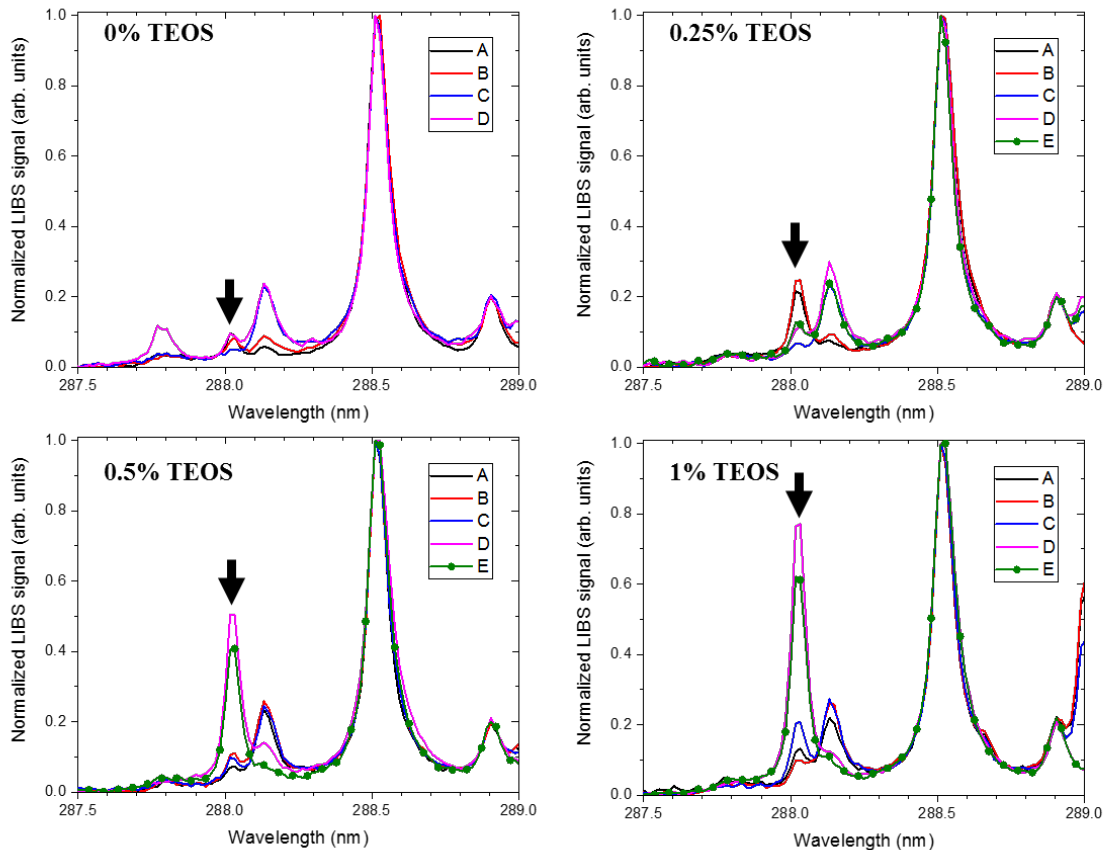


Figure 68: Selected spectral window of the recorded LIBS spectra showing the Si peak used for quantification (arrow at 288.158 nm). The main peak at 288.654 nm is that of neutral yttrium. On each figure, the different spectra correspond to the green-body (A), the calcined (B), vacuum-sintered (C) and annealed samples at 1100°C for 100 hours (D) or at 1300°C for 1 hour (E).

The combined results of the analysis are plotted in Figure 69 and show, for each initial Si-doping level, the evolution of the silicon content throughout the entire fabrication process. As expected, silica is not lost during the mixing/spray-drying process as TEOS has fully hydrolyzed and converted to SiO₂ by the time the slurry is granulated in the spray-dryer. After calcination of the pellets, a slight increase in the silica concentration is observed, which we interpret as a possible artifact due to the higher efficiency of the LIBS ablation process on the now hardened samples. Then follows a significant drop (>80 %) in silica content upon vacuum sintering. The

massive elimination of silica during the sintering step may be explained by a mechanism presented in the work of Boulesteix *et al.* [83], who have studied the effect of SiO₂ sintering additive on the fabrication of transparent YAG ceramics. These authors make the reasonable statement that, at high temperatures and under low oxygen partial pressures, gaseous silicon monoxide SiO evolves from the silica-rich secondary phases and contributes to the formation of porosity. At longer sintering times, this vapor transport also contributes to lowering the silica content of the bulk.

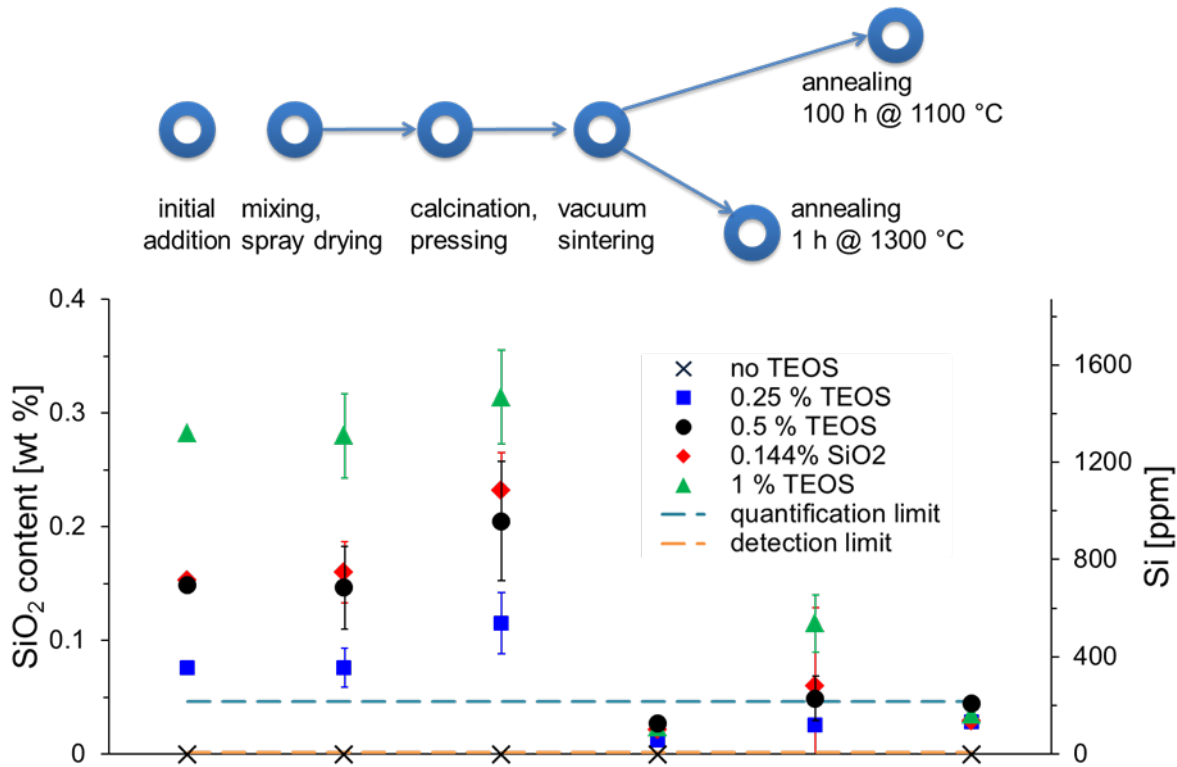


Figure 69: Silicon content measured by LIBS and reported in equivalent SiO₂ weight content, at various stages of the preparation of reactively-sintered YAG ceramics; the initial addition value was calculated from the actual weighing.

In order to validate this hypothesis, we measured the spatial distribution of silicon across the sections of a subset of samples (0.25 and 0.5 wt.% TEOS and 0.144 wt.% SiO₂ i.e. equivalent to 0.5 wt.% TEOS) that had undergone vacuum-sintering followed by an annealing step at 1100°C for 100 hours or 1300°C for 1 hour. This mapping was performed by in-depth scanning using LIBS laser pulses to drill through the samples. The resulting maps are shown in Figure 70 and indicate a difference in the amount of Si in the samples with 0.5 wt.% TEOS and 0.144 wt.% SiO₂. Even though the amount of Si in the powder mixtures used for the preparation of these two samples was nearly identical, the measured values differ (Figure 69) but remain within the error bars of the analysis. The samples with 0.144 wt.% SiO₂ contain a consistently higher amount of Si, with a decrease towards the surface. The observed influence of the annealing cycle was not

significant in the case of TEOS addition. In the case of the sample prepared with 0.144 wt.% SiO₂ soot, the distribution of Si appears to vary between the annealing at 1300 °C where the distribution appears uniform, and the annealing at 1100 °C where the Si content is lower in the upper surface layer in comparison to the bulk. This leads to the conclusion that, after the sintering process, the amount of Si in the surface layer is lower, but the annealing at a higher temperature may promote further diffusion of Si in the sample, providing a more uniform distribution.

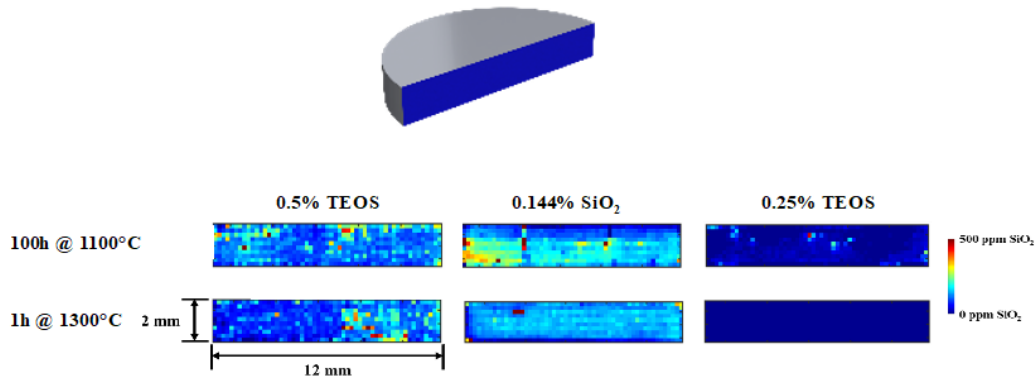


Figure 70: In-depth profiles of Si concentration measured by LIBS for annealed samples at 1100 °C for 100 hours (first row images) and 1300 °C for 1 hour (second row images).

The SiO₂ concentrations measured in our study are lower than those previously reported by Ikesue *et al.* [93] and Zamir [92], as shown in Figure 71. We believe that the difference in soaking time (16 hours at the sintering temperature in our work versus 10 and 6 hours, respectively) may not account for this difference entirely. It is possible that the presence of rare-earth dopants like Nd³⁺ helps retain silicon as suggested in [93].

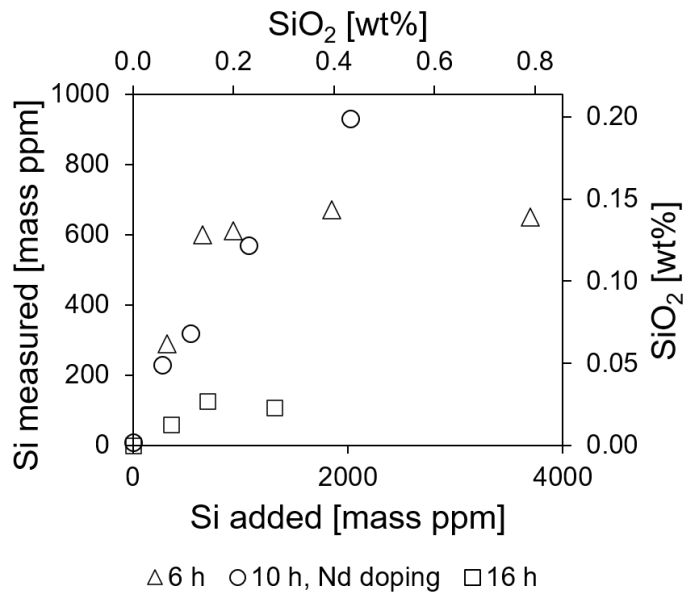


Figure 71: Comparative quantification of silicon in green- and sintered-bodies of reactively-sintered Nd:YAG ceramics; data from [92] (triangles), [93] (circles) and this paper (squares).

The difference between Si-doping using TEOS or silica soot does not seem to make a significant difference on the subsequent evaporation loss during sintering. The measured amount of silica is slightly higher in the case of YAG with silica soot; however, this difference already occurs in the green-body before sintering, and may thus be attributed to the variation in the powder preparation (e.g. weighing or evaporation of a small part of TEOS). A stronger effect of the annealing conditions is observed in the case of samples doped with silica soot.

5.3 Conclusion

The SiO₂ content of SiO₂-doped YAG ceramic samples has been measured and mapped by LIBS at four different steps of their fabrication process. We show that the ceramics experience a major SiO₂ loss during sintering under vacuum, on the order of 80 to 90 wt. %. ***This result supports the fact that reactively-sintered transparent YAG ceramics, in which SiO₂ is incorporated as a sintering additive, can be adequately processed to reduce the concentration of color centers and the production of low optical loss material suitable for high-power laser applications.***

6. Project Conclusions

6.1 YAG ceramic fabrication

Identification of the sources of error, and related uncertainties, in the fabrication process is important in ensuring repeatable product quality. The model developed allows for assessing the relevance of each source of uncertainty. Once the relevancies were determined, approaches were developed to reduce the uncertainties that bring the largest contributions, thereby increasing the repeatability of product quality.

The uncertainty attributed to a pile of particles randomly dispersed across the balance plate has a larger variance in the moment applied, compared to placing a mass repeatability in the center of the plate. Of all uncertainties identified in the process, this is the smallest contribution. If there were only this uncertainty, the probability of stoichiometry and transparent parts would be virtually 100% so long as the rest of the process is optimized.

Regarding the issue of the alumina deposit coming from the ball-milling process, we have found that the current means to quantify this is not only complex and time consuming, but very imprecise. This can be one of the largest uncertainty contributions in the fabrication process, depending on magnitude of uncertainty from the loss-on-ignition measurement. We have proposed an approach to a solution that would unique approach that would provide accurate determination of the total amount of alumina deposited during milling for the first time.

The loss-on-ignition measurement of precursor powders is critical to controlling the composition, and quality of the final product. These measurements can also be a very large contribution to the total uncertainty of the final composition. The TGA analysis of nanoparticles, on a dual beam thermal analyzer and for the purpose of quantifying LOIs is more sensitive than with coarse particles not only because (i) they have more surface area and experience more desorption, but (ii) they also have a tendency to sinter and walk during the thermal cycle. While we can minimize the walk of the crucibles on the platform by pinning them, it is more difficult to control the movement of the sintered sample inside this crucible. A possible approach to limit this effect would be to utilize crucibles designed to self-center the powder during the thermal cycle, for which a patent has been filed.

The novel statistical analysis approach demonstrates that if the uncertainty sources within the fabrication process are identified and quantified then parts within the limited solid solubility domain can be repeatably achieved. This achievement lays the framework to provide more repeatable quality of transparent ceramics, and other multinary compounds. Additionally, it provides a methodology to assess and further reduce uncertainty contributions. Thereby, making targeting of distinct composition within the solid solution possible. Finer scale defect engineering would be facilitated in this material system as well as other systems with limited solubility domains such as YIG, GAGG, ect. The amount of necessary precision depends on the specific application, and some may only care to guarantee to be within solid solution. However,

this lays the groundwork for better quality control and promotes a more repeatable fabrication process.

A study was conducted utilizing a contamination free mixing technology, as a means to eliminate this complication from the process. Despite its potential benefits in other applications, our investigations suggest that this mixing technology, in its present development state, is not sufficient to provide both intimate mixing and de-agglomeration for the fabrication of TOCs by reactive sintering.

The various insights we have gained on the control of our transparent ceramic fabrication process have seen a drastic improvement in sample quality. The consistency of sample quality originating from different batches and the recent laser test on a 6 at.% Tm:YAG TOC sample confirm our better understanding of the synthesis of oxide garnets, and our stronger hold on their fabrication process.

6.2 Laser-Induced Breakdown Spectroscopy (LIBS): A novel method for the assessment of stoichiometry in optical ceramics

Our plasma modeling results show that the Al^+/Y^+ intensity ratio, corresponding to atomic emissions at 281.61 nm for Al^+ and 278.52 nm for Y^+ , varies sharply above 12,000 K implying that experiments should be carried out at plasma temperatures below this value to minimize shot-to-shot fluctuations on the intensity ratio. However, simulated calibration curves at different plasma temperatures show that the sensitivity increases from $m = 0.04$ to 2.6 when the temperature is increased from 10,000 K to 17,000 K. Given that the intensity ratios are too small to be experimentally resolved at lower temperatures, and that a sensitivity greater than $m = \frac{6\sigma_{IR}}{\Delta M_R}$ is required to differentiate molar ratios with 99% confidence, this modeling work suggests that plasma temperatures on the order of 14,000 K should provide sufficient sensitivity while maintaining the standard deviation of the intensity ratio smaller than $m \times \Delta M_R$.

A positive monotonic calibration curve between the Al/Y intensity ratio and the molar ratio in non-reacted $\text{Al}_2\text{O}_3\text{-Y}_2\text{O}_3$ powder compacts can be obtained by LIBS about the stoichiometric YAG composition. However, due to the magnitude of error, originating mostly from Al^+ species, this did not provide a resolution comparable to that of acquisitions from sintered ceramics. Better homogenization of the Al_2O_3 addition and a more uniform density distribution within the compacts may reduce this error, providing a higher resolution.

A study was performed on commercial YAG phase powders to determine if binder additives could reduce the shot-to-shot fluctuation of intensity during ablation via LIBS. While this eliminates the possibility of effects of inhomogeneity, possibly seen in the prior study, none of the binders investigated provide an appreciable reduction in intensity fluctuations.

The use of aqueous solutions for the standard additions was effective in increasing the homogeneity, and reducing the error incurred during LIBS analysis. However, the composition of the sample provided by a commercial partner was not able to be determined by this method

because some of the parts fell out of the continuous linear regime. This could be corrected by producing a set of Al additions with a smaller step size. Directly measuring the intensity ratio of the known against the calibration curve obtained from the full set of additions provided a value we deemed invalid.

The ICP-MS analysis of the composition of the commercial powder by way of standard additions provided a more reasonable result than that of LIBS on powder compacts. This result was corroborated by the transparency of a sintered sample.

In an attempt to assess the composition as early in the process as possible we have proposed using fused glass as a host for the raw powder to present a flat dense surface for ablation. While LIBS on fused glass has been studied before, to our knowledge, no study has been performed on glass beads to determine the molar ratio of a powder mixture from the intensity ratio of majors or to quantify the ratio with the resolution we are seeking to achieve (0.1-0.3 mol%). Furthermore, there has not been a study to compare the analysis of sintered samples, powder compacts, and fused glass beads in the context of improving the fabrication of advanced ceramics. We have prepared a sample set to complete this study.

In trying to find an additive that can be used to adjust the composition of a batch upon determination that it deviated from stoichiometry aluminum ammonium sulfate and aluminum nitrate were investigated. The difficulty of removing sulfate from the surface of precursor oxide powders prior to sintering under vacuum makes the use of aluminum ammonium sulfate an unlikely candidate. Aluminum nitrate is neither a good candidate due to finding increased porosity or evolution of secondary phase after vacuum sintering

A novel device which can provide spectral-calibration and spectral power density calibration of laser-induced breakdown spectroscopy (LIBS) systems was patented as is titled '*Method for fabricating an optical source for calibrating an optical system*'. Several working prototypes were designed and built. This equipment will allow us to monitor the temperature of plasmas precisely in commercial LIBS systems and enable us to confirm (or infirm!) the validity of our simulations and optimizations. This will also be crucial in reducing quantification errors in the composition analysis of ceramics.

6.3 Monitoring of sintering additive concentration and unintentional impurities by LIBS during the fabrication of transparent ceramics of YAG

A study was conducted to quantify silica, used as a sintering aid, by the LIBS technique and the monitor the concentration of silica in YAG ceramics throughout the fabrication process. This work has been published in the *Journal of European Ceramic Society* under the title "*Monitoring the evaporation loss of silica sintering additive by LIBS during the fabrication of transparent YAG ceramics.*"

In this study, the SiO₂ content of SiO₂-doped YAG ceramic samples were measured and mapped by LIBS at four different steps of their fabrication process. We show that the ceramics

experience a major SiO₂ loss during sintering under vacuum, on the order of 80 to 90 wt. %. This result supports the fact that reactively-sintered transparent YAG ceramics, in which SiO₂ is incorporated as a sintering additive, can be adequately processed to reduce the concentration of color centers and the production of low optical loss material suitable for high-power laser applications.

6.4 Summary

We believe this work has met the objectives to develop robust fabrication protocols. We have further developed analytical methods that can provide highly accurate assessment of ceramic powder composition in order to guarantee the consistency of the fabrication process of YAG transparent ceramics. We believe these contribution help put the fabrication of high-quality optical ceramics on a firmer scientific ground than previous trial-and-error practices.

7. Communications

Papers:

- [1] M. Martinez, C. Bayne, D. Aiello, M. Julian, R. Gaume, M. Baudelet, “*Multi-elemental matrix-matched calcium hydroxyapatite reference materials for laser ablation: Evaluation on teeth by laser-induced breakdown spectroscopy*”, Spectrochim. Acta B **159** 105650 (2019)
- [2] J. Hostaša, A. Piancastelli, S.J. Pandey, M. Martinez, M. Baudelet, R. Gaume, “*Monitoring the evaporation loss of silica sintering additive by LIBS during the fabrication of transparent YAG ceramics*”, Ceramics International, **45**(9), 12274-12278 (2019)
- [3] S. Pandey, R. Locke, R. Gaume, M. Baudelet, “*Effect of powder compact density on the LIBS analysis of Ni impurities in alumina powders*”, Spectrochim. Acta B **148**, 99-104 (2018)

Conferences:

a) Invited talks:

- [1] R. Gaume*, S.J. Pandey, M. Julian, M. Baudelet, “*Stoichiometry assessment by Laser-Induced Breakdown Spectroscopy in the fabrication of optical ceramics*”, OSA Advanced Photonics 2018, NOMA, Zurich, Switzerland, July 2-5, 2018.

b) Contributed talks:

- [1] J. Hostaša*, S.J. Pandey, M. Julian, M. Baudelet, R. Gaume, “*Stoichiometry assessment by Laser-Induced Breakdown Spectroscopy in the fabrication of optical ceramics*”, Laser Ceramic Symposium, Okazaki, Japan, November 26, 2018.
- [2] J. Hostaša *, S.J. Pandey, M. Julian, M. Baudelet, R. Gaume, “*Stoichiometry assessment by Laser-Induced Breakdown Spectroscopy in the fabrication of optical ceramics*”, 12th International Conference on Ceramic Materials and Components for Energy and Environmental Applications (CMCEE-12), American Ceramic Society, Singapore, July 22-27, 2018.

AFOSR program review:

- [1] M. Julian, R. Gaume, “*Optical Ceramics Science for High-Power Lasers*”, AFOSR program review, October 2020, Virtual
- [2] M. Julian, R. Gaume, “*Optical Ceramics Science for High-Power Lasers*”, AFOSR program review, May 2019, Washington D.C.
- [3] M. Julian, C. French, R. Gaume, “*Optical Ceramics Science for High-Power Lasers*”, AFOSR program review, May 2018, Niceville FL.

Patent Applications:

R. Gaume, M. Julian, “*Self-centering crucibles for precision thermogravimetric analysis*”

- Application processing, University of Central Florida

R. Gaume, M. Baudalet, M. Julian, “*Method for fabricating an optical source for calibrating an optical system*” (United States application 16/429,423, docket number 10669-283US0),

8. References

1. Patel, A.P., et al., *Mechanisms of nonstoichiometry in Y₃Al₅O₁₂*. Applied Physics Letters, 2008. **93**(19): p. 191902.
2. Collongues, R., *Nonstoichiometry in oxides*. Progress in crystal growth and characterization of materials, 1992. **25**(4): p. 203-240.
3. Kuklja, M.M., *Defects in yttrium aluminium perovskite and garnet crystals: atomistic study*. Journal of Physics: Condensed Matter, 2000. **12**(13): p. 2953.
4. Kuklja, M.M. and R. Pandey, *Atomistic Modeling of Native Point Defects in Yttrium Aluminum Garnet Crystals*. Journal of the American Ceramic Society, 1999. **82**(10): p. 2881-2886.
5. Kröger, F.A. and H.J. Vink, *Relations between the concentrations of imperfections in crystalline solids*, in *Solid state physics*. 1956, Elsevier. p. 307-435.
6. Liu, J., et al., *Effects of ball milling time on microstructure evolution and optical transparency of Nd:YAG ceramics*. Ceramics International, 2014. **40**(Part A): p. 9841-9851.
7. Lee, S.-H., et al., *Hot Isostatic Pressing of Transparent Nd:YAG Ceramics*. Journal of the American Ceramic Society, 2009. **92**(7): p. 1456-1463.
8. Stevenson, A.J., et al., *Effect of SiO₂ on Densification and Microstructure Development in Nd:YAG Transparent Ceramics*. Journal of the American Ceramic Society, 2011. **94**(5): p. 1380-1387.
9. Boulesteix, R., et al., *Microstructural Evolution During Vacuum Sintering of Yttrium Aluminum Garnet Transparent Ceramics: Toward the Origin of Residual Porosity Affecting the Transparency*. Journal of the American Ceramic Society, 2013. **96**(6): p. 1724-1731.
10. Bonnet, L., et al., *Influence of (Nd+Y)/Al ratio on sintering behavior and optical features of Y_{3-x}Nd_xAl₅O₁₂ ceramics for laser applications*. Optical Materials, 2018. **77**: p. 264-272.
11. Boulesteix, R., et al., *Manufacturing of Large Size and Highly Transparent Nd:YAG Ceramics by Pressure Slip-Casting and Post-Sintering by HIP: An Experimental and Simulation Study*. Materials, 2020. **13**(9): p. 2199.
12. Yianatos, J., et al., *The effect of fines recycling on industrial grinding performance*. Minerals Engineering, 2005. **18**(11): p. 1110-1115.
13. Govender, I., et al. *Using positron emission particle tracking (PEPT) to investigate industrial systems*. in *XXV International Mineral Processing Congress 2010, IMPC 2010*. 2010. Australasian Institute of Mining and Metallurgy.
14. Makokha, A.B., M.H. Moys, and M. Vangu, *Application of gamma emission imaging in mineral processing industry: case study of slurry transport in a wet laboratory ball mill*. Measurement Science and Technology, 2011. **22**(4): p. 045706.
15. Vinnett, L., et al., *The use of radioactive tracers to measure mixing regime in semi-autogenous grinding mills*. Minerals Engineering, 2018. **115**: p. 41-43.
16. Wagner, M., 7 - *Differential Scanning Calorimetry*, in *Thermal Analysis in Practice*, M. Wagner, Editor. 2018, Hanser. p. 66-143.

17. Wagner, M., 9 - *Differential Thermal Analysis*, in *Thermal Analysis in Practice*, M. Wagner, Editor. 2018, Hanser. p. 158-161.
18. Xie, W. and W.-P. Pan, *Thermal characterization of materials using evolved gas analysis*. Journal of Thermal Analysis and Calorimetry, 2001. **65**(3): p. 669-685.
19. Yang, H., et al., *Characteristics of hemicellulose, cellulose and lignin pyrolysis*. Fuel, 2007. **86**(12): p. 1781-1788.
20. Skreiberg, A., et al., *TGA and macro-TGA characterisation of biomass fuels and fuel mixtures*. Fuel, 2011. **90**(6): p. 2182-2197.
21. Shi, L., et al., *Pyrolysis behavior and bonding information of coal—A TGA study*. Fuel Processing Technology, 2013. **108**: p. 125-132.
22. Weissenborn, P., J. Dunn, and L. Warren, *Quantitative thermogravimetric analysis of haematite, goethite and kaolinite in Western Australian iron ores*. Thermochemica acta, 1994. **239**: p. 147-156.
23. Giachetti, T., et al., *Discriminating secondary from magmatic water in rhyolitic matrix-glass of volcanic pyroclasts using thermogravimetric analysis*. Geochimica et Cosmochimica Acta, 2015. **148**: p. 457-476.
24. Wang, H., et al., *Classification and physical characteristics of bound water in loess and its main clay minerals*. Engineering Geology, 2020. **265**: p. 105394.
25. Cervantes-Uc, J., et al., *TGA/FTIR study on thermal degradation of polymethacrylates containing carboxylic groups*. Polymer degradation and stability, 2006. **91**(12): p. 3312-3321.
26. Menczel, J.D. and R.B. Prime, *Thermal analysis of polymers*. 2009.
27. Giżyński, M. and B. Romelczyk-Baishya, *Investigation of carbon fiber-reinforced thermoplastic polymers using thermogravimetric analysis*. Journal of Thermoplastic Composite Materials, 2021. **34**(1): p. 126-140.
28. Craig, D.Q. and M. Reading, *Thermal analysis of pharmaceuticals*. 2006: CRC press.
29. Yoshida, M.I., et al., *Thermal analysis applied to verapamil hydrochloride characterization in pharmaceutical formulations*. Molecules, 2010. **15**(4): p. 2439-2452.
30. Esposito, L., A.L. Costa, and V. Medri, *Reactive sintering of YAG-based materials using micrometer-sized powders*. Journal of the European Ceramic Society, 2008. **28**(5): p. 1065-1071.
31. Ge, X.-X., et al., *Influence of combustion reagent and microwave drying method on the characteristics of nano-sized Nd³⁺:YAG powders synthesized by the gel combustion method*. Journal of Sol-Gel Science and Technology, 2009. **52**(2): p. 179-187.
32. Kafili, G., et al., *The effects of TEOS on the microstructure and phase evolutions of YAG phase by formation of alumina/yttria core-shell structures*. Journal of the American Ceramic Society, 2017. **100**(9): p. 4305-4316.
33. Kumar, S.A. and J. Senthilselvan, *Co-precipitation synthesis and spectroscopic studies of YAG and Yb: YAG nanopowder for opto-electronic applications*. Transactions of the Indian Institute of Metals, 2015. **68**(2): p. 153-159.
34. Muresan, L., et al., *Investigation of thermal decomposition of yttrium-aluminum-based precursors for YAG phosphors*. Journal of Thermal Analysis & Calorimetry, 2012. **110**(1): p. 341-348.
35. Sharma, G., et al., *The influence of dopants on the surface enthalpy of Yttrium aluminum garnet (YAG)*. Thermochemica Acta, 2020. **683**: p. 178471.
36. Si, W., et al., *Kinetics of synthesis of YAG nanocrystals by ultrasound and ultrasound-microwave-assisted methods*. Journal of Wuhan University of Technology-Mater. Sci. Ed., 2016. **31**(3): p. 548-552.
37. Wang, L., et al., *Preparation of YAG ceramics through a novel process*. Ceramics International, 2012. **38**(1): p. 855-859.
38. You, Y., et al., *Preparation of YAG nano-powders via an ultrasonic spray co-precipitation method*. Ceramics International, 2013. **39**(4): p. 3987-3992.
39. Alderighi, D., et al., *Characterization of Yb:YAG ceramics as laser media*. Optical Materials, 2010. **33**(2): p. 205-210.

40. Esposito, L., et al., *Experimental features affecting the transparency of YAG ceramics*. Optical Materials, 2011. **33**(5): p. 713-721.
41. Hostaša, J., *Transparent YAG Ceramics for Laser Applications*, in *Department of Glass and Ceramics*. 2015, University of Chemistry and Technology: Prague. p. 132.
42. Hostaša, J., L. Esposito, and A. Piancastelli, *Influence of Yb and Si content on the sintering and phase changes of Yb:YAG laser ceramics*. Journal of the European Ceramic Society, 2012. **32**(11): p. 2949-2956.
43. Serantoni, M., et al., *Improvements in the production of Yb:YAG transparent ceramic materials: Spray drying optimisation*. Optical Materials, 2012. **34**(6): p. 995-1001.
44. Yang, P., P. Deng, and Z. Yin, *Concentration quenching in Yb:YAG*. Journal of Luminescence, 2002. **97**(1): p. 51-54.
45. Yin, H., P. Deng, and F. Gan, *Defects in YAG: Yb crystals*. Journal of applied physics, 1998. **83**(7): p. 3825-3828.
46. Dong, J., et al., *Comparative study the effect of Yb concentrations on laser characteristics of Yb:YAG ceramics and crystals*. Laser Physics Letters, 2008. **6**(4): p. 282.
47. Chen, X., et al., *Electric-field-induced composite color centers formation and Yb ions valence state change in spark plasma sintered Yb:YAG transparent ceramics*. Optical Materials, 2019. **95**: p. 109192.
48. Solomonov, V., V. Osipov, and A. Spirina, *Luminescence of Yb-doped YAG: Divalent ytterbium ions*. Journal of Luminescence, 2016. **169**: p. 151-155.
49. Tang, F., et al., *Fabrication and laser behavior of the Yb:YAG ceramic microchips*. Optical Materials, 2011. **33**(8): p. 1278-1282.
50. Xu, X., et al., *Structural, thermal, and luminescent properties of Yb-doped Y3Al5O12 crystals*. Journal of the Optical Society of America B, 2004. **21**(3): p. 543-547.
51. Wu, Y., et al., *Diode-Pumped Yb:YAG Ceramic Laser*. Journal of the American Ceramic Society, 2007. **90**(10): p. 3334-3337.
52. Tang, F., et al., *Photoluminescence and laser behavior of Yb:YAG ceramic*. Optical Materials, 2012. **34**(5): p. 757-760.
53. Luo, D., et al., *Fabrication and laser properties of transparent Yb:YAG ceramics*. Optical Materials, 2012. **34**(6): p. 936-939.
54. Tang, F., et al., *Dependence of optical and thermal properties on concentration and temperature for Yb:YAG laser ceramics*. Journal of Alloys and Compounds, 2014. **593**: p. 123-127.
55. Pandey, S.J., et al., *Quantification of non-stoichiometry in YAG ceramics using laser-induced breakdown spectroscopy*. Optical Materials Express, 2017. **7**(2): p. 627-632.
56. Coccia, L.G., G.C. Tyrrell, and I.W. Boyd, *Gas-phase reactions during reactive laser ablation of Ti and Si in N2 and O2 rarefied atmospheres analysed using energy-dispersive mass spectrometry*. Applied surface science, 1997. **109**: p. 413-418.
57. Simmons, J.D. and J.K. McDonald, *The emission spectrum of AlN*. Journal of Molecular Spectroscopy, 1972. **41**(3): p. 584-594.
58. Olsen, H.N., *Partition function cutoff and lowering of the ionization potential in an argon plasma*. Physical Review, 1961. **124**(6): p. 1703.
59. Raizer, Y.P. and Y.B. Zeldovich, *Physics of Shock Waves and High- Temperature Hydrodynamic Phenomena. Volume I*. FOREIGN TECHNOLOGY DIV WIRGHT-PATTERSON AFB OH, 1966.
60. Kramida, A., et al., *NIST Atomic Spectra Database*.
61. Lindstrom, P.J. and W.G. Mallard, *NIST Chemistry Webbook, NIST Standard Reference 69*, in *National Institute of Standards and Technology, Gaithersburg MD, 20899*. 2010.
62. Hermann, J. and C. Dutouquet, *Local thermal equilibrium plasma modeling for analyses of gas-phase reactions during reactive-laser ablation*. Journal of applied physics, 2002. **91**(12): p. 10188-10193.
63. Kurucz, R.L. *The Kurucz Smithsonian atomic and molecular database*. in *Astrophysical Applications of Powerful New Databases*. 1995.

64. Aragón, C. and J.A. Aguilera, *Characterization of laser induced plasmas by optical emission spectroscopy: A review of experiments and methods*. Spectrochimica Acta Part B: Atomic Spectroscopy, 2008. **63**(9): p. 893-916.
65. Cowan, R.D. and G.H. Dieke, *Self-absorption of spectrum lines*. Reviews of Modern Physics, 1948. **20**(2): p. 418.
66. Cremers, D.A. and L.J. Radziemski, *Handbook of laser-induced breakdown spectroscopy*. 2013: John Wiley & Sons.
67. Pandey, S.J., et al., *Effect of powder compact density on the LIBS analysis of Ni impurities in alumina powders*. Spectrochimica Acta Part B: Atomic Spectroscopy, 2018. **148**: p. 99-104.
68. Sivakumar, P., et al., *Packing density effects on the fluctuations of the emission lines in laser-induced breakdown spectroscopy*. Spectrochimica Acta Part B: Atomic Spectroscopy, 2014. **92**: p. 84-89.
69. Hübner, S. and A. Melzer, *Dust-Induced Modulation of the Atomic Emission in a Dusty Argon Discharge*. Physical Review Letters, 2009. **102**(21): p. 215001.
70. Stehrer, T., et al., *Laser-induced breakdown spectroscopy of iron oxide powder*. Journal of Analytical Atomic Spectrometry, 2009. **24**(7): p. 973-978.
71. Aguilera, J.A. and C. Aragón, *Analysis of rocks by CSigma laser-induced breakdown spectroscopy with fused glass sample preparation*. Journal of Analytical Atomic Spectrometry, 2017. **32**(1): p. 144-152.
72. Carvalho, A.A., et al., *Comparison of Fused Glass Beads and Pressed Powder Pellets for the Quantitative Measurement of Al, Fe, Si and Ti in Bauxite by Laser-Induced Breakdown Spectroscopy*. Geostandards and Geoanalytical Research, 2017. **41**(4): p. 585-592.
73. Carvalho, A.A.C., et al., *Internal standard fused glass beads for high silicon content sample analysis by laser-induced breakdown spectrometry*. Journal of Analytical Atomic Spectrometry, 2018. **33**(7): p. 1243-1250.
74. Negre, E., et al., *On the performance of laser-induced breakdown spectroscopy for quantitative analysis of minor and trace elements in glass*. Journal of Analytical Atomic Spectrometry, 2015. **30**(2): p. 417-425.
75. Pease, P., *Fused glass sample preparation for quantitative laser-induced breakdown spectroscopy of geologic materials*. Spectrochimica Acta Part B: Atomic Spectroscopy, 2013. **83-84**: p. 37-49.
76. Rahaman, M.N., *Ceramic processing and sintering*. 2014: CRC press.
77. Kingery, W.D., H.K. Bowen, and D.R. Uhlmann, *Introduction to ceramics*. Vol. 17. 1976: John wiley & sons.
78. Richardson, M. and R. Gaume, *Transparent ceramics for lasers - A game-changer*. AMERICAN CERAMIC SOCIETY BULLETIN, 2012. **91**(4): p. 4p.
79. Esposito, L., et al., *Integrated analysis of non-linear loss mechanisms in Yb:YAG ceramics for laser applications*. Journal of the European Ceramic Society, 2012. **32**(10): p. 2273-2281.
80. Van Dijk, H., *Translucent Y3Al5O12 ceramics*. Materials research bulletin, 1984. **19**(12): p. 1669-1674.
81. Sekita, M., et al., *Induced emission cross section of Nd: Y3Al5O12 ceramics*. Journal of applied physics, 1990. **67**(1): p. 453-458.
82. Ikesue, A., I. Furusato, and K. Kamata, *Fabrication of Polycrystalline, Transparent YAG Ceramics by a Solid-State Reaction Method*. Journal of the American Ceramic Society, 1995. **78**(1): p. 225-228.
83. Boulesteix, R., et al., *Mechanism of the liquid-phase sintering for Nd:YAG ceramics*. Optical Materials, 2009. **31**(5): p. 711-715.
84. Kochawattana, S., et al., *Sintering and grain growth in SiO2 doped Nd:YAG*. Journal of the European Ceramic Society, 2008. **28**(7): p. 1527-1534.
85. Li, J., et al., *Laminar-structured YAG/Nd: YAG/YAG transparent ceramics for solid-state lasers*. International Journal of Applied Ceramic Technology, 2008. **5**(4): p. 360-364.
86. Maître, A., et al., *Effect of Silica on the Reactive Sintering of Polycrystalline Nd:YAG Ceramics*. Journal of the American Ceramic Society, 2008. **91**(2): p. 406-413.

87. Gaume, R., et al., *Effect of Si-induced defects on 1 μm absorption losses in laser-grade YAG ceramics*. Journal of Applied Physics, 2012. **111**(9): p. 093104.
88. Boulesteix, R., et al., *The effect of silica doping on neodymium diffusion in yttrium aluminum garnet ceramics: implications for sintering mechanisms*. Journal of the European Ceramic Society, 2009. **29**(12): p. 2517-2526.
89. Hostasa, J., et al., *Polycrystalline Yb³⁺-Er³⁺-co-doped YAG: Fabrication, TEM-EDX characterization, spectroscopic properties, and comparison with the single crystal*. Journal of Materials Research, 2014. **29**(19): p. 2288.
90. Sun, W.Y., et al., *Solubility of Si in YAG*. Journal of Solid State Chemistry, 1984. **51**(3): p. 315-320.
91. Kuru, Y., et al., *Enhanced co-solubilities of Ca and Si in YAG (Y₃Al₅O₁₂)*. physica status solidi c, 2008. **5**(10): p. 3383-3386.
92. Zamir, S., *Solubility limit of Si in YAG at 1700°C in vacuum*. Journal of the European Ceramic Society, 2017. **37**(1): p. 243-248.
93. Ikesue, A., Y.L. Aung, and V. Lupei, *Ceramic lasers*. 2013: Cambridge University Press.
94. Pandey, S.J., et al., *Quantification of SiO₂ sintering additive in YAG transparent ceramics by laser-induced breakdown spectroscopy (LIBS)*. Optical Materials Express, 2017. **7**(5): p. 1666-1671.
95. Hostaša, J., et al., *Preparation and characterization of Yb-doped YAG ceramics*. Optical Materials, 2013. **35**(4): p. 798-803.
96. Ikesue, A., et al., *Optical Scattering Centers in Polycrystalline Nd:YAG Laser*. Journal of the American Ceramic Society, 1997. **80**(6): p. 1517-1522.